

T-1103

THE KERNEL FUNCTION IN
DIRECT-CURRENT RESISTIVITY SOUNDING

By

Hans Arnt Meinardus

ProQuest Number: 10795862

All rights reserved

INFORMATION TO ALL USERS

The quality of this reproduction is dependent upon the quality of the copy submitted.

In the unlikely event that the author did not send a complete manuscript and there are missing pages, these will be noted. Also, if material had to be removed, a note will indicate the deletion.



ProQuest 10795862

Published by ProQuest LLC (2018). Copyright of the Dissertation is held by the Author.

All rights reserved.

This work is protected against unauthorized copying under Title 17, United States Code
Microform Edition © ProQuest LLC.

ProQuest LLC.
789 East Eisenhower Parkway
P.O. Box 1346
Ann Arbor, MI 48106 – 1346

A Thesis submitted to the Faculty and the Board of Trustees of the Colorado School of Mines in partial fulfillment of the requirements for the degree of Doctor of Science in Geophysical Engineering.

Signed: Paul A. Meinardus

Student

Golden, Colorado

Date: 1/17, 1967

Approved: George V. Keller

Thesis Advisor

Paul A. Meinardus
Head of Department

Golden, Colorado

Date: 1/17, 1967

ABSTRACT

The apparent resistivity obtained by direct-current resistivity sounding over a horizontally layered earth can be expressed as a Hankel transform of the so-called kernel function. This function depends only on the layer thicknesses and resistivities, and not on the particular electrode arrays used in the measurements. This research was conducted to study the analytical properties and the use of the kernel function in interpreting resistivity sounding data. The numerical techniques developed for this purpose are implemented for digital computers and applied to the analysis of theoretical geoelectric models.

The value of the kernel function at the origin is given by the ratio of the resistivity of the lowermost infinite substratum to the surface resistivity. For large values of its argument, the kernel function approaches the value one, with a rate determined by the first layer thickness. In a logarithmic coordinate system, resistivity functions

symmetric with respect to depth produce kernel functions symmetric with respect to their argument. For a perfectly resistant or a perfectly conductive basement, the kernel function, plotted logarithmically, approaches asymptotically a straight line with a slope of minus 1 or plus 1, respectively. The position of this line depends on the ratio of the surface conductivity to the total conductance of the overlaying formations in the first case, and on the ratio of the surface resistivity to the transverse resistance in the second case.

Representative kernel functions for the Adena oil field, (Morgan County, Colorado), are computed from electric well logs digitized with a ten-foot interval. A Hankel transformation of these kernels, using Gaussian quadrature, furnishes "synthetic" resistivity sounding curves for the Adena field. These curves can be used to study exploration requirements of resistivity sounding surveys in the area. For "direct" detection of the pay zones in this particular oil field, an accuracy of field measurements much better than 1 percent at a distance of three to five miles from the current source is required.

Electrical soundings can be interpreted in the kernel-domain by inverse Hankel transformation of the observed apparent resistivity curves. This procedure probably

leads to a more nearly accurate determination of the layering parameters than curve matching methods. For the inversion of sounding curves recorded over a section with a resistant basement, the numerical technique developed for the Hankel transformation can be applied, making the correction for the branch of the curve raising with a slope of 1. The application of this formula to the inversion of simulated apparent resistivity data for the Adena field shows that the numerical accuracy is sufficient for practical purposes.

CONTENTS

	page
Abstract	iii
Illustrations	ix
Tables	xi
Acknowledgments	xiii
Introduction	1
Surface Potential and Kernel Function Associated with Direct Current Flow	4
Statement of the Resistivity Sounding Problem	4
Uniqueness of Solution	7
Formal Solution of Problem (5)	9
Some Properties of Equation (6i)	11
The Kernel Function	15
Relationship between the Kernel Function and the Two-Dimensional Fourier Transform	17
Some Properties of the Kernel Function	19
Langer's reciprocal relation	19
Behavior of $K(\lambda)$ for large λ	19

Behavior of $K(\lambda)$ for small λ	20
The kernel function in logarithmic coordinates	25
Kernel Functions for Continuous $\sigma(z)$	27
Kernel Functions for Discontinuous $\sigma(z)$	33
The Kernel Function for a Horizontally Layered Medium	41
Sunde's Recurrence Relation	42
Flathe's Recurrence Relation	44
Van'yan's Recurrence Relation	46
A Model Study of Kernel Functions for the Adena Oil Field, Morgan County, Colorado	49
General description of the Adena Field	50
The Kernel Functions for the Adena Oil Field	55
Effect of sampling interval	55
Effect of random noise in the resistivities	57
Equivalent layers for the geoelectric section	58
Detection of a target layer	63
Lateral variation of the kernel function	65
Effect of the disturbing factors in well logging on the true rock resistivities	66
Interpolation of the Kernel Function	74
The Numerical Evaluation of Hankel Transforms	78
The Apparent Resistivities of Some Common Arrays	78
The Fundamental Integral in the Expressions for Apparent Resistivities	82

Evaluation of the Basic Hankel Transforms by Series Expansion	86
Evaluation of the Basic Hankel Transforms by Numerical Quadrature	89
Polynomial approximation of the kernel function	89
Polynomial approximation of the integrand	95
Synthetic Sounding Curves for the Adena Field	106
The Interpretation of Resistivity Data Via Kernel Function	112
Formulas for the Inversion of Apparent Resistivities	113
Single-pole array	113
Wenner array	114
Schlumberger array	118
Polar-dipole array	122
The Interpretation of the Kernel Function	132
Asymptotic behavior of the kernel function	133
Stripping off the top layer	134
Summary and Conclusions	137
Appendix	141
List of Computer Programs	141
Flow Chart for Subroutine Kernel	144
Generalized Flow Chart for Hankel Transform Program	145
References	146

ILLUSTRATIONS

Figure	page
1. The single electrode configuration	4
2. The potential of a section overlaying a perfect resistor	22
3. Kernel function for a three-layer case. Layer thicknesses 1, 10; layer resistivities 1, 1000, 0.001	28
4. Kernel function for a four-layer case. Layer thicknesses 1, 1, 1; layer resistivities 1, 100, 0.1, 100	29
5. Medium with a discontinuous conductivity function	33
6. Geoelectric model for the Adena field	53
7. Adena field, "J" sand-net oil and gas isopach	54
8. Kernel function computed from Hough no.1 electric log digitized with a ten-foot interval	56
9. Hough no.1, Adena, electric log and some equivalent models	60
10. Comparison of the kernel function from the digitized electric log of Hough no.1 with the five layer model (5-12)	61

Figure	page
11. Probability density for Hough no.1, Adena, short normal resistivity	68
12. Probability density for Hough no.1, Adena, long normal resistivity	69
13. Probability distribution for Hough no.1, Adena, short normal resistivity	70
14. Probability distribution for Hough no.1, Adena, long normal resistivity	71
15. Approximation of the kernel	91
16. Effect of the transform variable r on the product $\phi(\lambda)J_0(x)$	98
17. Synthetic sounding curves for Hough no.1, model (6-2)	108
18. Synthetic sounding curves for Hough no.1, model (40)	109
19. Transforms of synthetic Schlumberger curve for Hough no.1, model (6-2)	127
20. Transform of synthetic Schlumberger curve for Hough no.1, model (6-2) using resistant basement formula (99)	128
21. Transforms of simulated Schlumberger field data for Hough no.1, model (6-2)	131
22. Horizontally layered earth model	133

TABLES

Table	page
I. Conductivity - kernel pairs	32
II. Some solutions of equation (6i) and their derivatives	38
III. Some two-layer conductivity models	39
IV. Effect of 50 and 20 feet sampling intervals of the kernel functions as compared to 10-foot sampling interval	57
V. Comparison of kernel functions without "D" and "J" sand in the section with the original kernel function	64
VI. Comparison of the kernel function for Hough no.1 with the kernel functions for some surrounding wells	65
VII. Comparison of the kernel function for Hough no.1 with the kernel functions for two wells without "D" and "J" sand	66
VIII. Comparison of the geoelectric parameters measured with the short and long normal arrays	67
IX. Effect of anisotropy θ of Paleozoic rocks in Hough no.1 on the "D" and "J" sand anomalies	74

Table	page
X. Divided difference table near the origin of the kernel function for Hough no.1, equivalent model (6-2)	76
XI. Apparent resistivities for several arrays	81
XII. Comparison of the Hankel transforms $H_1(r)$ computed in two different ways	95
XIII. Errors between exact and approximated transforms	105
XIV. Comparison of apparent resistivities computed by asymptotic expansion and by quadrature	107
XV. Simulated Schlumberger field data for Adena field	130

ACKNOWLEDGMENTS

It is a pleasure to express my appreciation and indebtedness to Professor George V. Keller for suggesting the subject of this thesis, and for helping me during the research with valuable suggestions.

I wish to express my gratitude to the Colorado School of Mines' Computer Center for giving me unlimited access to its computing facilities; my appreciation to the Graduate School of the University of Colorado for granting me free computer time.

To my colleague Mr. Russel L. Gray, I am particularly grateful for valuable help in digital computer programming, and for numerous stimulating discussions.

I also extend my thanks to the staff of the Colorado School of Mines, where I was privileged to study for three years.

Finally, I wish to express my deep gratitude to National Science Foundation, and in particular to

Dr. T. O. Jones, Division Director of Environmental Sciences,
for granting me with a generous scholarship (Grant NSF GA-39)
during my graduate study, which made this work possible.

INTRODUCTION

The geophysicist interpreting resistivity sounding curves is often faced with multi-layered earth models for which no set of master curves is available. Partial curve matching is useful for finding approximate solutions to the problem, however, this procedure does not make use of the inherent accuracy of the data. Consequently, some of the information contained in the observations is lost at the interpretation stage. Modern digital computer technology provides the tools to attack this problem numerically. The so-called "kernel function" offers the most promising path to its solution because this function is more directly related to the geoelectrical model than the apparent resistivity is.

The literature on the subject of interpretation in the kernel-domain includes papers by Slichter (1933), Pekeris (1940), Vozoff (1958), and Koefoed (1965a, 1965b, and 1966). The work of these authors is concentrated on the step of

obtaining the bed thicknesses and resistivities of the section from the kernel function. Except for Koefoed (1965a, and 1965b), who presents a graphical method, the step of obtaining the kernel function by a Hankel transform of observed apparent resistivities has not been considered.

Thus, this thesis was undertaken to develop an accurate numerical technique for the Hankel transformation and to study the general properties of kernel functions. Little attention is paid to "direct" interpretation methods, consisting in the analytical determination of the resistivity function of the medium from its kernel. The writer believes that determining the layering model from the kernel function is, as in every other interpretation problem in geophysics, essentially a step where geological judgment, past experience, and ingenuity are significant.

A mathematical model study is used throughout this thesis. The necessary digital computer programs are developed and then applied to a reasonable geological situation to test the requirements on the different variables involved.

The first chapter is a detailed discussion of the physical properties of direct-current flow in a horizontally uniform medium. Next, different algorithms for computing the kernel function for a horizontally layered earth are analyzed, and Sunde's recurrence relation is applied to a

model study of kernel functions for the Adena oil field, Morgan County, Colorado. The next chapter pertains to numerical methods for evaluating Hankel transforms, suitable for digital computers. Finally, the interpretation of resistivity sounding data in the kernel domain is considered.

SURFACE POTENTIAL AND KERNEL FUNCTION
ASSOCIATED WITH DIRECT-CURRENT FLOW

Statement of the Resistivity Sounding Problem

The basic physical concepts of direct current-resistivity sounding are explained by the theoretical single-pole setup shown in figure 1.

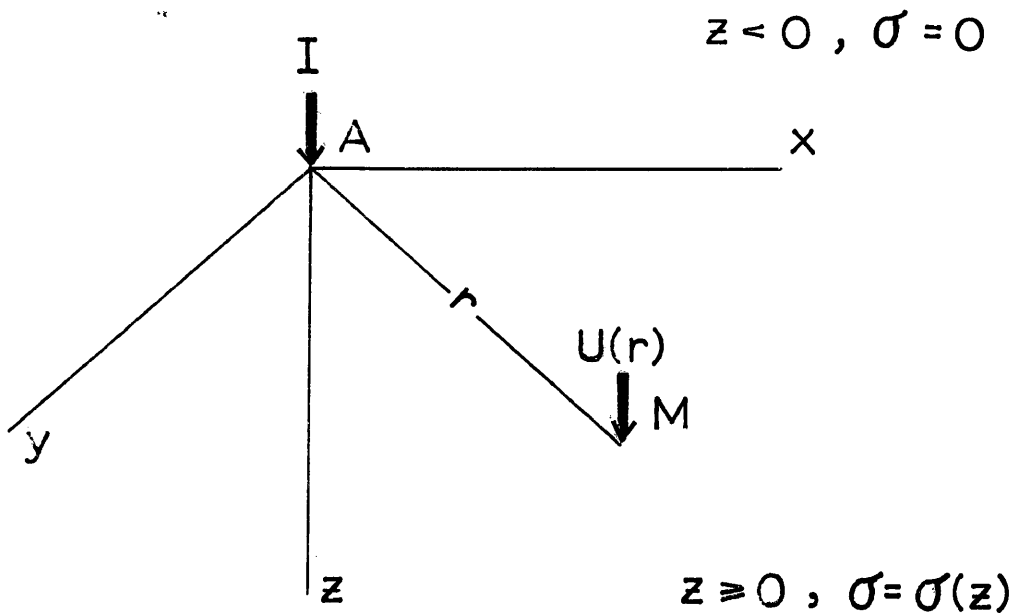


Figure 1.

The single-electrode configuration

A point electrode located at the origin A of an orthogonal cartesian coordinate system supplies a direct-current of intensity I (amperes) to an isotropic, horizontally uniform half space of conductivity $\sigma(z)$ (mhos/m). The surface potential $U(r)$, expressed in volts, arising from the current flow in the medium is measured with another point electrode at the point M, a distance of r meters away from the source A. (The MKS system of units is used throughout this thesis.) The fundamental geophysical problem is to obtain the conductivity variation with depth $\sigma(z)$ of the medium from the potential measured at a number of observation points M.

The single-pole configuration is a mathematical abstraction analogous to an isolated simple electrostatic charge. In actual field surveys, other electrode arrays, involving at least four electrodes are used instead.

The differential equation for the potential U is established from the following fundamental relationships,

$$\nabla \cdot \vec{J} = 0 \quad \vec{J}(0, 0, 0) \rightarrow \infty \quad (1)$$

\vec{J} : current density (amp/m)

$$\vec{J} = \sigma(z) \vec{E} \quad (2)$$

\vec{E} : electric field (volt/m)

$$\vec{E} = -\nabla U \quad (3)$$

$$\nabla \cdot (\sigma(z) \vec{E}) = \sigma(z) \nabla \cdot \vec{E} + \vec{E} \cdot \nabla \sigma(z) = 0$$

$$\nabla^2 U + \frac{1}{\sigma(z)} \nabla \sigma(z) \cdot \nabla U = 0 \quad (4)$$

Because of the axial symmetry of the current flow, it is convenient to adopt a cylindrical system of coordinates, then

$$U = U(r, z),$$

and equation (4) becomes

$$\frac{\partial^2 U}{\partial r^2} + \frac{1}{r} \frac{\partial U}{\partial r} + \frac{\partial^2 U}{\partial z^2} + \frac{\sigma'(z)}{\sigma(z)} \frac{\partial U}{\partial z} = 0 \quad (5)$$

$$0 < \sigma(z) < \infty, \quad r \geq 0, \quad z \geq 0, \quad \sigma'(z) \triangleq \frac{d\sigma(z)}{dz},$$

$\sigma(z)$ and $\sigma'(z)$ are continuous.

Equation (5) is a second-order partial differential equation of the elliptic type; for its solution two independent boundary conditions are required:

Dirichlet conditions on the infinite halfsphere

$$R = \sqrt{r^2 + z^2},$$

$$U(r, z) \rightarrow 0 \quad \text{as } R \rightarrow \infty, \quad (51)$$

Neumann conditions on the infinite plane $z = 0$,

$$J_z(r, 0) = 0 \quad r \neq 0.$$

There is no current flow across the plane $z = 0$, except at the point electrode at $r = 0$,

$$\frac{2\pi r J_z(r, 0)}{I} = 0 \quad r \neq 0$$

$$\frac{2\pi r J_z(0, 0)}{I} = \infty \quad r = 0 .$$

From the continuity of current flow it follows that,

$$\int_0^{\infty} \frac{2\pi J_z(r, 0)}{I} r dr = 1$$

The last three equations show that $2\pi r J_z(r, 0)/I$ behaves like Dirac's delta function; hence,

$$J_z(r, 0) = \frac{I \delta(r)}{2\pi r}$$

$$J_z(r, 0) = \sigma(0) E_z(r, 0) = -\sigma(0) \frac{\partial}{\partial z} U(r, 0) .$$

Therefore, the Neumann conditions can be rewritten

$$\frac{\partial}{\partial z} U(r, 0) = -\frac{I \delta(r)}{2\pi \sigma(0) r} . \quad (5ii)$$

Uniqueness of Solution

Theorem: If there exists a solution to the boundary-value problem (5), then this is the only one possible.

Proof: With the assumption that $U = U(r, z)$ is one solution satisfying conditions (5), and that there exists $U^* = U^*(r, z)$ also satisfying (5), it follows that,

$$\left. \frac{\partial U^*}{\partial z} \right|_{z=0} = - \frac{I \delta(\tau)}{2\pi \sigma(0) \tau}$$

If $W \triangleq U - U^*$, then

$$\left. \frac{\partial W}{\partial z} \right|_{\substack{\tau=0 \\ z=0}} = 0 \quad ,$$

which implies $\hat{J}(r, z) = 0$ at $r = 0$, where \hat{J} is the current density associated with the potential W . In other words, the current flow I^* is zero. Hence, $\hat{J}(r, z) = 0$ everywhere, and

$$\sigma(z) \vec{E}(\tau, z) = - \sigma(z) \nabla W(\tau, z) = 0$$

Excluding the case $\sigma(z) = 0$, which is only of academic interest,

$$\nabla W(r, z) = 0$$

$$W = \text{constant.}$$

From the Dirichlet conditions

$$U(r, z) \rightarrow 0 \quad \text{as } r \rightarrow \infty \quad \text{and}$$

$$U^*(r, z) \rightarrow 0 \quad \text{as } r \rightarrow \infty \quad , \quad \text{which shows}$$

that the value of the constant must be zero, i.e.

$$W = 0 \quad \text{for all space, hence,}$$

$$U^* = U \quad \text{for all space, Q.E.D.}$$

Formal Solution of Problem (5)

The boundary value problem (5) has been solved by separation of variables (Slichter, 1933). The solution using integral transform techniques is given in the following development.

Starting with the Hankel transform pair

$$V(\lambda, z) = \int_0^{\infty} U(\tau, z) \tau J_n(\lambda\tau) d\tau$$

$$U(\tau, z) = \int_0^{\infty} V(\lambda, z) \lambda J_n(\lambda\tau) d\lambda \quad ,$$

where $J_n(x)$ is the Bessel function of the first kind and n th order, and setting $n = 0$, the potential function may be written

$$U(\tau, z) = \int_0^{\infty} V(\lambda, z) \lambda J_0(\lambda\tau) d\lambda \quad .$$

Differentiating

$$\frac{\partial}{\partial \tau} U(\tau, z) = \int_0^{\infty} V(\lambda, z) \lambda \frac{d}{d\tau} J_0(\lambda\tau) d\lambda$$

$$= \int_0^{\infty} V(\lambda, z) \lambda [-\lambda J_1(\lambda\tau)] d\lambda$$

and,

$$\frac{1}{\tau} \frac{\partial}{\partial \tau} U(\tau, z) = - \int_0^{\infty} \frac{1}{\tau} V(\lambda, z) \lambda^2 J_1(\lambda, \tau) d\lambda \quad ,$$

$$\frac{\partial^2}{\partial r^2} U(r, z) = - \int_0^{\infty} V(\lambda, z) \lambda^2 \frac{d}{d\tau} J_1(\lambda\tau) d\lambda.$$

From the formulas for derivatives of Bessel functions

$$\frac{d}{d\tau} J_1(\lambda\tau) = \lambda J_0(\lambda\tau) - \frac{1}{\tau} J_1(\lambda\tau)$$

it follows that

$$\frac{\partial^2}{\partial r^2} U(r, z) = - \int_0^{\infty} V(\lambda, z) \lambda^2 \left[\lambda J_0(\lambda\tau) - \frac{1}{\tau} J_1(\lambda\tau) \right] d\lambda.$$

Hence,

$$\frac{\partial^2 U}{\partial r^2} + \frac{1}{r} \frac{\partial U}{\partial r} = - \int_0^{\infty} \lambda^2 V(\lambda, z) \lambda J_0(\lambda\tau) d\lambda,$$

also,

$$\frac{\partial^2 U}{\partial z^2} + \frac{\sigma'(z)}{\sigma(z)} \frac{\partial U}{\partial z} = \int_0^{\infty} \lambda \left[\frac{d^2 V}{dz^2} + \frac{\sigma'(z)}{\sigma(z)} \frac{dV}{dz} \right] J_0(\lambda\tau) d\lambda.$$

Consequently,

$$\int_0^{\infty} \left\{ \frac{d^2}{dz^2} V(\lambda, z) + \frac{\sigma'(z)}{\sigma(z)} \frac{d}{dz} V(\lambda, z) - \lambda^2 V(\lambda, z) \right\} \lambda J_0(\lambda\tau) d\lambda = 0.$$

One possible solution of this integral equation is that the expression in the braces vanishes. From the uniqueness of solution proved earlier, it is seen that this is "the" solution. Thus, problem (5) has the formal solution

$$\frac{d^2}{dz^2} V(\lambda, z) + \frac{\sigma'(z)}{\sigma(z)} \frac{d}{dz} V(\lambda, z) - \lambda^2 V(\lambda, z) = 0 \quad (6i)$$

$$U(\tau, z) = \int_0^{\infty} V(\lambda, z) \lambda J_0(\lambda \tau) d\lambda \quad . \quad (6ii)$$

Conditions (5i) and (5ii) will be introduced after discussing equation (6i).

Some Properties of Equation (6i)

Equation (6i) is an ordinary, linear differential equation with variable coefficients. Unfortunately, there is no general solution available for this second-order equation, as there is for the corresponding first-order equation. Unless equation (6i) reduces to a type with constant coefficients, which can be integrated in terms of elementary functions, the solution has to be expressed in infinite form. That is, an infinite series, a definite integral, a contour integral, or continued fractions are required. The solutions of some standard forms arising frequently in mathematical physics, as for instance the Bessel equations, have been expressed in special transcendental functions.

Approximate methods, such as asymptotic solutions, or the WKBJ method, can not be applied to equation (6i), because they require a large parameter λ , which is not the case in the present problem where $0 \leq \lambda \leq \infty$.

Even if the solution to equation (6i) is not known explicitly, some of its fundamental properties can be established. The corresponding general theory has been developed by Sturm (Ince, 1956), who studied extensively equations of the type

$$L(y) = \frac{d}{dx} \left\{ K(x) \frac{dy}{dx} \right\} - G(x)y = 0 .$$

$K(x)$ and $G(x)$ are continuous and real functions in some interval (a,b) .

Equation (6i) can be written as the Sturmian equation

$$\frac{d}{dz} \left\{ \sigma(z) \frac{d}{dz} V(\lambda, z) \right\} - \lambda^2 \sigma(z) V(\lambda, z) = 0 , \quad (7)$$

where

$$K = \sigma(z) , \quad G = \lambda^2 \sigma(z) .$$

The initial conditions of equation (7) are:

$$V(\lambda, 0) = \int_0^{\infty} U(\tau, 0) \tau J_0(\lambda \tau) d\tau \quad (7i)$$

$$\begin{aligned} \frac{d}{dz} V(\lambda, 0) &= \int_0^{\infty} \frac{\partial}{\partial z} U(\tau, 0) \tau J_0(\lambda \tau) d\tau \\ &= - \int_0^{\infty} \frac{I \delta(\tau)}{2\pi \sigma(0) \tau} \tau J_0(\lambda \tau) d\tau \end{aligned}$$

$$V'(\lambda, 0) = \frac{-I}{2\pi \sigma(0)} \quad (7ii)$$

Sturm established the fundamental theorem that the initial value problem (7) has one and only one solution. This unique solution can be expressed as the sum of two linearly independent solutions if the Wronskian $W(z)$ does not vanish on the interval $0 \leq z \leq \infty$. Consequently, the general solution of (7) can be written

$$V(\lambda, z) = C_1(\lambda)V_1(\lambda, z) + C_2(\lambda)V_2(\lambda, z) ,$$

where both V_1 and V_2 satisfy equations (7). From Abel's identity (Ince, 1956, p. 75) it follows that

$$W(z) \stackrel{\Delta}{=} \begin{vmatrix} V_1 & V_2 \\ \frac{dV_1}{dz} & \frac{dV_2}{dz} \end{vmatrix} = C \exp \left[- \int^z \frac{\sigma'(z)}{\sigma(z)} dz \right]$$

$$W(z) = \frac{C}{\sigma(z)} ;$$

where,

$$C = V_1(\lambda, 0)V_2'(\lambda, 0) - V_2(\lambda, 0)V_1'(\lambda, 0) . .$$

The last two relationships show that there are two independent solutions V_1 and V_2 of equations (7), as long as $\sigma(z)$ remains bounded, and $C \neq 0$.

Another consequence of Sturm's theory is that the solutions of the equation $L(y) = 0$ are non-oscillatory (having at most one zero), if $G \geq 0$ in the interval (a, b) . Since in

in equation (7) $\lambda^2 \sigma(z) \geq 0$, the important result arises that V_1 and V_2 are both non-oscillatory for all z .

The behavior of the solutions V_1 and V_2 for large λ may be studied by reducing equation (7) to an equation not containing the first derivative. To achieve this the following change of variable is carried out

$$V(z) = u \exp \left[-\frac{1}{2} \int^z \frac{\sigma'(z)}{\sigma(z)} dz \right] = \frac{u}{\sqrt{\sigma(z)}} .$$

Equation (7) changes to

$$\frac{d^2 u}{dz^2} - u I(z) = 0 , \quad (8)$$

where

$$I(z) = \lambda^2 + \frac{1}{4} \left[\frac{\sigma'(z)}{\sigma(z)} \right]^2 + \frac{1}{2} \left[\frac{\sigma'(z)}{\sigma(z)} \right]' .$$

Given that $\sigma(z) \neq 0$, and $\sigma(z)$, $\sigma'(z)$ are both continuous for all z , equation (8) becomes:

$$\frac{d^2 u}{dz^2} - \lambda^2 u = 0 , \text{ as } \lambda \rightarrow \infty ,$$

its solution is

$$u = C_1(\lambda) e^{-\lambda z} + C_2(\lambda) e^{+\lambda z} ;$$

hence, the solution of equation (7) for large λ approaches

$$V(\lambda, z) = C_1(\lambda) \frac{e^{-\lambda z}}{\sqrt{\sigma(z)}} + C_2(\lambda) \frac{e^{+\lambda z}}{\sqrt{\sigma(z)}} \quad \lambda \rightarrow \infty .$$

This expression shows that one solution remains bounded, the other unbounded with either z or λ .

The Kernel Function

In the last paragraph it was shown that the solution to equation (6i) can be written

$$V(\lambda, z) = C_1(\lambda)V_1(\lambda, z) + C_2(\lambda)V_2(\lambda, z).$$

With V_2 the solution which is unbounded as $z \rightarrow \infty$, it is reasonable by considering (6ii) and (5i) to set $C_2(\lambda) = 0$. This arbitrary assumption yields a solution of the boundary value problem (5). From the uniqueness of solution proved on page 8 it follows that this solution is the only one possible.

Hence,

$$U(\tau, z) = \int_0^{\infty} C_1(\lambda) V_1(\lambda, z) \lambda J_0(\lambda \tau) d\lambda$$

$$\left. \frac{\partial}{\partial z} U(\tau, z) \right|_{z=0} = \int_0^{\infty} C_1(\lambda) V_1'(\lambda, 0) \lambda J_0(\lambda \tau) d\lambda$$

where

$$V_1'(\lambda, 0) \triangleq \left. \frac{\partial}{\partial z} V_1(\lambda, z) \right|_{z=0}$$

From (5ii)

$$\frac{-I \delta(\tau)}{2\pi \sigma(0) \tau} = \int_0^{\infty} C_1(\lambda) V_1'(\lambda, 0) \lambda J_0(\lambda \tau) d\lambda,$$

inverting this transform yields

$$C_1(\lambda) V_1'(\lambda, 0) = \frac{-I}{2\pi \sigma(0)} ,$$

so that the potential is given by

$$U(\tau, z) = \frac{-I}{2\pi \sigma(0)} \int_0^{\infty} \frac{V_1(\lambda, z)}{V_1'(\lambda, 0)} \lambda J_0(\lambda \tau) d\lambda . \quad (9)$$

The surface potential is of interest in prospecting,

$$U(\tau, 0) = \frac{-I}{2\pi \sigma(0)} \int_0^{\infty} \frac{V_1(\lambda, 0)}{V_1'(\lambda, 0)} \lambda J_0(\lambda \tau) d\lambda .$$

Denoting by $K(\lambda)$ the kernel function corresponding to a given conductivity function $\sigma(z)$, the surface potential can be written

$$U(\tau) = \frac{I}{2\pi \sigma(0)} \int_0^{\infty} K(\lambda) J_0(\lambda \tau) d\lambda \quad (10i)$$

$$K(\lambda) \triangleq -\lambda \frac{V_1(\lambda, 0)}{V_1'(\lambda, 0)} . \quad (10ii)$$

It is customary in mathematical physics to call $J_0(\lambda r)$ the kernel of the integral transform (10i). However, Slichter (1933) assigned the name "kernel" to the function given by equation (10ii), a designation which has been followed

later by other authors and is now well established in the literature on electrical prospecting.

Relationship between the Kernel Function and the Two-Dimensional Fourier Transform of the Surface Potential

Expression (10i) shows that

$$U(r) = \frac{I}{2\pi \sigma(o)} \int_0^{\infty} K(\lambda) J_0(\lambda r) d\lambda$$

is the surface potential expressed as Fourier-Bessel transform. From the identity

$$\int_0^{2\pi} e^{i\lambda r \cos \psi} d\psi = 2\pi J_0(\lambda r) \quad ,$$

the Fourier-Bessel integral can be transformed to

$$U(r) = \frac{I}{(2\pi)^2 \sigma(o)} \int_0^{\infty} \int_0^{2\pi} K(\lambda) e^{i\lambda r \cos \psi} d\psi d\lambda$$

Changing from the polar coordinate systems, in both the λ and r -domains to orthogonal cartesian coordinates by the transformation

$$\begin{aligned} \alpha &= \lambda \cos \phi & x &= r \cos \theta \\ \beta &= \lambda \sin \phi & y &= r \sin \theta \quad , \end{aligned}$$

and letting

$$\begin{aligned} \psi &= \phi - \theta \\ d\psi &= d\phi \end{aligned}$$

$$\begin{aligned}\lambda \operatorname{rcos} \psi &= \lambda \operatorname{rcos}(\phi - \theta) \\ &= \alpha x + \beta y.\end{aligned}$$

The Jacobian of the transformation is given by

$$J = \begin{vmatrix} \frac{\partial \lambda}{\partial \alpha} & \frac{\partial \lambda}{\partial \beta} \\ \frac{\partial \phi}{\partial \alpha} & \frac{\partial \phi}{\partial \beta} \end{vmatrix} = \begin{vmatrix} \cos \phi & \sin \phi \\ -\frac{\sin \phi}{\lambda} & \frac{\cos \phi}{\lambda} \end{vmatrix} = \frac{1}{\lambda}$$

$$\lambda = \sqrt{\alpha^2 + \beta^2},$$

and the potential in the new system of coordinates becomes

$$U(x, y) = \frac{I}{(2\pi)^2 \sigma(0)} \int_{-\infty}^{\infty} \int_{-\infty}^{\infty} \frac{K(\alpha, \beta)}{\sqrt{\alpha^2 + \beta^2}} e^{i(\alpha x + \beta y)} d\alpha d\beta. \quad (11)$$

The potential function $U(x, y)$ and the function $F(\alpha, \beta) = (K(\alpha, \beta)/\sqrt{\alpha^2 + \beta^2})I/\sigma(0)$ constitute a two-dimensional Fourier transform pair. In effect, equation (10i) is a special case of a two-dimensional Fourier transform resulting from the cylindrical symmetry of the problem. Equation (11) could have been derived by applying the two-dimensional Fourier transform to equation (4) expressed in orthogonal cartesian coordinates. But, the expression of the potential as a Hankel transform of the kernel function, equation (10i), is better suited for numerical computation because only one integration is required.

Some Properties of the Kernel Function

1. Langer's reciprocal relation.-- If $K(\lambda)$ is the kernel corresponding to $\sigma(z)$, then $Q(\lambda) = 1/K(\lambda)$ is the kernel corresponding to $\rho(z) = 1/\sigma(z)$, (Slichter, 1933).

2. Behavior of $K(\lambda)$ for large λ --

$$\lim_{\lambda \rightarrow \infty} K(\lambda) = \lim_{\lambda \rightarrow \infty} -\lambda \left. \frac{V_1(\lambda, z)}{V_1'(\lambda, 0)} \right|_{z=0},$$

from page 14

$$V_1(\lambda, z) \rightarrow \frac{e^{-\lambda z}}{\sqrt{\sigma(z)}}, \quad \text{as } \lambda \rightarrow \infty$$

and

$$V_1(\lambda, 0) = \frac{1}{\sqrt{\sigma(0)}}$$

$$V_1'(\lambda, z) = \frac{-\lambda e^{-\lambda z} \sqrt{\sigma(z)} - \frac{1}{2} e^{-\lambda z} [\sigma(z)]^{-\frac{1}{2}} \sigma'(z)}{\sigma(z)}$$

$$V_1'(\lambda, 0) = \frac{-\lambda \sigma(0) - \frac{1}{2} \sigma'(0)}{[\sigma(0)]^{3/2}}$$

$$\lim_{\lambda \rightarrow \infty} K(\lambda) = \lim_{\lambda \rightarrow \infty} -\lambda \frac{\sigma(0)}{-\lambda \sigma(0) - \frac{1}{2} \sigma'(0)}$$

$$\lim_{\lambda \rightarrow \infty} K(\lambda) = 1. \quad (15)$$

3. Behavior of $K(\lambda)$ for small λ .--

Defining

$$K(0) \triangleq \lim_{\lambda \rightarrow 0} K(\lambda) \quad ,$$

then from equation (10ii),

$$K(0) = \lim_{\lambda \rightarrow 0} \frac{-\lambda V_1(\lambda, 0)}{\frac{\partial}{\partial z} V_1(\lambda, 0)} \quad ,$$

and from equations (7i) and (7ii)

$$V_1(\lambda, 0) = \frac{1}{C_1(\lambda)} \int_0^{\infty} U(\tau) \tau J_0(\lambda \tau) d\tau$$

$$\frac{\partial}{\partial z} V_1(\lambda, 0) = \frac{-I \rho(0)}{2 \pi C_1(\lambda)} \quad ;$$

hence,

$$K(0) = \frac{2 \pi}{I \rho(0)} \lim_{\lambda \rightarrow 0} \lambda \int_0^{\infty} U(\tau) \tau J_0(\lambda \tau) d\tau \quad ,$$

with the change of variable $\lambda \tau = x$

$$K(0) = \frac{2 \pi}{I \rho(0)} \lim_{\lambda \rightarrow 0} \int_0^{\infty} U\left(\frac{x}{\lambda}\right) \frac{x}{\lambda} J_0(x) dx \quad .$$

From (10i) it is seen that if the medium is homogeneous ($K(\lambda) = 1$), then

$$U(\tau) = \frac{I \rho(0)}{2 \pi \tau} \quad .$$

If the medium is homogeneous from a certain depth z_n on, or in other words, if the lowermost layer of the section

extends to infinite depth with a constant, finite resistivity $\rho(z_n)$, this layer will ultimately determine the behavior of the potential function for large r , i.e.

$$\lim_{r \rightarrow \infty} U(r) \rightarrow \frac{I \rho(z_n)}{2 \pi r} \quad (16)$$

Consequently, by taking the limit of the integrand,

$$K(0) = \frac{\rho(z_n)}{\rho(0)} \int_0^{\infty} J_0(x) dx$$

$$K(0) = \frac{\rho(z_n)}{\rho(0)} \quad (17)$$

If the resistivity of the substratum at depth z_n is either unbounded or zero, equation (16) does not apply, and another method has to be used to find the behavior of the kernel function at the origin.

A perfectly resistant or conductive bed of finite thickness located at some depth z_n of the section acts as a screen eliminating every direct current effect of the underlying medium. This phenomenon can be easily visualized by considering the paths of the current flow under these circumstances.

For a perfect resistor at depth z_n it follows from the continuity of current flow, that

$$I = \int_{(S)} \vec{J} \cdot d\vec{S} = - \int_{(S)} \sigma(z) \nabla U \cdot d\vec{S}$$

Because no current flows through the planes $z = 0$ and $z = z_n$, the surface S can be considered to include only the vertical surface of the cylinder with radius r and height z_n shown in figure 2.

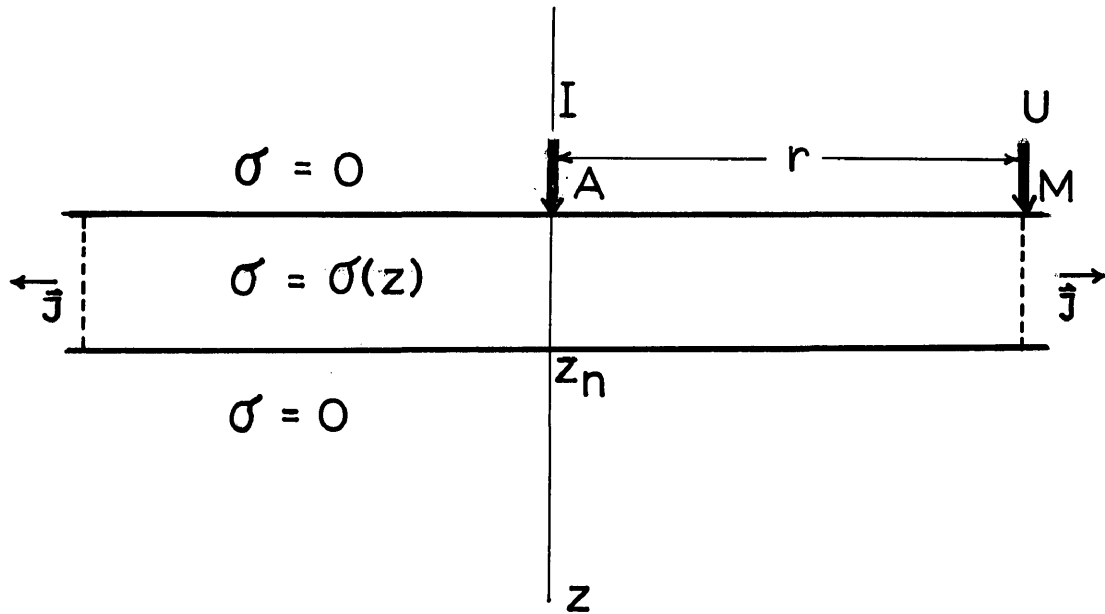


Figure 2.

The potential of a section overlaying a perfect resistor

The current vector \vec{J} will be essentially parallel to the horizontal boundaries of the disc if r is taken sufficiently large compared with z_n .

Under this condition

$$\nabla U = \hat{r} \frac{\partial U}{\partial r} \quad r \rightarrow \infty ,$$

and

$$I = - \int_0^{2\pi} \int_0^{z_m} \sigma(z) \frac{\partial U}{\partial r} r dz d\theta ;$$

if

$$S \triangleq \int_0^{z_m} \sigma(z) dz$$

is the total conductance of the section resting on top of the resistor,

$$I = - 2\pi r \frac{\partial U}{\partial r} S \quad r \rightarrow \infty . \quad (18)$$

Integrating with respect to r , and defining the potential such that the integration constant becomes zero,

$$\lim_{r \rightarrow \infty} U(r) = \frac{I}{2\pi S} \log \frac{1}{r} ,$$

which shows that the potential is logarithmic for large spacing r , and tends to $-\infty$ rather than zero as in formula (16).

The kernel function for this limiting case is obtained from $\frac{\partial U}{\partial r}$ instead of U . Setting $K(\lambda) = \phi(\lambda) + 1$ in equation (10i) in order to secure the convergence of the integrals in the following steps,

$$U(r) = \frac{I}{2\pi\sigma(o)} \left\{ \frac{1}{r} + \int_0^{\infty} \Phi(\lambda) J_0(\lambda r) d\lambda \right\} ,$$

then

$$\frac{\partial}{\partial r} U(r) = \frac{-I}{2\pi\sigma(o)} \left\{ \frac{1}{r^2} + \int_0^{\infty} \lambda \Phi(\lambda) J_1(\lambda r) d\lambda \right\}$$

$$\frac{2\pi\sigma(o)}{I} \frac{\partial}{\partial r} U(r) + \frac{1}{r^2} = - \int_0^{\infty} \lambda \Phi(\lambda) J_1(\lambda r) d\lambda ;$$

inverting,

$$\Phi(\lambda) = - \frac{2\pi\sigma(o)}{I} \int_0^{\infty} r \frac{\partial U}{\partial r} J_1(\lambda r) dr - \int_0^{\infty} \frac{J_1(\lambda r)}{r} dr ,$$

but

$$\int_0^{\infty} \frac{J_1(\lambda r)}{r} dr = 1 ;$$

(Abramowitz and Stegun, 1965, p. 486)

consequently,

$$K(\lambda) = - \frac{2\pi\sigma(o)}{I} \int_0^{\infty} r \frac{\partial U}{\partial r} J_1(\lambda r) dr .$$

This integral may be written

$$\int_0^{\infty} r \frac{\partial U}{\partial r} J_1(\lambda r) dr = \int_0^{\epsilon} r \frac{\partial U}{\partial r} J_1(\lambda r) dr + \int_{\epsilon}^{\infty} r \frac{\partial U}{\partial r} J_1(\lambda r) dr .$$

When r becomes vanishingly small, $\frac{\partial U}{\partial r}$ is of order $\frac{1}{r^2}$, and $J_1(\lambda r)$ is of order r , which shows that the first integral on the right side vanishes as $\epsilon \rightarrow 0$. With the change

of variable $\lambda r = x$ in the second integral on the right side it is seen that when $\lambda \rightarrow 0$, $r \rightarrow \infty$ ($x \neq 0$), so that the value of $r \frac{\partial U}{\partial r}$ obtained from equation (18) can be substituted into the integral provided that λ becomes vanishingly small,

$$\lim_{\lambda \rightarrow 0} K(\lambda) = \frac{2\pi\sigma(o)}{I} \int_0^{\infty} \frac{I}{2\pi S} J_1(\lambda r) dr,$$

hence,

$$\lim_{\lambda \rightarrow 0} K(\lambda) = \frac{\sigma(o)}{\lambda S}, \quad \sigma(z_n) \rightarrow 0. \quad (19i)$$

For a perfect conductor at depth, from Langer's reciprocal relation,

$$\lim_{\lambda \rightarrow 0} K(\lambda) = \frac{\lambda T}{\rho(o)}, \quad \rho(z_n) \rightarrow 0 \quad (19ii)$$

where

$$T \triangleq \int_0^{z_n} \rho(z) dz$$

is called the transverse resistance of the upper section.

4. The kernel function in logarithmic coordinates.--
There are several advantages of plotting the kernel function in logarithmic coordinates. As a consequence of Langer's reciprocal relation, $\log\{K(\lambda)\}$ corresponding to a conductivity variation $\sigma(z)$, and $\log\{Q(\lambda)\}$ corresponding to the reciprocal of $\sigma(z)$ are symmetric with respect to the λ -axis. This

property does not hold for the logarithmic graphs of the potential or apparent resistivities plotted against some spacing factor. Thus, a catalog of kernel function curves for layered media would need only half the number of curves of the corresponding resistivity catalog.

The slope of the kernel function for the resistant base-ment case is obtained from equation (19i),

$$\log [K(\lambda)] = -\log \lambda + \log \frac{\sigma(0)}{S} \quad \lambda \rightarrow 0.$$

This linear equation shows that $\log\{K(\lambda)\}$ is asymptotic for small values of λ to a straight line with slope of minus 1 passing through the point $\lambda = \frac{\sigma(0)}{S}$, $K = 1$.

Similarly, for a perfect conductor at depth, $\log\{K(\lambda)\}$ approaches asymptotically a straight line with slope of plus 1 through the point $\lambda = \frac{\rho(0)}{T}$, $K = 1$.

Because only one perfect resistor or conductor can be observed in a particular kernel curve, its slope must lie between plus and minus 1. In practice, however, beds with finite thickness and relatively large resistivity contrasts produce slopes of 1, which do not occur at the origin if the substratum has a finite resistivity. The kernel function of the Hough no.1 well log from the Adena field, (Morgan County, Colorado) resolved into 560 layers (figure 10), provides an example. Here the resistivity contrast of the lowest layers

is 1 : 40, and the kernel function is tangent to a straight line with slope of minus 1, cutting the λ -axis at $\lambda \approx 0.00015$. With a total conductance of $S = 630$ mhos, and a surface resistivity of 10 ohm-m, the theoretical crossing point is

$$\lambda_c = \frac{\sigma(0)}{S} = \frac{0.1}{630} \approx 0.00016 .$$

If several sufficiently thick layers with strong resistivity contrasts are present, the kernel curve will approach several lines with slope of 1. As before, the intersection of each asymptotic line will be determined by the total conductance or the transverse resistance of the overlaying beds. Illustrations of repeating slopes of about plus and about minus 1 are presented in figures 3 and 4.

Kernel Functions for Continuous $\sigma(z)$

The solution of equation (6i) for simple continuous conductivity functions $\sigma(z)$ allows the evaluation of the kernel function in closed form. The conductivity-kernel pairs presented in table I, except for the power conductivity law derived in the following development, are taken from Slichter (1933).

For the conductivity function $\sigma(z) = (\sigma(0) + kz)^p$, p real $\neq 0$, $k > 0$, $\sigma(0) > 0$, equation (6i) becomes

$$\frac{d^2}{dz^2} V(\lambda, z) + \frac{pk}{\sigma(0) + kz} \frac{d}{dz} V(\lambda, z) - \lambda^2 V(\lambda, z) = 0. (20)$$

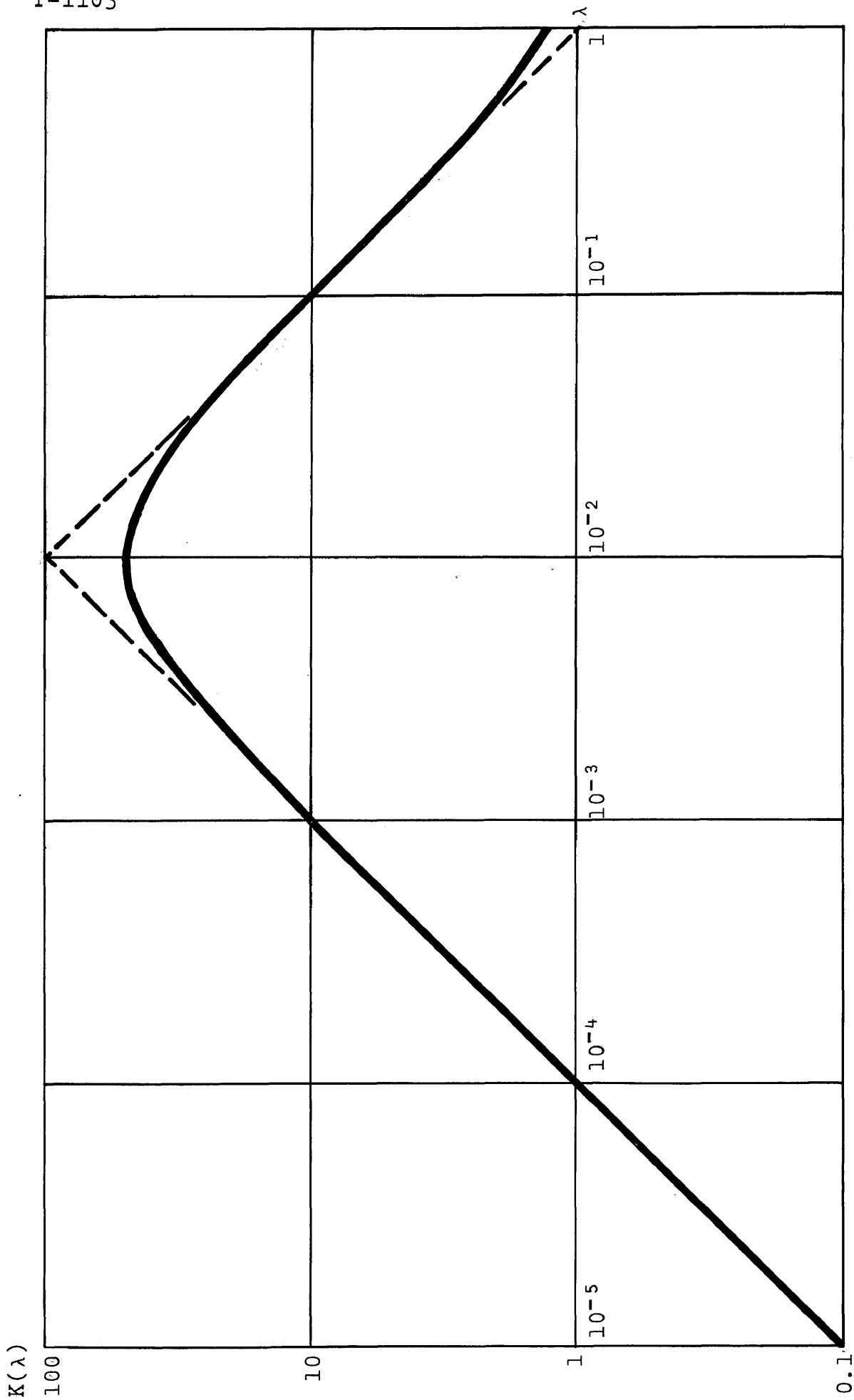


Figure 3.
Kernel function for a three-layer case. Layer thicknesses 1, 10;
layer resistivities 1, 1000, 0.001

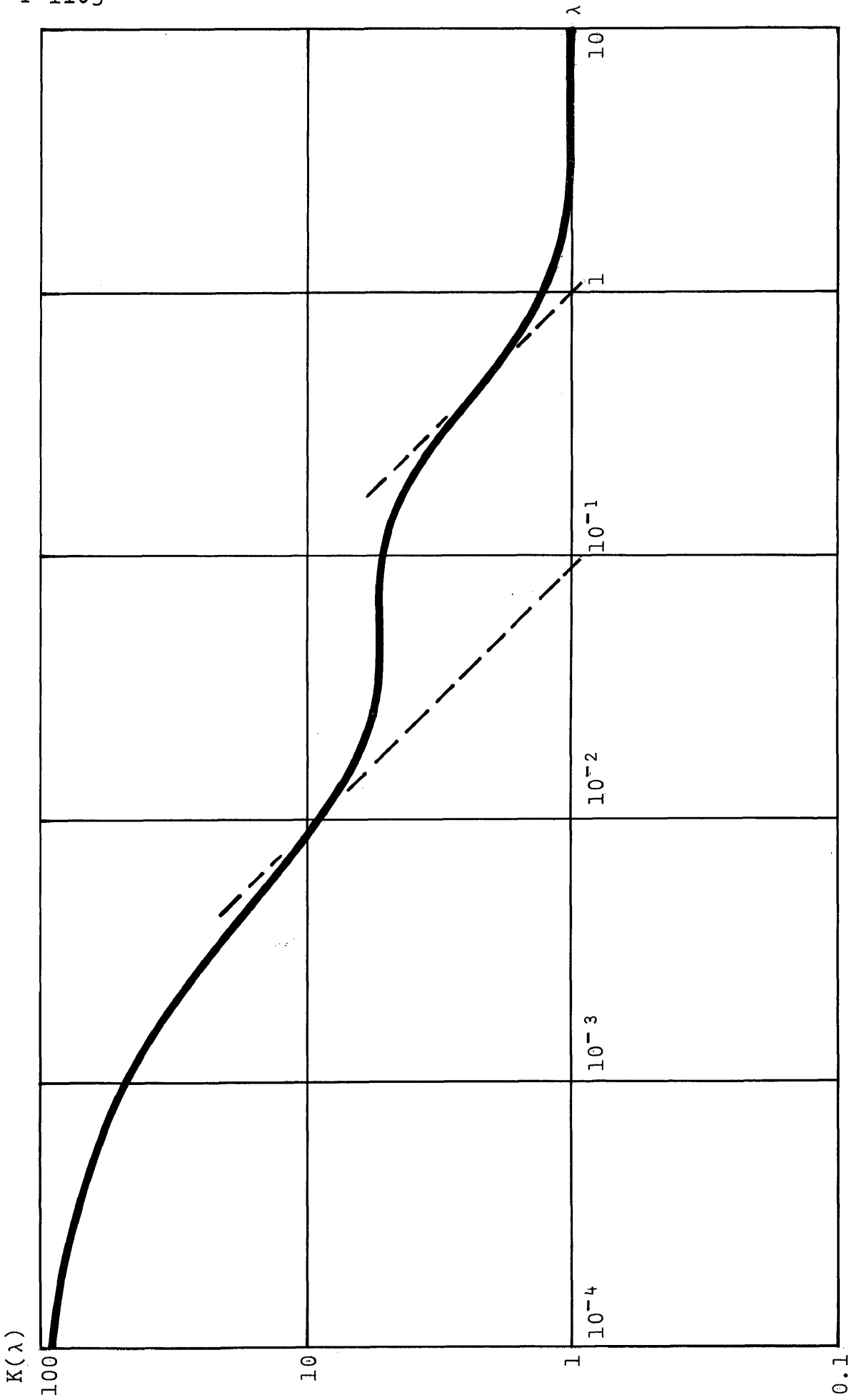


Figure 4.
Kernel function for a four-layer case. Layer thicknesses 1, 1, 1;
layer resistivities 1, 100, 0.1, 100

The change of variable $x = \sigma(0) + kz$ reduces this equation to a particular type of Bessel equation,

$$\frac{d^2}{dx^2} V(\lambda, x) + \frac{p}{x} \frac{d}{dx} V(\lambda, x) - \frac{\lambda}{k} V(\lambda, x) = 0 .$$

Its solution is expressed in terms of modified, or Bessel functions of imaginary argument (Abramowitz and Stegun, 1965, p. 362)

$$V(\lambda, x) = x^{\frac{1-p}{2}} \left\{ C_1 I_{\frac{1-p}{2}} \left(\frac{\lambda}{k} x \right) + C_2 K_{\frac{1-p}{2}} \left(\frac{\lambda}{k} x \right) \right\} .$$

The second term remains bounded for large argument; therefore, the appropriate solution to equation (20) is:

$$\begin{aligned} V_1(\lambda, z) &= [\sigma(0) + kz]^{\nu} K_{\nu} \left(\lambda \frac{\sigma(0)}{k} + \lambda z \right) \\ &= k^{\nu} \left[\frac{\sigma(0)}{k} + z \right]^{\nu} K_{\nu} \left[\lambda \left(\frac{\sigma(0)}{k} + z \right) \right] \end{aligned}$$

$$V_1(\lambda, 0) = \sigma(0) K_{\nu} \left(\lambda \frac{\sigma(0)}{k} \right)$$

$$\nu \triangleq \frac{1-p}{2} .$$

The differentiation formula

$$\frac{d}{dz} \left[z^\nu K_\nu(z) \right] = -z^\nu K_{\nu-1} \left(\lambda \frac{\sigma(0)}{k} \right) ,$$

(Abramowitz and Stegun, 1965, p. 376)

gives

$$V_1'(\lambda, 0) = -\lambda \sigma(0)^\nu K_{\nu-1} \left(\lambda \frac{\sigma(0)}{k} \right) ,$$

and finally,

$$K(\lambda) = \frac{K_\nu \left(\lambda \frac{\sigma(0)}{k} \right)}{K_{\nu-1} \left(\lambda \frac{\sigma(0)}{k} \right)} . \quad (21)$$

For the linear law $\sigma(z) = \sigma(0) + kz$,

$$K(\lambda) = \frac{K_0 \left(\frac{\sigma(0)}{k} \lambda \right)}{K_1 \left(\frac{\sigma(0)}{k} \lambda \right)} .$$

For the quadratic law $\sigma(z) = (\sigma(0) + kz)^2$, making use of the identity $K_{-\nu}(z) = K_\nu(z)$ (Abramowitz and Stegun, 1965, p. 375),

$$K(\lambda) = \frac{K_{1/2} \left(\frac{\sigma(0)}{k} \lambda \right)}{K_{3/2} \left(\frac{\sigma(0)}{k} \lambda \right)} .$$

Table I.
Conductivity - kernel pairs

$\sigma(z)$	$K(\lambda)$
constant $\sigma(o)$	1
exponential $\sigma(o) e^{kz}$ $\forall \text{ real } k$	$\frac{2\lambda}{k + \sqrt{k^2 + (2\lambda)^2}}$
power $(c + kz)^p$ $\forall \text{ real } p \neq 0$	$\frac{K_\nu\left(\frac{c}{k}\lambda\right)}{K_{\nu-1}\left(\frac{c}{k}\lambda\right)}$ $\nu \triangleq \frac{1-p}{2}$
hyperbolic $\sigma_o \sinh^2 \omega(z+c)$ $\arg \neq 0$	$\frac{\lambda c}{\omega c \coth \omega c + \sqrt{(\lambda c)^2 + (\omega c)^2}}$
$\sigma_o \cosh^2 \omega(z+c)$ $\forall \omega, c$	$\frac{\lambda c}{\omega c \tanh \omega c + \sqrt{(\lambda c)^2 + (\omega c)^2}}$
trigonometric $\sigma_o \sin^2 \omega(z+c)$ $0 < \arg < \pi$	$\frac{\lambda c}{\omega c \cot \omega c + \sqrt{(\lambda c)^2 - (\omega c)^2}}$
$\sigma_o \cos^2 \omega(z+c)$ $\frac{\pi}{2} < \arg < \frac{3\pi}{2}$	$\frac{\lambda c}{-\omega c \tan \omega c + \sqrt{(\lambda c)^2 - (\omega c)^2}}$

Kernel Functions for Discontinuous $\sigma(z)$

The simple models of table I apply for strictly continuous conductivity functions $\sigma(z)$ and $\sigma'(z)$. If these functions are only sectionally continuous, the potential function assumes an entirely different analytic form in each region separated by planes where discontinuities in $\sigma(z)$ and $\sigma'(z)$ occur. Two conditions must be satisfied at each of these boundaries:

- a). continuity of the potential function,
- b). continuity of the normal component of the current density.

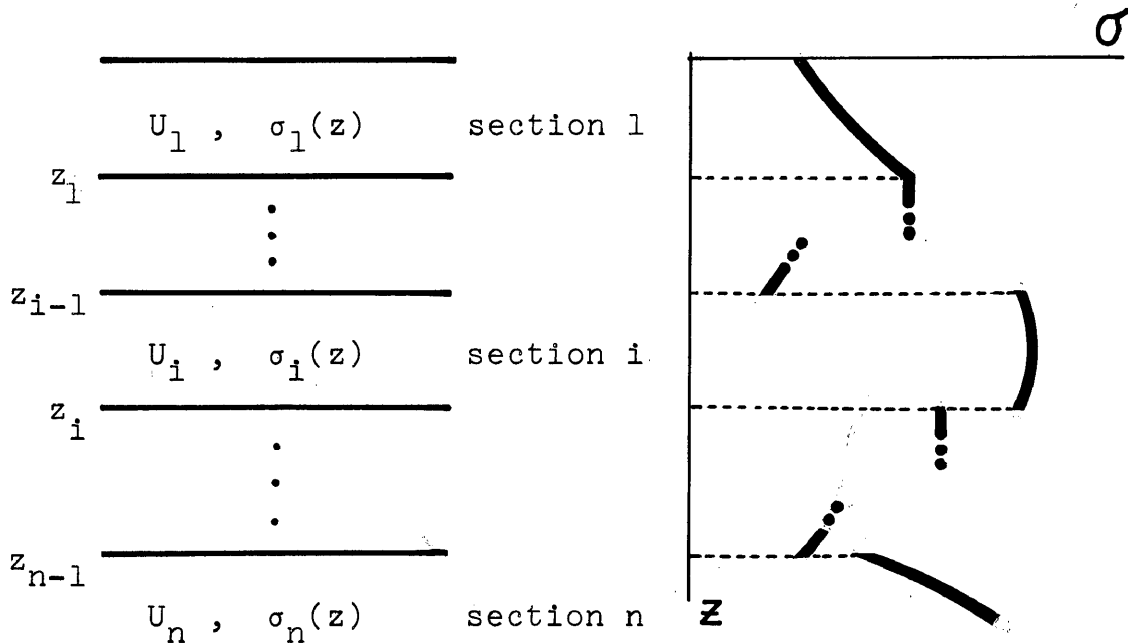


Figure 5.

Medium with a discontinuous conductivity function

The model for a discontinuous conductivity function consists of an infinite half space composed of an arbitrary, finite number n of sections. Each section i of thickness $z_i - z_{i-1}$ is characterized by its own continuous conductivity function $\sigma_i(z)$, as shown in figure 5.

The potential function U_i is given by:

$$U_i(r, z) = \int_0^{\infty} \{A_i F_i(\lambda, z) + B_i G_i(\lambda, z)\} \lambda J_0(\lambda r) d\lambda, \quad (22)$$

$$i = 1, 2, \dots, n; \quad z_{i-1} \leq z \leq z_i; \quad r \geq 0;$$

$$A_i = A_i(\lambda, z_i, \sigma(z_i)).$$

$F_i(\lambda, z)$ and $G_i(\lambda, z)$ are two linearly independent solutions of equation (6i). The constants A_i and B_i are determined from the boundary conditions.

At the surface $z = 0$,

$$\frac{\partial}{\partial z} U_i(r, 0) = -\frac{I}{2\pi \sigma(0)} \frac{\delta(r)}{r}.$$

At each boundary $z = z_i$,

$$U_i(r, z_i) = U_{i+1}(r, z_i)$$

$$\sigma_i(z_i) \frac{\partial}{\partial z} U_i(r, z_i) = \sigma_{i+1}(z_i) \frac{\partial}{\partial z} U_{i+1}(r, z_i).$$

For the n th section $z \geq z_{n-1}$,

$$\lim_{z \rightarrow \infty} U_n(r, z) = 0.$$

which from page 15 requires that $B_n = 0$.

The remaining $2n - 1$ constants A_i and B_i are determined from a system of $2n - 1$ linear equations. If the functional dependence on λ is omitted for simplicity; that is, if

$F_i(z_i) \triangleq F_i(\lambda, z_i)$, and $F_i'(z_i) \triangleq \frac{\partial}{\partial z} F_i(\lambda, z_i) \Big|_{z=z_i}$, then the system of linear equations may be written:

$$A_1 F_1'(0) + B_1 G_1'(0) = \frac{-1}{2\pi \sigma(0)}$$

$$A_1 F_1(z_1) + B_1 G_1(z_1) = A_2 F_2(z_1) + B_2 G_2(z_1)$$

$$\sigma_1(z_1) \{A_1 F_1'(z_1) + B_1 G_1'(z_1)\} = \sigma_2(z_1) \{A_2 F_2'(z_1) + B_2 G_2'(z_1)\}$$

•
•
•

$$A_i F_i(z_i) + B_i G_i(z_i) = A_{i+1} F_{i+1}(z_i) + B_{i+1} G_{i+1}(z_i)$$

$$\sigma_i(z_i) \{A_i F_i'(z_i) + B_i G_i'(z_i)\} = \sigma_{i+1}(z_i) \{A_{i+1} F_{i+1}'(z_i) + B_{i+1} G_{i+1}'(z_i)\} \quad (23)$$

•
•
•

$$A_{n-1} F_{n-1}(z_{n-1}) + B_{n-1} G_{n-1}(z_{n-1}) = A_n F_n(z_{n-1})$$

$$\sigma_{n-1}(z_{n-1}) \{A_{n-1} F_{n-1}'(z_{n-1}) + B_{n-1} G_{n-1}'(z_{n-1})\} = \sigma_n(z_{n-1}) A_n F_n'(z_{n-1})$$

The $(2n-1)$ by $(2n-1)$ determinant of system (23) is

$$\Delta = \begin{vmatrix} F_1'(0) & G_1'(0) & 0 & 0 & 0 & \dots & 0 \\ F_1(z_1) & G_1(z_1) & -F_2(z_1) & -G_2(z_1) & 0 & \dots & 0 \\ \sigma_1(z_1) F_1'(z_1) & \sigma_1(z_1) G_1'(z_1) & -\sigma_2(z_1) F_2'(z_1) & -\sigma_2(z_1) G_2'(z_1) & 0 & \dots & 0 \\ 0 & 0 & F_2(z_2) & G_2(z_2) & -F_3(z_2) & \dots & 0 \\ 0 & 0 & \sigma_2(z_2) F_2'(z_2) & \sigma_2(z_2) G_2'(z_2) & -\sigma_3(z_2) F_3'(z_2) & \dots & 0 \\ 0 & 0 & 0 & 0 & F_3(z_3) & \dots & 0 \\ \dots & \dots & \dots & \dots & \dots & \dots & \dots \\ 0 & 0 & 0 & \dots & F_{n-1}(z_{n-1}) & G_{n-1}(z_{n-1}) & -F_n(z_{n-1}) \\ 0 & 0 & 0 & \dots & \sigma_{n-1}(z_{n-1}) F_{n-1}'(z_{n-1}) & \sigma_{n-1}(z_{n-1}) G_{n-1}'(z_{n-1}) & -\sigma_n(z_{n-1}) F_n'(z_{n-1}) \end{vmatrix}$$

With A_{ij} denoting the cofactor of the element a_{ij} of this determinant, the surface potential $U(r,0)$ becomes from equation (22),

$$U_1(r,0) = \frac{-I}{2\pi\sigma(0)} \int_0^\infty \frac{A_{11} F_1(0) + A_{12} G_1(0)}{\Delta} \lambda J_0(\lambda r) d\lambda$$

$$U_1(\tau, 0) = \frac{-I}{2\pi G(0)} \int_0^{\infty} \frac{A_{11} F_1(0) + A_{12} G_1(0)}{A_{11} F_1'(0) + A_{12} G_1'(0)} \lambda J_0(\lambda \tau) d\lambda.$$

The kernel function is, consequently,

$$K(\lambda) = -\lambda \frac{A_{11} F_1(0) + A_{12} G_1(0)}{\frac{d}{dz} \{A_{11} F_1(0) + A_{12} G_1(0)\}},$$

or alternatively,

$$K(\lambda) = -\lambda \frac{F_1(0) + \frac{A_{12}}{A_{11}} G_1(0)}{F_1'(0) + \frac{A_{12}}{A_{11}} G_1'(0)} \quad (24)$$

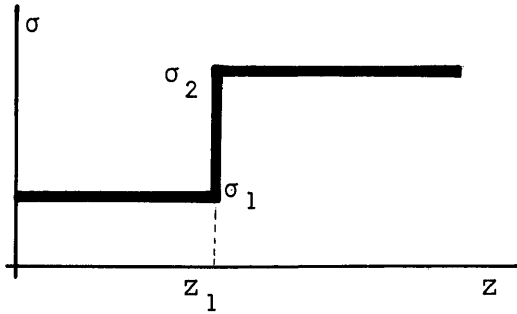
Table II shows the functions F and G together with their derivatives, corresponding to the conductivity laws listed in table I. Equation (24) allows one to compute the analytic expression of the kernel corresponding to any combination of these conductivity functions. Table III gives the kernel functions for a few models consisting of two sections, each characterized by some conductivity law from table I. Most widely used is model 1, the two-layer case. Exponential or power conductivity laws might be helpful for representing certain geological situations. In some special cases they can also be used to approximate multi-layered models.

Table II.
Some solutions of equation (6i) and their derivatives

Conductivity law σ	$F(\lambda, z)$	$G(\lambda, z)$	$\frac{\partial}{\partial z} F(\lambda, z)$	$\frac{\partial}{\partial z} G(\lambda, z)$
constant $\sigma(z_i)$	$e^{-\lambda z}$	$e^{\lambda z}$	$-\lambda e^{-\lambda z}$	$\lambda e^{\lambda z}$
exponential e^{kz}	$e^{-\frac{1}{2} \left\{ \sqrt{k^2 + (2\lambda)^2} + k \right\} z}$	$e^{\frac{1}{2} \left\{ \sqrt{k^2 + (2\lambda)^2} - k \right\} z}$	$-\frac{1}{2} \left\{ \sqrt{k^2 + (2\lambda)^2} + k \right\} F(\lambda, z)$	$\frac{1}{2} \left\{ \sqrt{k^2 + (2\lambda)^2} - k \right\} G(\lambda, z)$
power $(c+kz)^p$	$(c+kz)^p K_{\nu} \left[\left(\frac{c}{k} + z \right) \lambda \right]$ $\nu = \frac{1-p}{2}$	$(c+kz)^p I_{\nu} \left[\left(\frac{c}{k} + z \right) \lambda \right]$	$-\lambda (c+kz)^p K_{\nu-1} \left[\left(\frac{c}{k} + z \right) \lambda \right]$	$\lambda (c+kz)^p I_{\nu-1} \left[\left(\frac{c}{k} + z \right) \lambda \right]$
hyperbolic $\sinh^2[\omega(z+c)]$	$\frac{-\sqrt{\lambda^2 + \omega^2} z}{\sinh[\omega(z+c)]}$	$\frac{\sqrt{\lambda^2 + \omega^2} z}{\sinh[\omega(z+c)]}$	$-\frac{\sinh\left\{ \log(\omega + \sqrt{\lambda^2 + \omega^2} + \omega(z+c)) \right\}}{\sinh[\omega(z+c)]} F$	$\frac{\sinh\left\{ \log(\omega + \sqrt{\lambda^2 + \omega^2} - \omega(z+c)) \right\}}{\sinh[\omega(z+c)]} G$
trigonom. $\sin^2[\omega(z+c)]$	$\frac{e^{-\sqrt{\lambda^2 - \omega^2} z}}{\sin[\omega(z+c)]}$	$\frac{e^{\sqrt{\lambda^2 - \omega^2} z}}{\sin[\omega(z+c)]}$	$-\frac{\sin\left\{ \tan^{-1}[\omega(\lambda^2 - \omega^2)^{\frac{1}{2}}] + \omega(z+c) \right\}}{\sin[\omega(z+c)]} F$	$\frac{\sin\left\{ \tan^{-1}[\omega(\lambda^2 - \omega^2)^{\frac{1}{2}}] - \omega(z+c) \right\}}{\sin[\omega(z+c)]} G$

Table III.

Some two-layer conductivity models

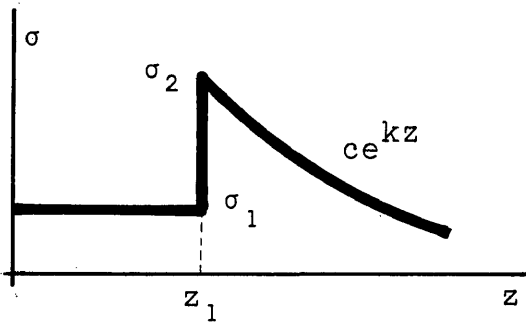


model 1

$$K(\lambda) = \frac{1 - Q}{1 + Q}$$

where

$$Q \triangleq \frac{\sigma_2 - \sigma_1}{\sigma_2 + \sigma_1} e^{-2\lambda z_1}$$



model 2

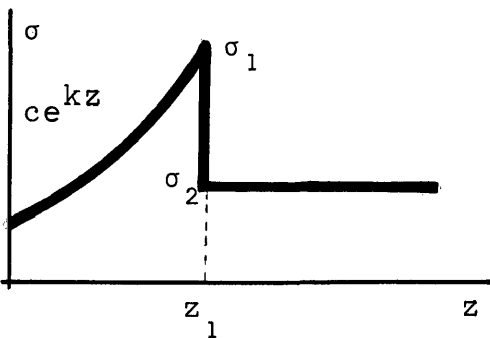
$$K(\lambda) = \frac{1 - Q}{1 + Q}$$

where

$$Q \triangleq \frac{\sigma_2 \tau - \sigma_1 \lambda}{\sigma_2 \tau + \sigma_1 \lambda} e^{-2\lambda z_1}$$

and

$$\tau \triangleq \frac{1}{2} \left\{ \sqrt{R^2 + (2\lambda)^2} + R \right\}$$



model 3

$$K(\lambda) = \frac{\tau - sQ}{\tau + sQ}$$

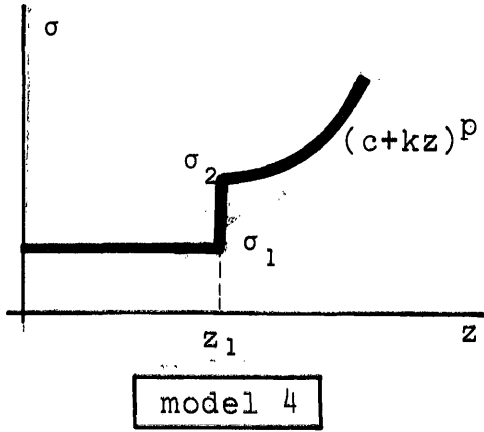
where

$$Q \triangleq \frac{\sigma_2 \lambda - \sigma_1 \tau}{\sigma_2 \lambda + \sigma_1 \tau} e^{-z_1(\tau + s)}$$

$$\tau \triangleq \frac{1}{2} \left\{ \sqrt{R^2 + (2\lambda)^2} + R \right\}$$

and

$$s \triangleq \frac{1}{2} \left\{ \sqrt{R^2 + (2\lambda)^2} - R \right\}$$



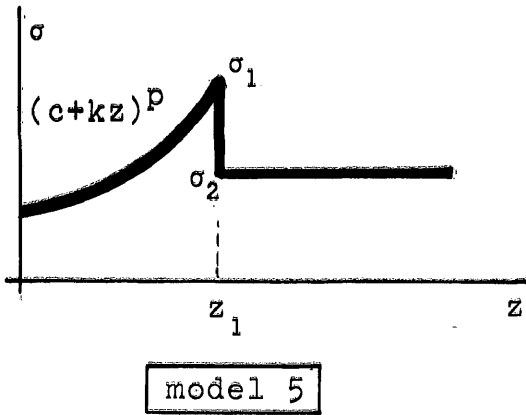
$$K(\lambda) = \frac{1 - Q}{1 + Q}$$

where

$$Q \triangleq \frac{\sigma_2 K_{\nu-1}(\frac{u_1}{k}\lambda) - \sigma_1 K_{\nu}(\frac{u_1}{k}\lambda)}{\sigma_2 K_{\nu-1}(\frac{u_1}{k}\lambda) + \sigma_1 K_{\nu}(\frac{u_1}{k}\lambda)} e^{-2\lambda z_1}$$

and

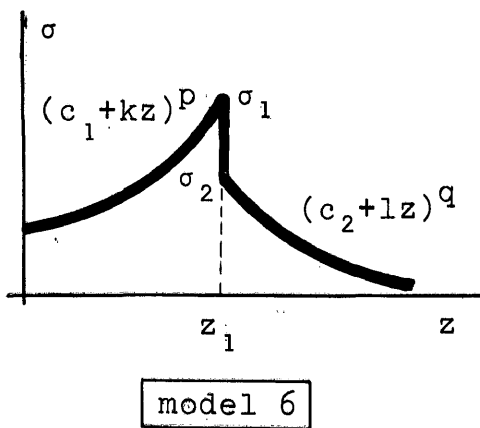
$$u_1 \triangleq c + kz_1, \quad \nu \triangleq \frac{1-p}{2}$$



$$K(\lambda) = \frac{K_{\nu}(\frac{c}{k}\lambda) - Q I_{\nu}(\frac{c}{k}\lambda)}{K_{\nu-1}(\frac{c}{k}\lambda) + Q I_{\nu-1}(\frac{c}{k}\lambda)}$$

where

$$Q \triangleq \frac{\sigma_2 K_{\nu}(\frac{u_1}{k}\lambda) - \sigma_1 K_{\nu-1}(\frac{u_1}{k}\lambda)}{\sigma_2 I_{\nu}(\frac{u_1}{k}\lambda) + \sigma_1 I_{\nu-1}(\frac{u_1}{k}\lambda)}$$



$$K(\lambda) = \frac{K_{\nu}(\frac{c_1}{k}\lambda) - Q I_{\nu}(\frac{c_1}{k}\lambda)}{K_{\mu}(\frac{c_1}{k}\lambda) + Q I_{\mu-1}(\frac{c_1}{k}\lambda)}$$

where

$$Q \triangleq \frac{\sigma_2 K_{\nu}(\frac{u_1}{k}\lambda) K_{\mu-1}(\frac{\omega_1}{l}\lambda) - \sigma_1 K_{\nu-1}(\frac{u_1}{k}\lambda) K_{\mu}(\frac{\omega_1}{l}\lambda)}{\sigma_2 I_{\nu}(\frac{u_1}{k}\lambda) K_{\mu-1}(\frac{\omega_1}{l}\lambda) + \sigma_1 I_{\nu-1}(\frac{u_1}{k}\lambda) K_{\mu}(\frac{\omega_1}{l}\lambda)}$$

$$\nu \triangleq \frac{1-p}{2}, \quad \mu \triangleq \frac{1-q}{2}, \quad u_1 \triangleq c_1 + kz_1, \quad \omega_1 \triangleq c_2 + lz_1$$

THE KERNEL FUNCTION FOR A HORIZONTALLY
LAYERED MEDIUM

The purpose of the following development is to review, discuss, and evaluate the kernel functions for media consisting of an arbitrary number of horizontal layers with constant conductivities. The first publications on this subject appeared in 1928 and 1929 in a series of articles by J. N. Hummel, who established what can be called the "Image School" in electrical prospecting. A general development for the n-layer case was first given by Stefanescu in collaboration with the Schlumberger brothers in 1930, in a paper that created the "Harmonic School." Later development of different expressions and recurrence relations for the kernel function is associated with the names of Slichter (1933), Pekeris (1940), Sunde (1949), Flathe (1955), and Onodera (1960). A review of their work is given by Roman (1963).

Of all the different expressions for the kernel function, two specific recurrence relations, namely Sunde's and Flathe's have been investigated closer in this thesis and

are discussed briefly to point out the difference in the numerical calculation of the kernel function.

Sunde's Recurrence Relation

Equation (24) gives the kernel function for quite general conductivity laws. However, this expression can be greatly simplified for the present case because of the particularly simple relationship between the exponential function and its derivatives.

With $F = e^{-\lambda z}$, $G = e^{\lambda z}$ in the determinant of the system of simultaneous equations (23), the following recurrence relation can be established formally by simple row and column operations:

$$\begin{aligned}
 V_{123 \dots n} &= \frac{1 - k_{123 \dots n} e^{-2\lambda d_1}}{1 + k_{123 \dots n} e^{-2\lambda d_1}} \\
 k_{123 \dots n} &= \frac{\sigma_2 - \sigma_1 V_{234 \dots n}}{\sigma_2 + \sigma_1 V_{234 \dots n}} \\
 V_{234 \dots n} &= \frac{1 - k_{234 \dots n} e^{-2\lambda d_2}}{1 + k_{234 \dots n} e^{-2\lambda d_2}} \\
 k_{234 \dots n} &= \frac{\sigma_3 - \sigma_2 V_{345 \dots n}}{\sigma_3 + \sigma_2 V_{345 \dots n}} \\
 &\vdots \\
 &\vdots \\
 &\vdots \\
 &\vdots
 \end{aligned} \tag{25}$$

⋮
⋮
⋮
⋮
⋮

$$V_{(n-1)n} = \frac{1 - k_{(n-1)n} e^{-2\lambda d_{n-1}}}{1 + k_{(n-1)n} e^{-2\lambda d_{n-1}}}$$

$$k_{(n-1)n} = \frac{\sigma_n - \sigma_{n-1}}{\sigma_n + \sigma_{n-1}},$$

where $V_{123\dots n} = K(\lambda)$ is the kernel function for a medium consisting of n layers, $k_{123\dots n} = k(\lambda)$ is the reflection function, and d_i is the thickness of the i th layer. With the notation of figure 5, $d_i = z_i - z_{i-1}$.

This recurrence relation has been derived by Sunde (1949) in a very elegant way based on the analogy of the present boundary-value problem with a particular transmission line consisting of n different sections having the same propagation constant.

The kernel function $V_{123\dots n}$ is found by a series of substitutions starting at the bottom of the sequence of layers. First $V_{(n-1)n}$ is computed, which corresponds to the kernel of a two-layer case with a top layer of conductivity σ_{n-1} and thickness d_{n-1} resting on an infinite substratum of resistivity σ_n . Next, the kernel of a two-layer case with a top layer of conductivity σ_{n-2} , $V_{(n-1)n}$ and thickness d_{n-1} resting on an infinite half space of conductivity σ_{n-1} is computed, and so on.

In the appendix, the flow chart is shown for a digital computer program of Sunde's recurrence relation (25). The computation time is approximately 0.1 sec_x per layer for each value of the kernel function on the CDC 8090, a machine with a cycle time of 6.3 μsec.

Flathe's Recurrence Relation

Stefanescu and others (1930), wrote the surface potential for a horizontally stratified earth in the following form:

$$U(r) = \frac{I}{2\pi\sigma(o)} \left\{ \frac{1}{r} + 2 \int_0^{\infty} \Theta(\lambda) J_0(\lambda r) d\lambda \right\} . \quad (26)$$

The first term on the right side of equation (26) is known as the primary potential. It is the potential of a homogeneous, semi-infinite half space having the conductivity of the surface layer. The second term is called the disturbing potential; it arises from the presence of layers with different conductivities.

The following relation exists between the "total" kernel function $K(\lambda)$, equation (25), and the "disturbing" kernel function $\theta(\lambda)$, equation (26):

$$K(\lambda) = 1 + 2\theta(\lambda) . \quad (27)$$

Flathe (1955) developed and proved the following recurrence relations for the "disturbing" kernel function $\theta(\lambda)$ in equation (26):

$$\theta_n(\lambda) = \frac{P_n(u)}{H_n(u) - P_n(u)} \quad , \quad (28)$$

where $u = e^{-2\lambda}$, and n denotes the n th layer according to figure 5.

Recurrence relations for $P_n(u)$ and $H_n(u)$ are given by:

$$\begin{aligned} P_{i+1}(u) &= P_i(u) + H_i(u^{-1}) k_i u^{z_i} \\ H_{i+1}(u) &= H_i(u) + P_i(u^{-1}) k_i u^{z_i} \quad , \end{aligned} \quad (29)$$

where $i = 1, 2, 3, \dots, (n-1)$;

and $P_1 = 0, H_1 = 1$.

This recurrence relation is just the opposite of (25), in that successive layers are added at the bottom of the sequence rather than on the top as in the former. Equations (29) are very convenient for obtaining the explicit analytic expression of the kernel function. However, difficulties arise when implementing them for a digital computer because of the inverse functional relationships $P(u^{-1})$ and $H(u^{-1})$. A way to overcome this difficulty has been devised by Mooney and others (1966). Their procedure consists in allowing only integer thicknesses for the layering, which is not a limitation from a practical point of view because actual layer

thicknesses can always be scaled to integer values with a specified accuracy. But, from a computational point of view difficulties arise in small-scale computers because of the storage requirements for large matrices representing $P_n(u)$ and $H_n(u)$.

Van'yan's Recurrence Relation

A very simple recurrence relation for the multi-layered kernel function was given by Van'yan (1959), for the general alternating-current case. Because its direct-current equivalent can be derived directly from Sunde's expressions, it was not implemented for the digital computer. However, analytical compactness makes this formula useful for manual computation of kernels if a table of hyperbolic trigonometric functions is available. Since Van'yan's formula is not well known in the English literature on the subject of resistivity sounding, a short proof of it is given next.

Starting from Sunde's recurrence relation (25), and writing $k = k_{123\dots n}$ in order to simplify, the kernel function for a medium consisting of n layers may be written:

$$V_{123\dots n} = \frac{k^{-\frac{1}{2}} e^{\lambda d_1} - k^{\frac{1}{2}} e^{-\lambda d_1}}{k^{-\frac{1}{2}} e^{\lambda d_1} + k^{\frac{1}{2}} e^{-\lambda d_1}}$$

$$V_{123\dots n} = \frac{e^{\lambda d_1 - \frac{1}{2} \log k} - e^{-(\lambda d_1 - \frac{1}{2} \log k)}}{e^{\lambda d_1 - \frac{1}{2} \log k} + e^{-(\lambda d_1 - \frac{1}{2} \log k)}} .$$

By the definition of the hyperbolic tangent function this expression becomes

$$V_{123\dots n} = \tanh\left(\lambda d_1 + \frac{1}{2} \log \frac{1}{k}\right) ;$$

substituting the expression for k from (25),

$$V_{123\dots n} = \tanh\left(\lambda d_1 + \frac{1}{2} \log \frac{1 + \frac{\sigma_1}{\sigma_2} V_{23\dots n}}{1 - \frac{\sigma_1}{\sigma_2} V_{23\dots n}}\right) .$$

This formula can be further simplified by means of the logarithmic representation of the inverse hyperbolic tangent (Abramowitz and Stegun, 1965, p. 87),

$$V_{123\dots n} = \tanh\left(\lambda d_1 + \operatorname{arctanh} \frac{\sigma_1}{\sigma_2} V_{23\dots n}\right) .$$

The kernel function for the four-layer case shown in figure 4 was computed by Flathe's and by Sunde's algorithms and listed side by side. A comparison of the numerical values of these two functions (Flathe's kernel function being converted by means of relation (27)), shows a small random error with a maximum relative value of 0.074%, which is due to

round-off in the computations. It was established that Sunde's algorithm is twice as fast as Flathe's. Concerning the accuracy of the kernel functions, Sunde's relationship seems to give better numerical values. It was seen, for instance, that the first two entries of Flathe's formula converted to Sunde's expression are too large compared with the theoretical value of the kernel function at zero.

In summary, Sunde's algorithm for the numerical evaluation of the unique kernel function is simpler, faster, and probably more accurate than Flathe's. Therefore, all the tabulated kernel functions used in this thesis are based on the former.

A MODEL STUDY OF KERNEL FUNCTIONS FOR THE ADENA
OIL FIELD, MORGAN COUNTY, COLORADO

In this chapter the properties of kernel functions for a specific multi-layered model are investigated. The purpose is to gain some insight into the resolving power of the kernel function. In other words, how much information on the subsurface layering can be extracted from a given kernel curve? Needless to say that this question is of fundamental importance in the interpretation of resistivity sounding curves. For, assuming that field data are measured and transformed to the λ -domain under ideal conditions of accuracy, the question which then arises is, how accurate a model in terms of number of layers, layer thicknesses, and resistivities can be established?

Because of the contemporary interest in the application of electrical methods to petroleum exploration, a study of synthetic kernel curves over an idealized oil field was undertaken. The oil field model was selected for this study, to take advantage of the tremendous amount of information

on the electrical properties of the subsurface contained in the existing well logs. The apparent resistivities obtained in this way are subject to several errors; mud resistivity in the well bore, well diameter, bed thickness, degree of invasion of the rock, and type of logging array used. All these errors may cause the measured resistivity to differ from the true value. Another point to be considered in the compilation of resistivities from well logs is the electrical microanisotropy, which is an inherent property, especially of sediments, caused by a better conduction of the electric current along the bedding planes than across the bedding planes. A discussion of the influence of these disturbing factors on the kernel function is presented. Keller (1966) has shown statistically, that these errors are consistent, rather than random, from well log to well log; thus in spite of the fact that the actual kernel curves may not be precise, a comparison of them for studying similarities or differences is quite permissible.

General Description of the Adena Field

The Adena field is located 65 miles northeast of Denver and 10 miles south of Fort Morgan, in Morgan County, Colorado. The surface elevation is approximately 4500 feet; the terrain is flat and treeless. The field covers 11425 acres.

and is 7 miles long and 4 miles wide, the average depth is 5650 feet. According to Mygdal (1963, p. 222):

Adena oil field is the giant of the Denver basin; its cumulative production of 53.8 million barrels through 1962 is approximately four times that of the next largest field in the basin and is exceeded in Colorado only by the Rangley.

The sedimentary column is normal for the central Denver basin and could be divided into four geoelectric units as described by Keller (1964, p. 58):

The near surface rocks belong to the Fox Hills member of the Montana Group, underlain by the Pierre Shale member of the Montana Group. The next lower group of beds with consistent electrical properties consists of the Morrison Formation, the Dakota Sandstone, the Benton Formation and the Niobrara Formation. The deepest electrical layer is composed of Paleozoic sedimentary rocks, which contain extensive evaporite deposits in places.

Local structure is monoclinal, with west dips of approximately 50 feet per mile; there is no significant local folding. The trap is entirely stratigraphic; nevertheless the field was discovered in May 1953 by drilling on a small seismic anomaly which was later shown to be unrelated to the monoclinal structure. Oil is produced from the "D" and "J" sands of the Dakota Formation, the latter being by far the more important producer. Mygdal (1963, p. 224) describes the "J" sand reservoir as follows:

The "J" sand is continuous over the region as a massive sand zone containing minor shale breaks. At Adena the top of the zone is approximately

150 feet thick. An upper sand unit, called the "First Bench", is separated from the main sand body by an underlying shale member which thickens eastwards at the expense of the "First Bench". This shale pinches out in the western portion of the field. The "First Bench" thins eastward and becomes more shaly so that eventually its permeability is decreased sufficiently to prevent the escape of oil and gas. This permeability barrier extends south-eastward and up dips along the north edge of the field, then curves south and northwest and finally passes below the oil water contact. The oil moving eastward along the roof of the "J" sand has become trapped above the basal seal which prevents its further movement up dip.

The "First Bench" sand is mostly clean and unbroken without continuous shale layers, thus constituting a single reservoir over the entire field. The thickness of the net pay sand in the oil zone averaged 30 feet with a maximum of 72 feet; the thickness of the gas cap averaged 18 feet.

Figure 6 shows the model on which the computation of the kernel function for the Adena field is based. Surface measurements in the area yield a resistivity of about 10 ohm-m for the surface layer. The resistivities of the section between 110 and approximately 5600 feet were sampled from the short normal curve of selected well logs. The deepest well in the area (Weiss, no.42-32, sec. 32-3N-55W, Morgan County, Colorado), which penetrates the Precambrian basement, shows a thickness of approximately 3000 feet for the Paleozoic rocks underlying the logged zone. The longitudinal resistivity of these rocks lies between 8 and 20

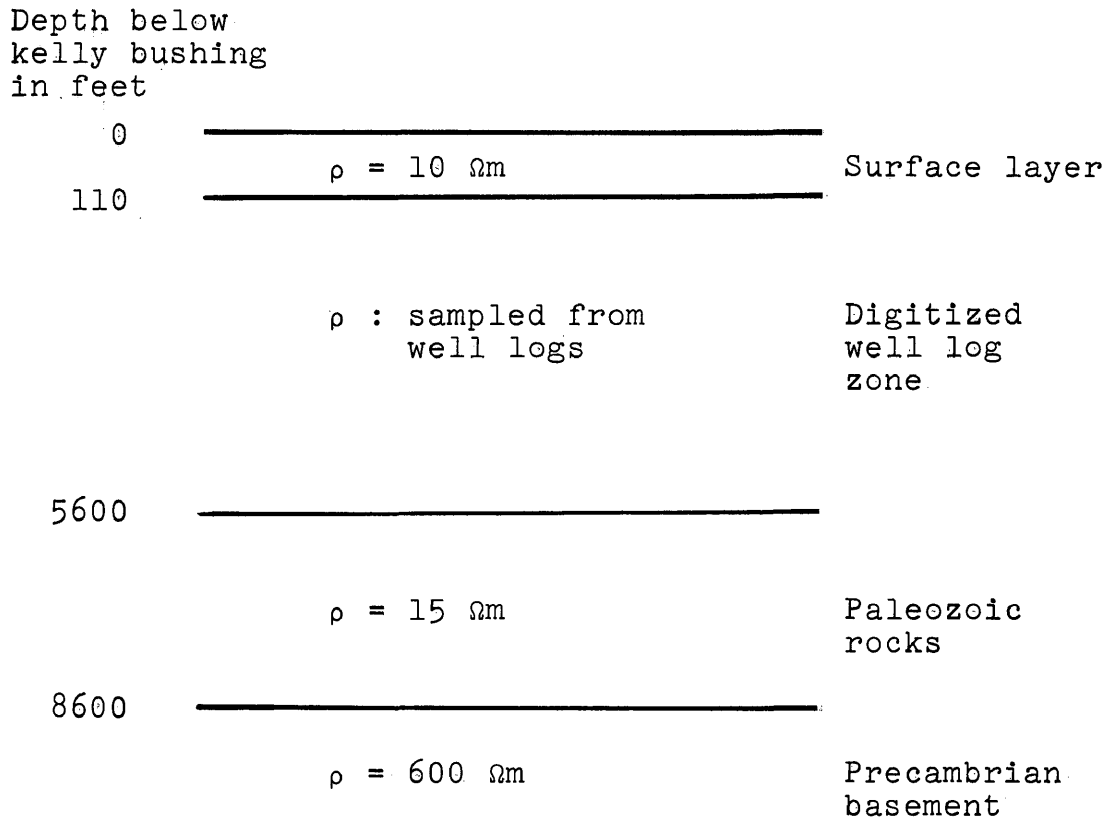


Figure 6.

Geoelectric model for the Adena field

ohm-m (Keller, 1964); for this study an average resistivity of 15 ohm-m was adopted. For the resistivity of the Precambrian basement consisting of a complex of mainly schists and gneisses containing numerous igneous intrusions, a value of 600 ohm-m was chosen.

Figure 7 indicates the locations of the nine well logs selected from the Adena field. The well Pure Oil, Hough no.1

ADENA FIELD
"J" SAND-NET OIL AND GAS ISOPACH
CONTOUR INTERVAL 10'

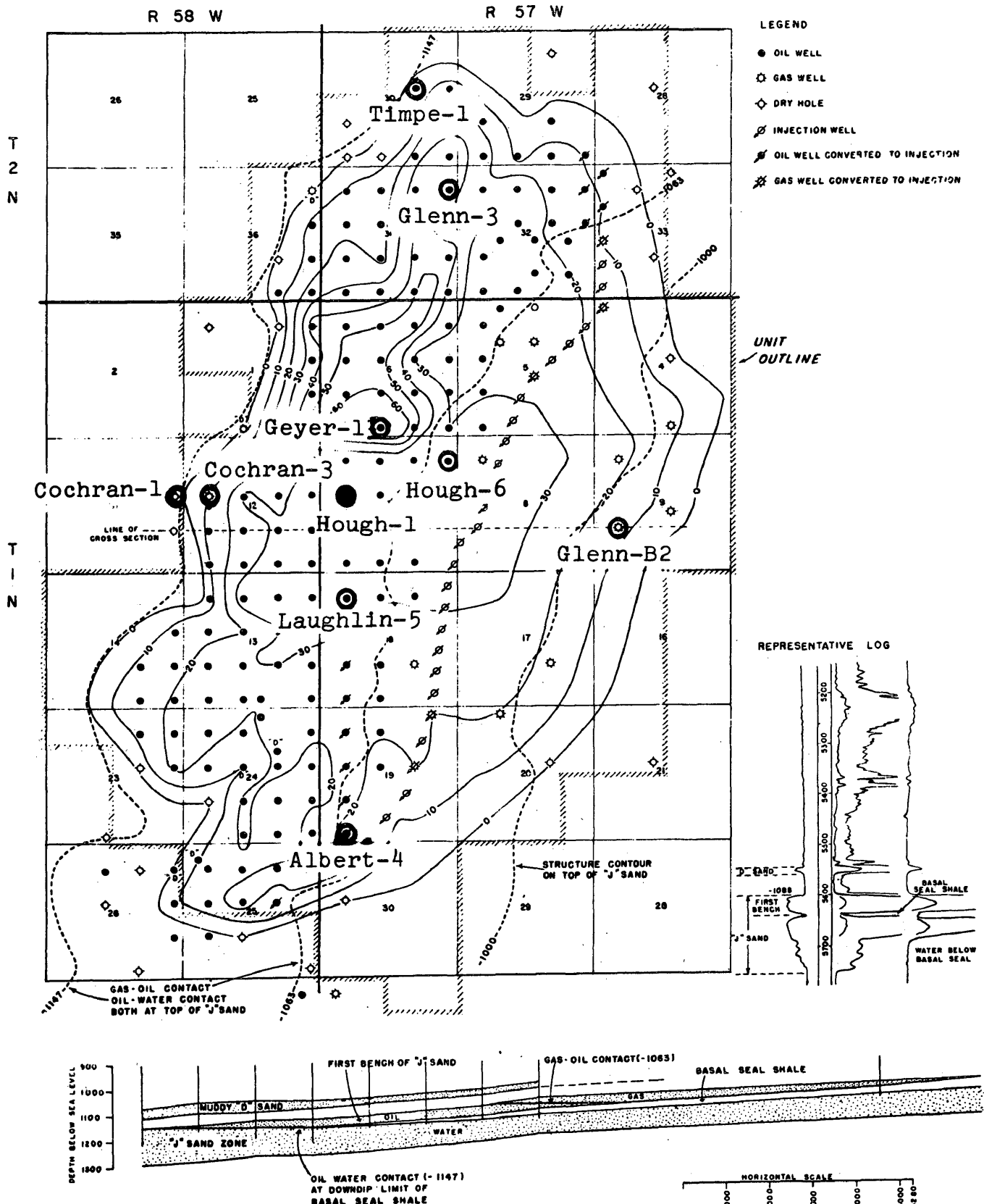


FIGURE - 7
(From Mygdal, 1963)

(Sec. 7-1N-57W, SE-SW-NW) is considered its representative log (Parker, 1961). The upper part of this well log corresponds to the Tertiary and Upper Cretaceous rocks with a fairly uniform resistivity of 4 to 5 ohm-m. The transition to the Pierre Shale having an almost constant resistivity of approximately 2 ohm-m is gradual. A sharp break is observed at the top of the Niobrara, 4710 feet below the kelly bushing. The Niobrara, Benton, and Dakota Formations are characterized by rapid changes in their resistivities in the range 2 to 10 ohm-m. On this background, the "D" sand produces a ten-foot thick anomaly of about 20 ohm-m, (5550 feet below the kelly bushing). The "First Bench" of the "J" sand shows up as an anomaly of 100 ohm-m with a thickness of 35 feet. The following analysis is based on this representative log.

The Kernel Functions for the Adena Oil Field

1. Effect of sampling interval.-- The short normal electric log of Hough no.1 was sampled with a ten-foot interval, and the kernel for layer thicknesses of 50, 20, and 10 feet were computed, the latter being shown in figure 8. Table IV shows the maximum absolute and relative errors, and the root mean square deviation of the 50 and 20 foot interval kernels from the 10-foot interval kernel. Both maximum absolute errors occur in the vicinity of $\lambda = 5 \times 10^{-6}$ and are

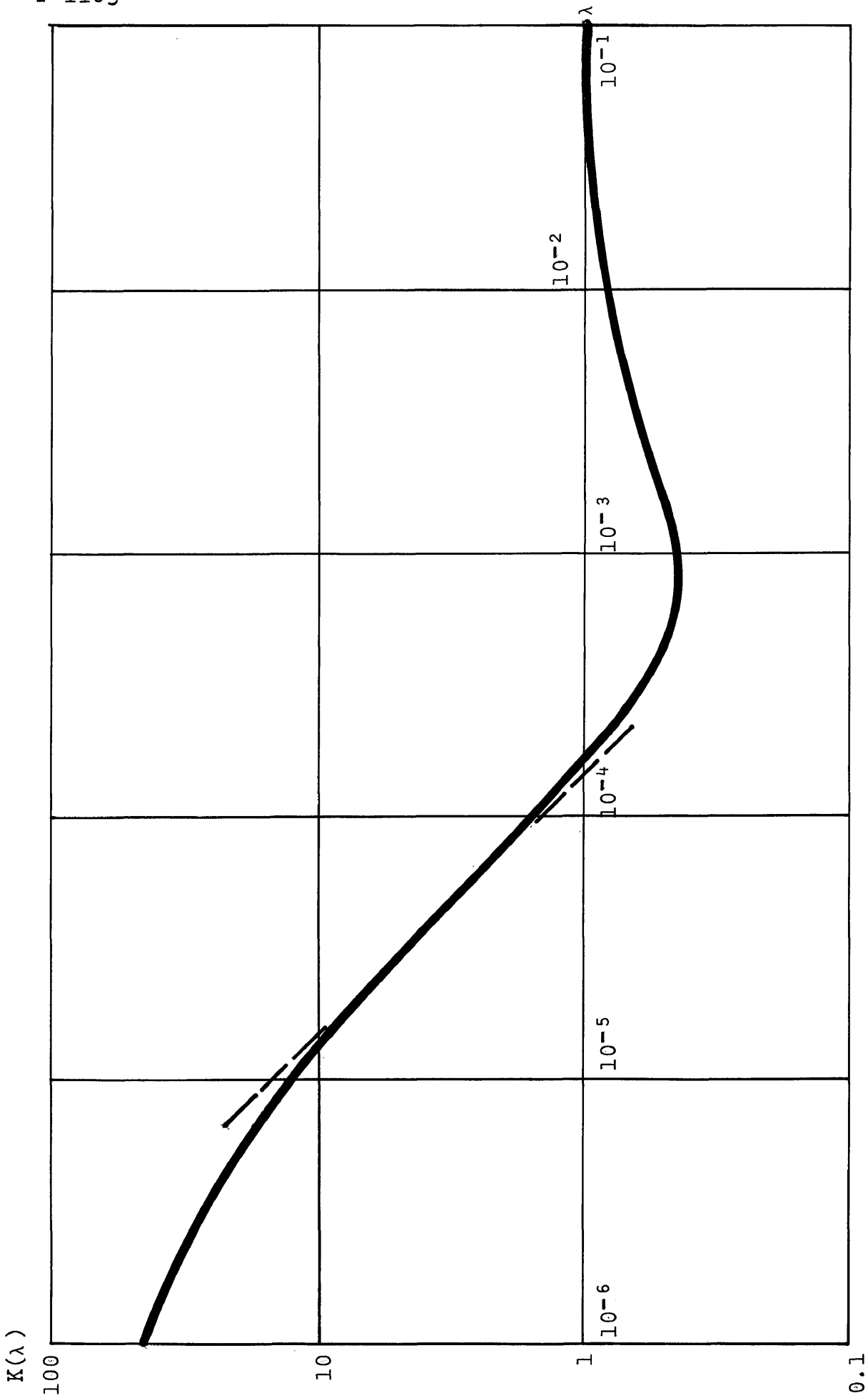


Figure 8.
Kernel function computed from Hough no.1, Adena, electric log
digitized with a ten-foot interval

produced by imperfect sampling of the Niobrara, Benton, and Dakota Formations. The maximum relative errors are too small to show the discrepancies between the kernel curves when plotted on the scale of figure 8.

Table IV.

Effect of 50- and 20-foot sampling intervals of the kernel functions as compared to 10-foot sampling interval

Sampling interval in feet	Max. ampl. of absolute error curve	Maximum absolute error	Maximum relative error	Root mean square deviation
50	0.146	-0.10	2.6 %	0.038
20	0.138	-0.13	-0.9 %	0.047

For the computation of kernel functions a 10-foot interval was used throughout, which yields sufficiently accurate results within the limitations of the general procedure discussed above.

2. Effect of random noise in the resistivities.-- The effect of possible slight errors made during measurements or sampling of the log was estimated by changing a few of the recorded resistivity values arbitrarily by plus or minus five percent. The overall effect of these changes on the kernel curve is negligible (maximum relative error 0.005 percent).

3. Equivalent layers for the geoelectric section.-- A hypothetical 557-layer case is obtained by digitizing the Hough no.1 electric log every ten feet. However, many of these layers may be lumped together using the principle of equivalence (Maillet, 1947). This principle states that an anisotropic layer of thickness h , and longitudinal resistivity ρ_l and transverse resistivity ρ_t is equivalent in its outside effects, within a given range of error, to an isotropic layer of thickness θh (equivalent thickness), and resistivity ρ (equivalent resistivity). Here $\theta = \sqrt{\rho_t/\rho_l}$ is the coefficient of anisotropy, and $\rho = \sqrt{\rho_l \times \rho_t}$ is the average resistivity.

A computer program was written to generate equivalent thicknesses and resistivities from digitized electric logs. The selection of the anisotropic sections to be transformed into isotropic layers was based in part on sampling with specified intervals, in part on natural breaks in the apparent resistivities of the short normal curve. Over 50 equivalent kernels were evaluated and compared with the original 557-layer kernel of Hough no.1. Each equivalent model is labeled by the number of layers and an identifier. For instance, layer case (6-3) means model no.3 consisting of six layers. The degree of fit of the equivalent with the original kernel curve was measured in terms of the following error criteria:

a). maximum amplitude of the absolute error curve

$$\text{MAX}[K_s(\lambda) - K_e(\lambda)] - \text{MIN}[K_s(\lambda) - K_e(\lambda)] ,$$

b). maximum absolute error

$$\text{MAX}[K_s(\lambda) - K_e(\lambda)] ,$$

c). maximum relative error

$$\text{MAX} \left[\frac{K_s(\lambda) - K_e(\lambda)}{K_s(\lambda)} \right] ,$$

d). root mean square deviation

$$\left[\sum_{i=1}^n \frac{[K_s(\lambda_i) - K_e(\lambda_i)]^2}{n} \right]^{1/2} ,$$

where $K_s(\lambda)$ denotes the 557-layer, $K_e(\lambda)$ the equivalent kernel, and n is the number of tabulated values of the kernel function.

Only the maximum relative error proved to be of practical value, because if the curves are plotted on a regular 8.5-by 11-inch logarithmic paper, a 2 percent departure is the threshold for clear distinction between them.

Figure 9 presents the original electric log, sampled with a 20-foot interval, and some of its equivalent models. The fit of the five-layer kernel which divides the well log section into two isotropic layers, with the 557-layer kernel is shown in figure 10. The maximum relative departure between the two curves is 3.4 percent. The degree of fit of the other equivalent models drawn in figure 9 is better than 2.5 percent and differences between original and equivalent kernel curves are hardly detectible on the scale of figure 10.

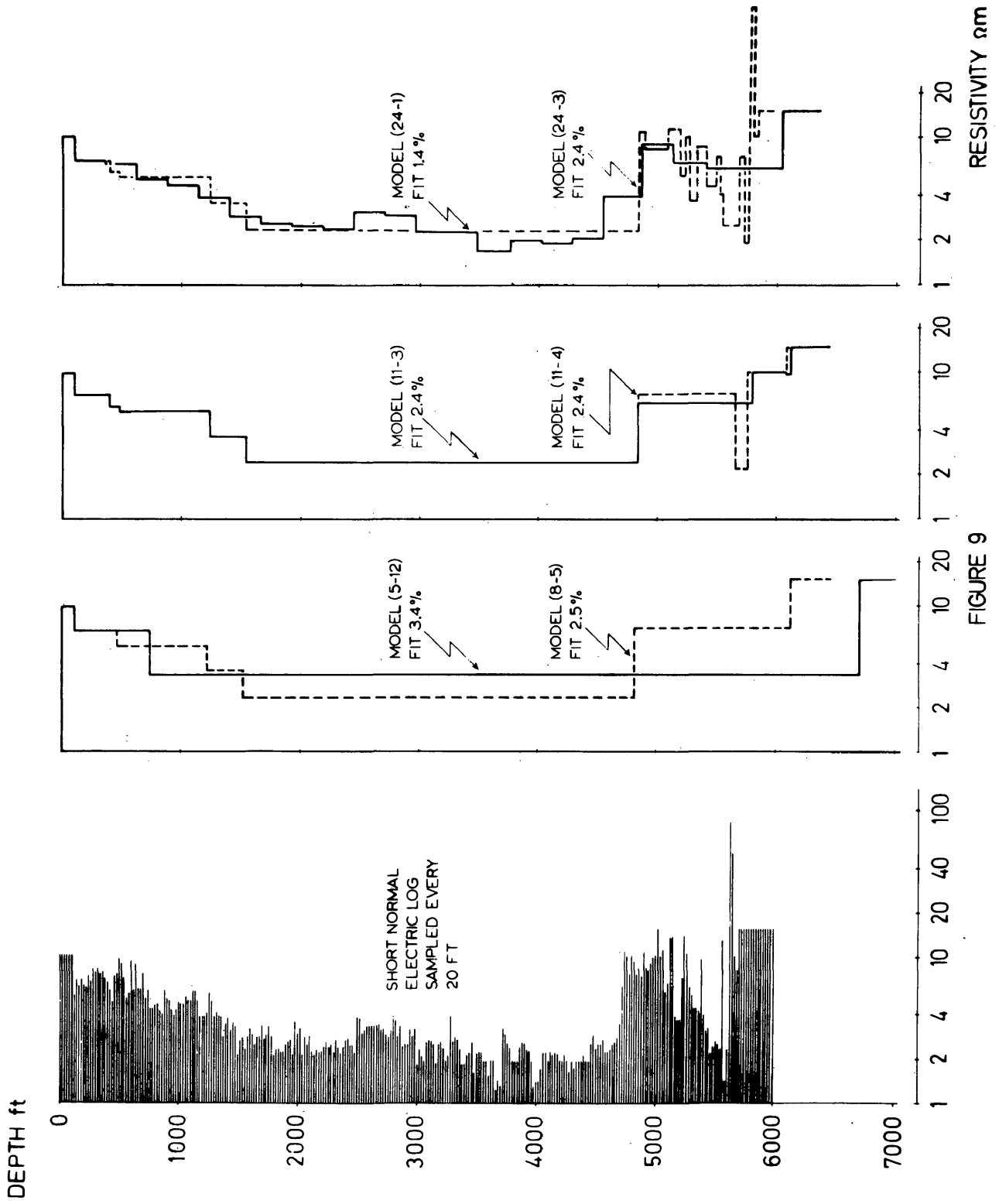


FIGURE 9

HOUGH NO. 1 ADENA, ELECTRIC LOG AND SOME EQUIVALENT MODELS

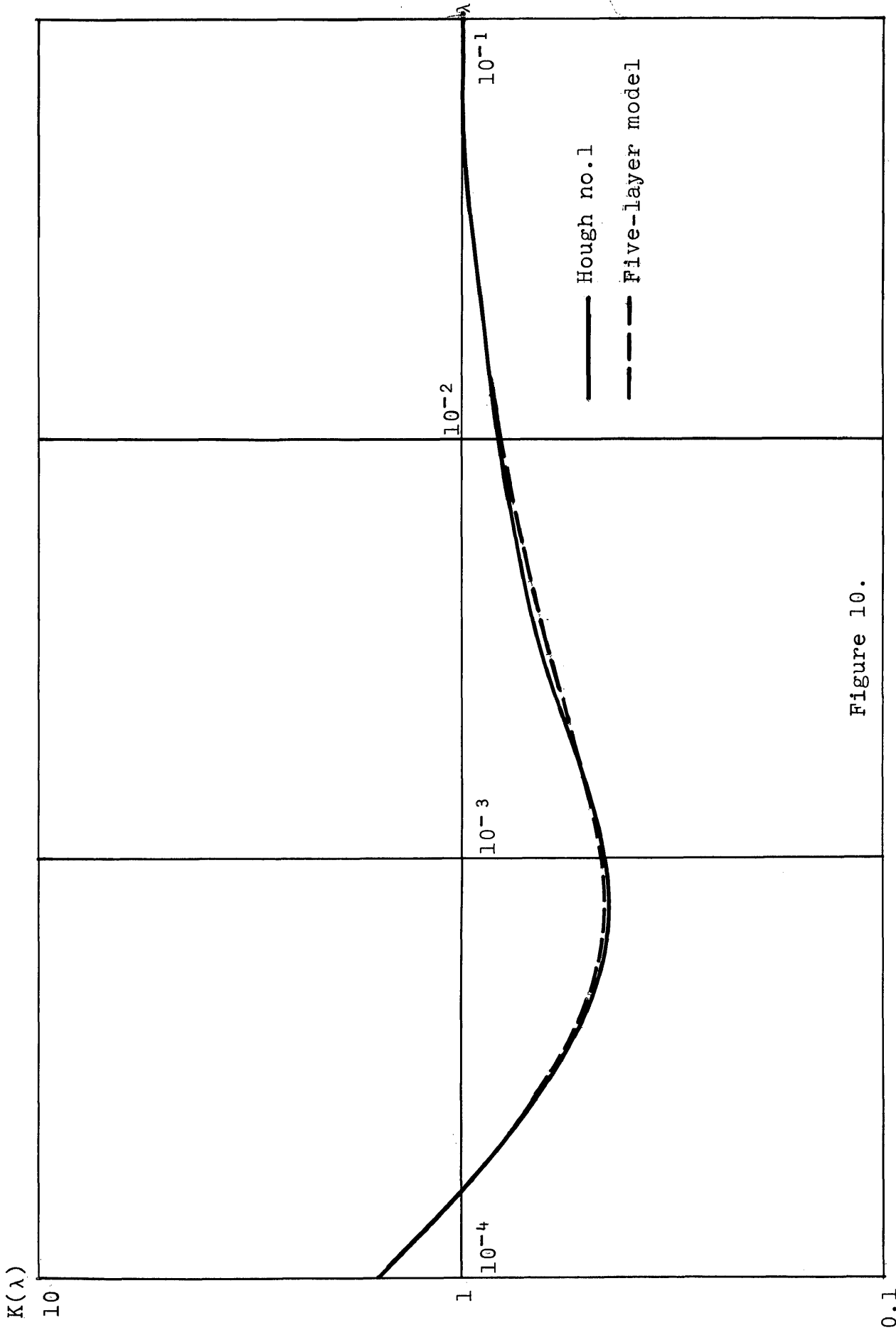


Figure 10.

Comparison of the kernel function from the digitized electric log of Hough no.1, Adena, with the five-layer model (5-12)

Keeping the number of layers fixed the overall fit of the equivalent models can be improved considerably by subdividing the upper part of the log, (Tertiary and Pierre). Even if the general appearance of the electric log between 110 and 4700 feet is rather uniform compared with the remaining section, individual layers of this lower part, with strong resistivity contrasts, do not contribute significantly to the kernel function. This observation was well illustrated by the equivalent models (24-1) and (24-2). The former was computed by sampling the whole length of the section with a fixed interval of 260 feet; the fit with the original 557-layer model is better than 1.4 percent. The latter represents the section between 110 and 4710 feet by one layer, from there on a sampling interval of 50 feet was taken; the maximum relative error is 39 percent. This general insensitivity of the kernel function to deep resistivity variations is further substantiated by cases (11-3) and (11-4), where different subdivisions of the section below 4710 feet do not affect the overall fit.

This feature of the kernel functions means that in the interpretation of the type of curves representing the Adena field section, the layering parameters of the upper few hundred feet only, could be found with reasonable accuracy from sounding data alone. The need for additional information is

also drastically demonstrated by figure 9, where all the different layering models could be considered valid interpretations.

This figure also illustrates graphically that without knowledge of the coefficient of anisotropy for the individual layers a correct interpretation of their thicknesses is impossible.

In order to test the principle of equivalence, the kernel functions for models (6-2) and (40) have been evaluated using true thicknesses, transverse and longitudinal resistivities. The errors resulting from comparison with the standard curve show that selecting longitudinal resistivities produces better fits than choosing transverse resistivities. Nevertheless, the fit of the equivalent layer curves is still better than the fit of the corresponding longitudinal resistivity curve.

4. Detection of a target layer.-- The oil-producing zones of the Adena field ("D" sand and "First Bench" of "J" sand) are represented on the Hough no.1 well by two resistant layers, 10 and 30 feet thick, respectively. Located approximately 5500 feet below the kelly bushing, they have resistivities 10 times ("D" sand) and 50 times ("First Bench") the background value. These layers produce on the surface

kernel function a maximum deflection of 0.154 or 1 percent with a root mean square deviation of 0.057. In table V, this anomaly is shown as even smaller in some of the other well logs nearby. The effect of these target layers in the equivalent models is almost exactly the same as in the standard model. Consequently, an accuracy of the kernel curve much better than 1 percent is required to detect the presence of these beds. Unfortunately, even if the measurements of field data and their transformation to the λ -domain would meet this accuracy requirement, it does not mean that the existence of the high resistant layers could be established from the knowledge of the kernel function alone. As shown in the preceding section, some additional information is necessary, either in the form of the coefficient of anisotropy, or depths of the beds.

Table V.

Comparison of kernel functions without "D" and "J" sand
in the section with the original kernel function

Well	Total thickness in m	Transverse resistance in Ωm^2	Total conductance in mhos	Maximum relative error
Hough no.1	2646	20778	637.2	0.98 %
Hough no.6	2624	21354	567.4	0.20 %
Geyer no.1	2643	21073	615.7	0.68 %

5. Lateral variation of the kernel function.-- Table VI compares the kernel function for Hough no.1 with eight kernel functions obtained from four wells on a N-S and four wells on a W-E line (see figure 7). There is no uniform trend in the error indicator so that the variation must be attributed to lateral changes of resistivities rather than lateral changes of depths due to dipping beds.

Table VI.

Comparison of the kernel function for
Hough no. 1 with the kernel functions
for some surrounding wells

Well	Total thickness in m	Transverse resistance in Ωm^2	Total conductance in mhos	Maximum relative error
Cochran 1	2679	21197	621.8	2.9 %
Cochran 3	2667	21167	628.4	2.1 %
Hough 6	2624	22438	566.3	-11. %
Glenn B-2	2603	21032	584.5	- 7.4 %
Timpe 1	2630	21577	565.2	-20. %
Geyer 1	2642	21919	611.3	3.9 %
Laughlin 5	2646	22677	570.3	-10. %
Albert 4	2664	21078	616.7	6.3 %

Changes in resistivity or thickness of the target layers do not account for the observed errors. For instance, the "First Bench" of Hough no.6 has a resistivity of 150 ohm-m compared with a resistivity of 100 ohm-m for this bed in

Hough no.1. However, this increase in resistivity does not produce any noticeable effect on the relative error listed in table VII. Similarly, the Geyer no.1 log shows a "First Bench" twice as thick as Hough's no.1, and yet it is seen from the table that this effect is also negligible compared with the total deflection of the kernel curve. Hence, it must be concluded that the lateral changes in the value of the kernel function are produced by changes in the resistivities along the whole section of the log.

Table VII.

Comparison of the kernel function for Hough no.1 with the kernel functions for two wells without "D" and "J" sand

Well	Total thickness in m	Transverse resistance in Ωm^2	Total conductance in mhos	Maximum relative error
Hough no.6	2624	21354	567.4	-11. %
Geyer no.1	2642	21073	615.7	3.9 %

6. The effect of the disturbing factors in well logging on the true rock resistivities.-- The current method of correction for the apparent resistivities obtained by the various logging devices is based on the use of nomographs and master charts. This procedure, oriented towards the evaluation of individual layers, is too cumbersome for the

correction of a whole section consisting of hundreds of beds. It is, therefore, possible to get only an estimate of the influence of the disturbing factors for certain typical sections of the well log. For this purpose the Hough no.1 electric log has been divided into three parts, each with consistent electrical properties. Table VIII compares the geoelectric parameters computed with the short and long normal arrays. Figures 11 to 14 show the probability density and distribution curves for the corresponding resistivities.

Table VIII.

Comparison of the geoelectric parameters measured
with the short and long normal arrays.

Short normal array section (ft)	Transverse resistance in Ωm^2	Total conductance in mhos	ρ_t (Ωm)	ρ_l (Ωm)	θ
110 - 1500	2322.2	84.5	5.48	5.01	1.045
1500 - 4710	2379.8	424.9	2.43	2.30	1.027
4710 - 5680	2790.7	56.8	9.43	5.20	1.347
Long normal array section (ft)					
110 - 1500	2113.7	112.9	4.98	3.75	1.153
1500 - 4710	1634.6	623.6	1.67	1.59	1.031
4710 - 5680	2780.9	79.6	9.40	3.71	1.591

ρ_t : transverse resistivity
 ρ_l : longitudinal resistivity
 θ : coefficient of anisotropy

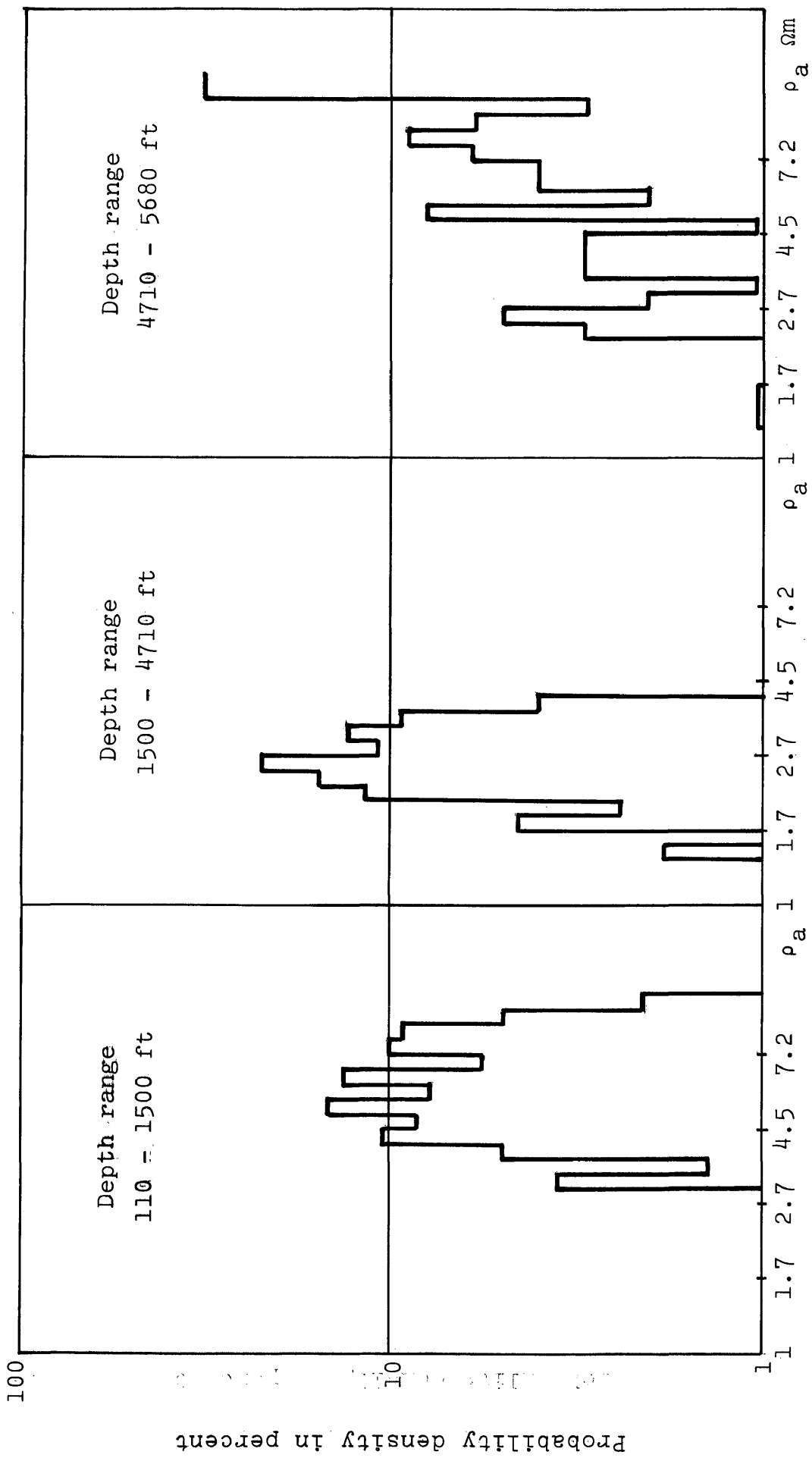


Figure 11.
 Probability density for Hough no.1, Adena,
 short normal resistivity

Probability density in percent

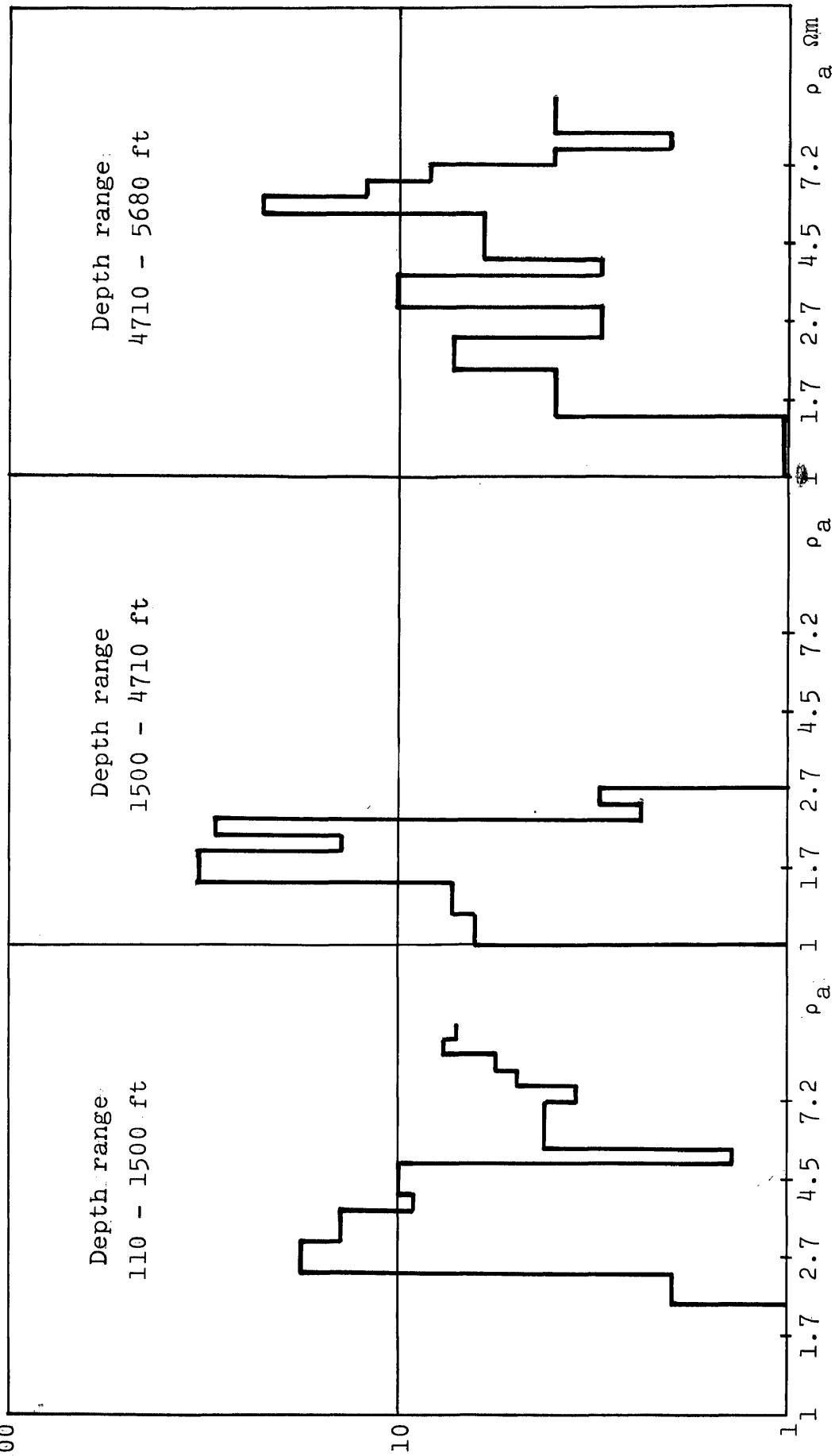


Figure 12.

Probability density for Hough no.1, Adena,
long normal resistivity

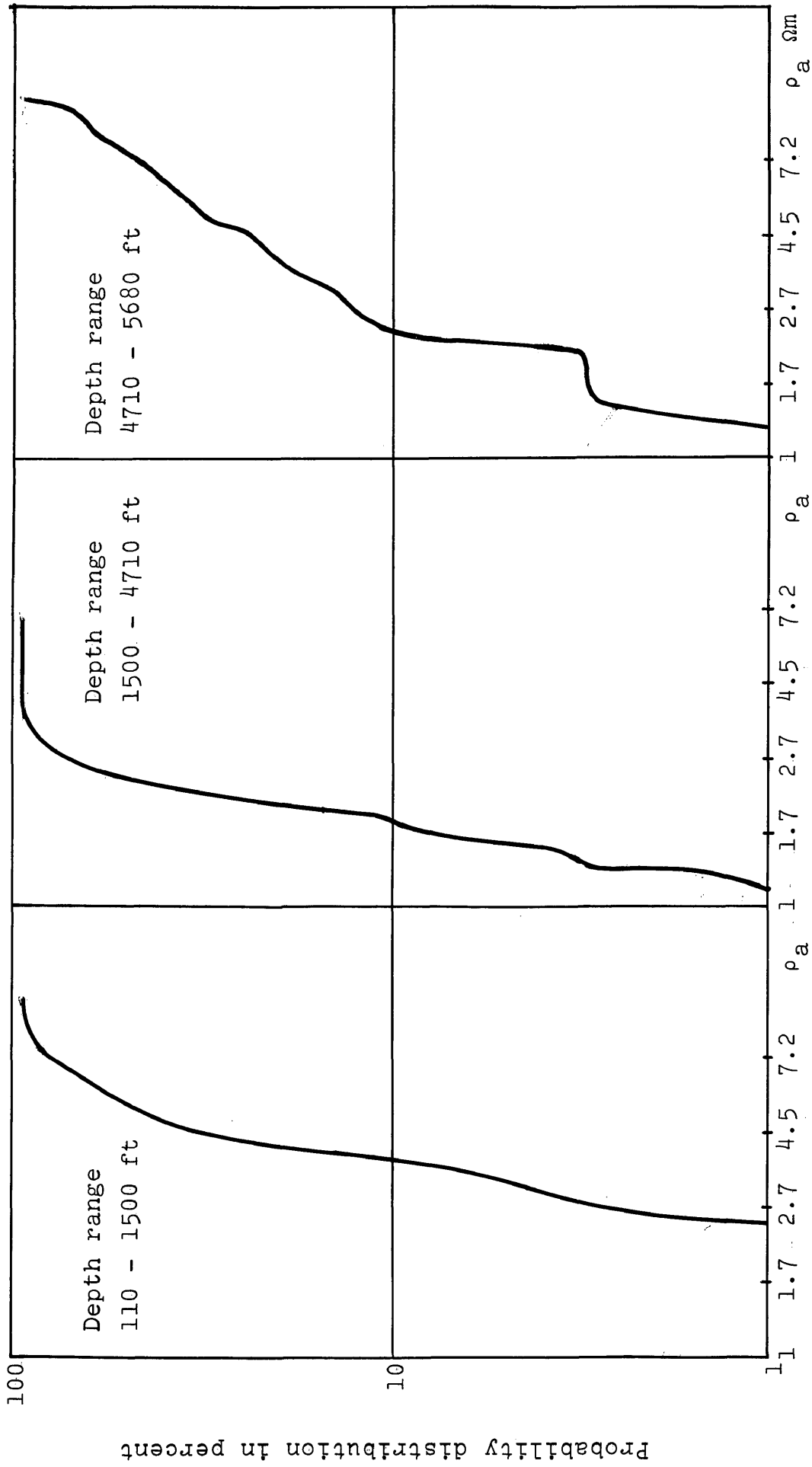


Figure 13.

Probability distribution for Hough no.1, Adena,
short-normal resistivity

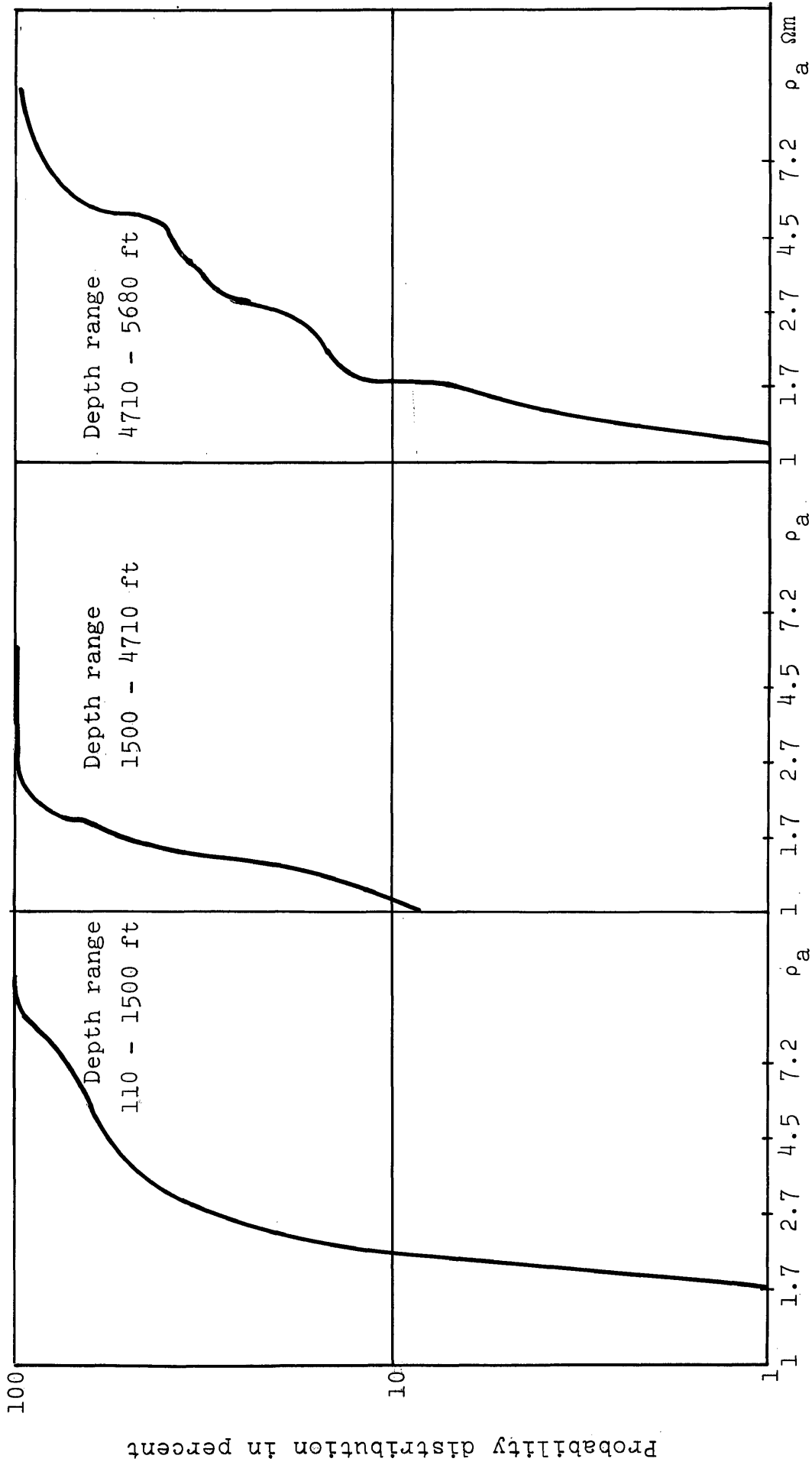


Figure 14.

Probability distribution for Hough no.1, Adena,
long normal resistivity

The probability density curves (figures 11 and 12) of the first two sections are very narrow and peak at low resistivity values. These characteristics indicate uniform electrical properties with no large resistivity contrasts, which is further confirmed by their coefficients of anisotropy θ (table VIII). Therefore; corrections for hole diameter, bed thickness, and adjacent beds are negligible for the first two units. It can be observed on the well log that the short normal and lateral curves are almost coincident over long portions of the record. This circumstance means that if there is any significant invasion at all, the invaded zone has approximately the same resistivity value as the true rock resistivity and no corrections are necessary.

The prominent bed in the third section is the "J" sand unit which presents a significant resistivity contrast with respect to the surrounding rocks. The correction of its apparent resistivity for hole diameter, mud resistivity, bed thickness, and adjacent-bed effects, made with the Lane Wells correction charts (Pirson, 1963), is negligible. The correction for mud-filtrate invasion effects could not be applied because the values of the resistivities fall outside the range of the departure tables. The value of about 110 ohm-m obtained from the lateral log is probably a good estimate for the resistivity of the "J" sand.

The influence of the logging device was tested by computing the kernel function for the Hough no.1 well from long normal resistivities sampled with a 10-foot interval. Comparison with the corresponding short normal kernel curve shows a maximum deflection of 27 percent. In spite of this difference the "J" and "D" sand units still produce a 1 percent anomaly as in the short normal curves, illustrating once more that the exact kernel curve is not necessary for comparison.

As pointed out earlier, the microanisotropy is an inherent property of rocks primarily because of their intimate structure. Its magnitude can not be evaluated in situ by either surface or bore-hole resistivity surveys where the current is flowing essentially in one direction. Laboratory determinations are of questionable value as long as the conditions of temperature, pressure, and fluid content of the original sample are not reproduced accurately.

The effect of the microanisotropy is to increase the general anisotropy θ , which increases the equivalent thicknesses of the geoelectric units by the same factor. According to Schlumberger and others (1934), this increase may be by a factor as high as 1.2 or 1.3 in some instances. The overall effect of microanisotropy on the preceding comparison study of kernels would decrease the magnitude of the

the error criteria defined on page 59. For illustration, the magnitudes of the error criteria for the "D" and "J" sand units in the Hough no.1 section with different values for the coefficient of anisotropy of the Paleozoic rocks are listed in table IX.

Table IX.

Effect of anisotropy θ of the Paleozoic rocks in Hough no.1 on the "D" and "J" sand anomalies

θ	Maximum absolute error	Maximum relative error	Root mean square deviation
1	0.154	0.979 %	0.0570
2	0.142	0.908 %	0.0520
3	0.131	0.855 %	0.0479

Interpolation of the Kernel Function

The kernel functions discussed in the preceding sections were all tabulated with a constant, multiplying increment of the argument equal to $\sqrt[3]{10}$ (i.e. three values of $K(\lambda)$ per decade of λ). It was established that this spacing is adequate to guarantee the validity of the resulting conclusions by doubling the spacing to six values per decade for some of the computations, without introducing significant changes in the numerical values of the error criteria.

From a different point of view, the kernel function should be tabulated with a spacing such that polynomial interpolation of a given order yields a specified accuracy in the numerical values. This criterion is of practical importance in dealing with geoelectrical sections consisting of numerous layers, for instance digitized well logs, because of a considerable saving in computing time.

A digital computer program for polynomial interpolation based on divided differences techniques was developed and applied to several tabulated kernel functions obtained from the electric log of the Hough no.1 well, Adena. However, for the adopted models, serious difficulties arise in interpolating near the origin. It was shown earlier that the kernel function is singular at the origin if the lowest layer is a perfect resistor. This singularity implies that higher order derivatives become very large near that point, and so does the error of the polynomial approximation, which is a function of some suitable higher derivative. Numerically, it is bad enough that the lowest layer has a large, but finite resistivity (like 600 ohm-m in the Adena field section compared with 4 ohm-m for the overlaying layers) in order to produce this effect. To illustrate the point, the divided difference table for Hough no.1, equivalent model (6-2) is shown in table X.

Table X.

Divided difference table near the origin of the kernel function for Hough no.1, equivalent model (6-2)

λ	$K(\lambda)$	[i]	[ii]	[iii]	[iv]	[v]
1×10^{-8}	59.774					
		-2.25×10^7				
2×10^{-8}	59.549		7.89×10^{12}			
		-2.23×10^7		4.66×10^{19}		
3×10^{-8}	59.325		9.29×10^{12}		-2.15×10^{27}	
		-2.22×10^7		-3.94×10^{19}		5.90×10^{34}
4×10^{-8}	59.104		8.10×10^{12}		8.01×10^{26}	
		-2.20×10^7		-7.39×10^{20}		
5×10^{-8}	58.884		7.88×10^{12}			
		-2.18×10^7				
6×10^{-8}	58.666					

The following relation holds between the fifth divided difference [v] of this table and the fifth derivative $K(\lambda)$

$$[v] = \frac{1}{5!} K^{(5)}(\xi), \quad 10^{-8} \leq \xi \leq 6 \times 10^{-8}.$$

It is seen in table X that higher differences increase rapidly in value and become unstable in their signs. Comparison with the exact values of higher derivatives shows a two-figure agreement between the first derivative and first difference. However, discrepancies between divided

differences and derivatives become increasingly larger for higher orders because of the inherent limitations of the CDC 8090 computer, so that the fifth difference as shown in table X is numerically meaningless. Consequently, only low-order interpolation (up to cubic) can be used on this computer for the particular model under consideration. Closer spacing of the tabulated values of the kernel function is required to improve the accuracy of interpolation.

THE NUMERICAL EVALUATION
OF HANKEL TRANSFORMS

The kernel function $K(\lambda)$ defined by equation (10ii) gives the complete and unique description of the electrical direct-current properties of an isotropic half space having cylindrical symmetry. However, electrical measurements are made in the "r" (distance) domain, yielding the potential, the electrical field, or the curvature of the field; direct measurements of $K(\lambda)$ in the " λ " domain are not feasible. The passage from either one to the other domain is accomplished by the Hankel transformation. The following sections deal with the transformation from the λ to the r-domain, or in other words, the computation of synthetic resistivity sounding curves.

The Apparent Resistivity for some Common Arrays

It is customary in resistivity prospecting to convert the variables measured in the field to apparent resistivities ρ_a . This term is defined as the resistivity of the

homogeneous half space which would produce the observed electrical quantity for a given spacing of the measuring array. This concept may be illustrated with the example of the potential measured around a single-current electrode as given by equation (10i). If the ground is assumed homogeneous for a given spacing r , i.e. $K(\lambda) = 1$, then the surface resistivity $\rho(0)$ is constant for the entire half space. The value of this constant resistivity is called the apparent resistivity measured with the array for the particular spacing r .

With these definitions equation (10i) becomes

$$U(r) = \frac{I \rho_a(r)}{2\pi} \int_0^{\infty} J_0(\lambda r) d\lambda$$

$$U(r) = \frac{I \rho_a(r)}{2\pi r} \quad (30)$$

The apparent resistivity is computed from the field data as

$$\rho_a(r) = 2\pi r \frac{U(r)}{I} \quad , \quad (31)$$

replacing $U(r)$ by its expression (10i)

$$\rho_a(r) = r \rho(0) \int_0^{\infty} K(\lambda) J_0(\lambda r) d\lambda \quad .$$

With $\Phi(\lambda)$, the modified kernel function defined on page 23, the normalized apparent resistivity measured with the single-pole array can be rewritten

$$\rho_a(r)/\rho(0) = 1 + r \int_0^{\infty} \Phi(\lambda) J_0(\lambda r) d\lambda \quad (33)$$

The normalized apparent resistivities for some common arrays obtained in a similar way are listed in table XI.

From the expressions in this table, it is seen immediately that for small spacings the apparent resistivity approaches the value of the surface resistivity,

$$\lim_{r \rightarrow 0} \rho_a(r) = \rho(0) \quad (34)$$

If the resistivity is constant from a certain depth z_n on, i.e.

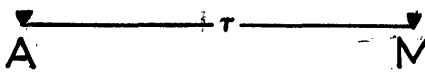
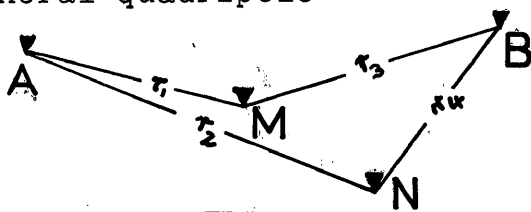
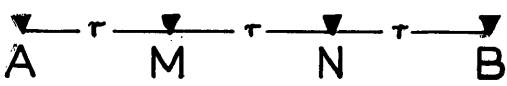

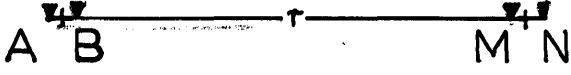
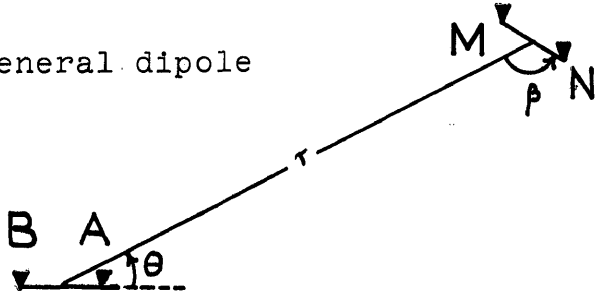
$$\rho(z) = \rho(z_n) \quad z \geq z_n,$$

then the apparent resistivity for any array in table XI approaches the lowermost constant resistivity for large spacings,

$$\lim_{r \rightarrow \infty} \rho_a(r) = \rho(z_n) = \rho(\infty) \quad (35)$$

Table XI.

Apparent resistivities for several arrays

Array	Normalized apparent resistivity $\rho_a(r)/\rho(0)$
<p>Single pole</p> 	$1 + \tau \int_0^{\infty} \Phi(\lambda) J_0(\lambda r) d\lambda$
<p>General quadripole</p> 	$1 + \frac{1}{\frac{1}{r_1} - \frac{1}{r_2} - \frac{1}{r_3} + \frac{1}{r_4}} \int_0^{\infty} \Phi(\lambda) \times \{J_0(\lambda r_1) - J_0(\lambda r_2) - J_0(\lambda r_3) + J_0(\lambda r_4)\} d\lambda$
<p>Wenner</p> 	$1 + 2\tau \int_0^{\infty} \Phi(\lambda) \{J_0(\lambda r) - J_0(2\lambda r)\} d\lambda$
<p>Schlumberger or equatorial dipole</p> 	$1 + \tau^2 \int_0^{\infty} \lambda \Phi(\lambda) J_1(\lambda r) d\lambda$
<p>Polar dipole</p> 	$1 + \frac{\tau^2}{2} \int_0^{\infty} \lambda \Phi(\lambda) J_1(\lambda r) d\lambda - \frac{\tau^3}{2} \int_0^{\infty} \lambda^2 \Phi(\lambda) J_0(\lambda r) d\lambda$
<p>General dipole</p> 	$1 + \tau^2 \frac{\cos(\theta - \beta)}{2 \cos \theta \cos \beta + \sin \theta \sin \beta} \int_0^{\infty} \lambda \Phi(\lambda) J_1(\lambda r) d\lambda + \tau^3 \frac{\cos \theta \cos \beta}{2 \cos \theta \cos \beta + \sin \theta \sin \beta} \int_0^{\infty} \lambda^2 \Phi(\lambda) J_0(\lambda r) d\lambda$

The proof of (35) follows directly from the asymptotic expansion for the apparent resistivities presented in equations (48) through (50).

The Fundamental Integral in the Expressions for Apparent Resistivities

Table XI shows that the r-domain expression of $\Phi(\lambda)$ depends on the geometrical configuration of the measuring electrode array. The apparent resistivities for the arrays commonly used in electrical prospecting are functions of the following three integrals:

$$H_1(\tau) = \int_0^{\infty} \Phi(\lambda) J_0(\lambda\tau) d\lambda \quad , \quad (36)$$

for potential arrays (single-pole, Wenner, Lee, etc.);

$$H_2(\tau) = \int_0^{\infty} \lambda \Phi(\lambda) J_1(\lambda\tau) d\lambda \quad , \quad (37)$$

for electric field arrays (Schlumberger, equatorial-dipole);

$$H_3(\tau) = \int_0^{\infty} \lambda^2 \Phi(\lambda) J_0(\lambda\tau) d\lambda \quad , \quad (38)$$

for curvature arrays (polar-dipole, general dipole).

A general expression for these integral transforms is

$$H_{k'}(\tau) = \int_0^{\infty} \Phi(\lambda) \lambda^{\mu} J_{\nu}(\lambda\tau) d\lambda \quad (39)$$

$k = 1, 2, 3; \mu = 0, 1, 2; \nu = 0, 1.$

There are two basic approaches to the numerical evaluation of formula (39): expansion of the integral in an infinite series, or numerical quadrature. Series expansions may be used for computing the integral transforms (39) for small and large values of r .

In the first case $J_{\nu}(\lambda r)$ is replaced by its ascending power series (Abramowitz and Stegun, 1965, p. 360), yielding the following expansion:

$$H_{k'}(\tau) = \left(\frac{1}{2}\tau\right)^{\nu} \sum_{m=0}^{\infty} \frac{(-1)^m}{m!(m+\nu)!} \left(\frac{\tau}{2}\right)^{2m} \int_0^{\infty} \lambda^{\mu+\nu+2m} \Phi(\lambda\tau) d\lambda, \quad (40)$$

with the change of variable $\lambda r = x$ this formula becomes

$$H_{k'}(\tau) = \left(\frac{1}{2}\right)^{\nu} \left(\frac{1}{\tau}\right)^{\mu+\nu} \sum_{m=0}^{\infty} \frac{(-1)^m}{m!(m+\nu)! 2^{2m}} \int_0^{\infty} x^{\mu+\nu+2m} \Phi(x) dx. \quad (41)$$

For a horizontally stratified medium consisting of n layers, it follows from Sunde's recurrence relation (25), that

$$\Phi\left(\frac{x}{\tau}\right) = -2 \frac{k_{12\dots n} e^{-2xd_1/\tau}}{1 + k_{12\dots n} e^{-2xd_1/\tau}}, \quad \text{where } |k_{12\dots n}| < 1,$$

which shows that the rate of convergence of the integral in (41) is determined by the rate at which $x^{\mu+\nu+2m} e^{-2xd_1/r}$ approaches zero. Hence, formula (41) will be of practical use only if d_1/r is kept large, so that a few terms of the infinite series give sufficient numerical accuracy.

With $\rho_{sp}(r)$, $\rho_{sl}(r)$, and $\rho_{pd}(r)$ denoting the apparent resistivities measured with the single-pole, Schlumberger, and polar-dipole arrays respectively (table XI), a first approximation for small spacings compared with the first layer thickness is

$$\rho_{sp}(\tau) \approx \rho(0) \left\{ 1 + \tau \int_0^{\infty} \Phi(\lambda) d\lambda - \frac{\tau^3}{4} \int_0^{\infty} \lambda^2 \Phi(\lambda) d\lambda + \frac{\tau^5}{64} \int_0^{\infty} \lambda^4 \Phi(\lambda) d\lambda - \dots \right\} \quad (42)$$

$$\rho_{sl}(\tau) \approx \rho(0) \left\{ 1 + \frac{\tau^3}{2} \int_0^{\infty} \lambda^2 \Phi(\lambda) d\lambda - \frac{\tau^5}{16} \int_0^{\infty} \lambda^4 \Phi(\lambda) d\lambda + \frac{\tau^7}{384} \int_0^{\infty} \lambda^6 \Phi(\lambda) d\lambda - \dots \right\} \quad (43)$$

$$\rho_{pd}(\tau) \approx \rho(0) \left\{ 1 - \frac{\tau^3}{4} \int_0^{\infty} \lambda^2 \Phi(\lambda) d\lambda + \frac{3\tau^5}{32} \int_0^{\infty} \lambda^4 \Phi(\lambda) d\lambda - \frac{5\tau^7}{768} \int_0^{\infty} \lambda^6 \Phi(\lambda) d\lambda - \dots \right\} \quad (44)$$

Asymptotic expansions of the integral transforms (39) can be derived from expressions given by Tranter (1951, p.67):

$$\int_0^{\infty} \Phi(\lambda) J_0(\lambda\tau) d\lambda \sim \frac{\Phi(0)}{\tau} + \sum_{m=1}^{\infty} (-1)^m \frac{1 \cdot 3 \cdot 5 \cdot \dots \cdot (2m-1)}{2^m m! \tau^{2m+1}} \frac{\partial^{2m}}{\partial \lambda^{2m}} \Phi(0) \quad (45)$$

$$\int_0^{\infty} \lambda \Phi(\lambda) J_1(\lambda\tau) d\lambda \sim \frac{\Phi(0)}{\tau^2} + \sum_{m=1}^{\infty} (-1)^m \frac{1 \cdot 3 \cdot 5 \cdot \dots \cdot (2m+1)}{2^m m! \tau^{2m+2}} \frac{\partial^{2m}}{\partial \lambda^{2m}} \Phi(0) \quad (46)$$

$$\int_0^{\infty} \lambda^2 \Phi(\lambda) J_0(\lambda\tau) d\lambda \sim -\frac{\Phi(0)}{\tau^3} + \sum_{m=2}^{\infty} (-1)^m \frac{1 \cdot 3 \cdot \dots \cdot (2m-1)(2m-1)2m}{2^m m! \tau^{2m+1}} \frac{\partial^{2m-2}}{\partial \lambda^{2m-2}} \Phi(0), \quad (47)$$

If $\lim_{m \rightarrow \infty} \frac{\Phi^{(2m-2)}(0)}{\Phi^{(2m)}(0)} > 1$, then the series (45) to (47) diverge for all values of r . However, the value of the integrals can be calculated with great accuracy for large r , by using only the decreasing part of the series, stopping at the proper term. Under these circumstances the error is smaller than the first neglected term, (Lanczos, 1956, p. 483).

If r is sufficiently large so that the first few terms in series (45) to (47) decrease in absolute value, the approximation to the apparent resistivities using four terms of the asymptotic expansion becomes,

$$\rho_{SP}(\tau) \approx \rho(\infty) + \rho(0) \left\{ -\frac{1}{2\tau^2} \bar{\Phi}^{(2)}(0) + \frac{3}{8\tau^4} \bar{\Phi}^{(4)}(0) - \frac{5}{16\tau^6} \bar{\Phi}^{(6)}(0) + \dots \right\} \quad (48)$$

$$\rho_{SL}(\tau) \approx \rho(\infty) + \rho(0) \left\{ -\frac{3}{2\tau^2} \bar{\Phi}^{(2)}(0) + \frac{15}{8\tau^4} \bar{\Phi}^{(4)}(0) - \frac{35}{16\tau^6} \bar{\Phi}^{(6)}(0) + \dots \right\} \quad (49)$$

$$\rho_{PD}(\tau) \approx \rho(\infty) + \rho(0) \left\{ -\frac{3}{\tau^2} \bar{\Phi}^{(2)}(0) + \frac{45}{8\tau^4} \bar{\Phi}^{(4)}(0) - \frac{70}{8\tau^6} \bar{\Phi}^{(6)}(0) + \dots \right\} \quad (50)$$

Evaluation of the Basic Hankel Transforms by Series Expansion

The following paragraph, a synthesis of ideas developed by Baranov and Kunetz (1958), and Bodvarsson (1966), is presented because it gives considerable insight into the physical nature of the problem and has a direct connection to other branches of geophysics.

Consider $K(\lambda)$ as unilateral Laplace transform of a certain function $q(z)$, i.e.

$$K(\lambda) = \int_0^{\infty} q(z) e^{-\lambda z} dz \quad (51)$$

If this integral is substituted into (10i),

$$U(r) = \frac{1}{2\pi} \int_0^{\infty} \int_0^{\infty} q(z) e^{-\lambda z} J_0(\lambda r) dz d\lambda$$

Interchange of the order of integration and application of the Lipschitz integral (Erdelyi, 1954, v. 2, p. 9) yields

$$U(r) = \frac{1}{2\pi} \int_0^{\infty} \frac{q(z)}{\sqrt{r^2 + z^2}} dz \quad (52)$$

Hence, $q(z)$ is Green's function for the general boundary-value problem stated at the beginning of this thesis. It can also be thought of as a certain density distribution along the vertical axis (see figure 1), producing the potential $U(r)$. From still another point of view, $q(z)$ may be considered as the impulse response of a linear system characterized by a system function $K(\lambda)$ defined by (10ii).

In certain cases $q(z)$ can be computed independently from the inversion of (51) and is such that it simplifies expression (52) as illustrated next for the two-layer model. Its kernel function is according to table III

$$K(\lambda) = \frac{1 - k e^{-2\lambda h}}{1 + k e^{-2\lambda h}}$$

where,

$$k \triangleq \frac{h_2 - h_1}{h_1 + h_2} \frac{\rho_1 - \rho_2}{\rho_1 + \rho_2}$$

is the reflection coefficient, ρ_1 and ρ_2 are the first and second layer resistivities respectively, and h is the thickness of the first layer.

Since, $|ke^{-2\lambda h}| < 1$, $\lambda \geq 0$, except for $\rho_2 = 0$, or ∞ , the kernel function can be written

$$K(\lambda) = 1 + 2 \sum_{n=1}^{\infty} (-k)^n e^{-2n\lambda h} \quad (53)$$

The inverse Laplace transformation of (53) yields

$$q(z) = \delta(z) + 2 \sum_{n=1}^{\infty} (-k)^n \delta(z - 2nh) \quad (54)$$

Thus, $q(z)$ consists of an infinite train of impulses along the vertical axis through the current electrode. Consequently, it can be computed directly from the laws of geometrical optics, or in the same way as a synthetic impulse seismogram with all the multiple reflections in it. If (54) is substituted into (52), the electrical potential around the current electrode can be evaluated by summation of an infinite series,

$$U(r) = \frac{IP(o)}{2\pi} \left\{ \frac{1}{r} + 2 \sum_{n=1}^{\infty} \frac{(-k)^n}{\sqrt{r^2 + 2nh^2}} \right\} \quad (54)$$

This is the familiar result obtained by Hummel (1929), applying the theory of Kelvin's images.

Generalization to a multilayered model is possible if the thicknesses of the beds in the section have integer values. Under this condition $q(z)$ is computed either as a synthetic impulse seismogram (Baranov and Kunetz, 1958), or by expanding Flathe's kernel function into an infinite series of exponential terms (Mooney and others, 1966). The advantage of the method is the simplicity of the computations if the series converge fast. The disadvantage is that the method is not general enough to be applicable to any kernel function or to the inversion of field data.

Evaluation of the Basic Hankel Transforms by Numerical Quadrature

1. Polynomial approximation of the kernel function.--

The method consists in replacing sections of the kernel function by an approximating polynomial in order to simplify the integral. Quadratic approximation was used by Mooney and Wetzel (1957), and Galbraith and others (1964). The algorithm for the general n th order approximation is developed next.

For numerical computations with a fixed number of digits, as for instance when working in single precision on the CDC 8090 computer (eight digits), the upper limit of the integrals (39) becomes finite, because $\phi(\lambda)$ becomes smaller than the smallest number in the range of the machine for some large,

but finite λ . The numerical value of this upper limit λ_c for the horizontal layer case is found from (25),

$$K(\lambda) = \frac{1 - k(\lambda)e^{-2\lambda d_1}}{1 + k(\lambda)e^{-2\lambda d_1}}, \quad |k(\lambda)| < 1$$

by observing that with an accuracy of eight digits $K(\lambda) = 1$, whenever $|k(\lambda)e^{-2\lambda d_1}| < 10^{-8}$. An upper bound λ_c for λ such that this relation holds is found by setting $|k(\lambda)| = 1$, then $e^{-2\lambda_c d_1} < 10^{-8}$, and $\lambda_c > \frac{8 \log_{10} 10}{2d_1}$; hence, $\lambda_c = \frac{10}{d_1}$ is an appropriate upper bound for the variable of integration, and equation (39) can be rewritten

$$H_k(\tau) \approx \int_0^{\lambda_c} \Phi(\lambda) \lambda^u J_\nu(\lambda\tau) d\lambda. \quad (56)$$

Next the range of integration $0 \leq \lambda \leq \lambda_c$ is divided into m subintervals, or panels such as $\lambda_i \leq \lambda \leq \lambda_{i+1}$, $i = 1, 2, 3, \dots, m$ in figure 15, so that (56) is replaced by

$$H_k(\tau) \approx \sum_{i=1}^m \int_{\lambda_i}^{\lambda_{i+1}} \Phi(\lambda) \lambda^u J_\nu(\lambda\tau) d\lambda. \quad (57)$$

On each interval $(\lambda_i, \lambda_{i+1})$ the modified kernel curve is approximated by a polynomial of degree n passing through exactly $n+1$ points of $\Phi(\lambda)$, i.e.

$$\bar{\Phi}(\lambda) \approx \sum_{j=0}^n a_j \lambda^j, \quad (58)$$

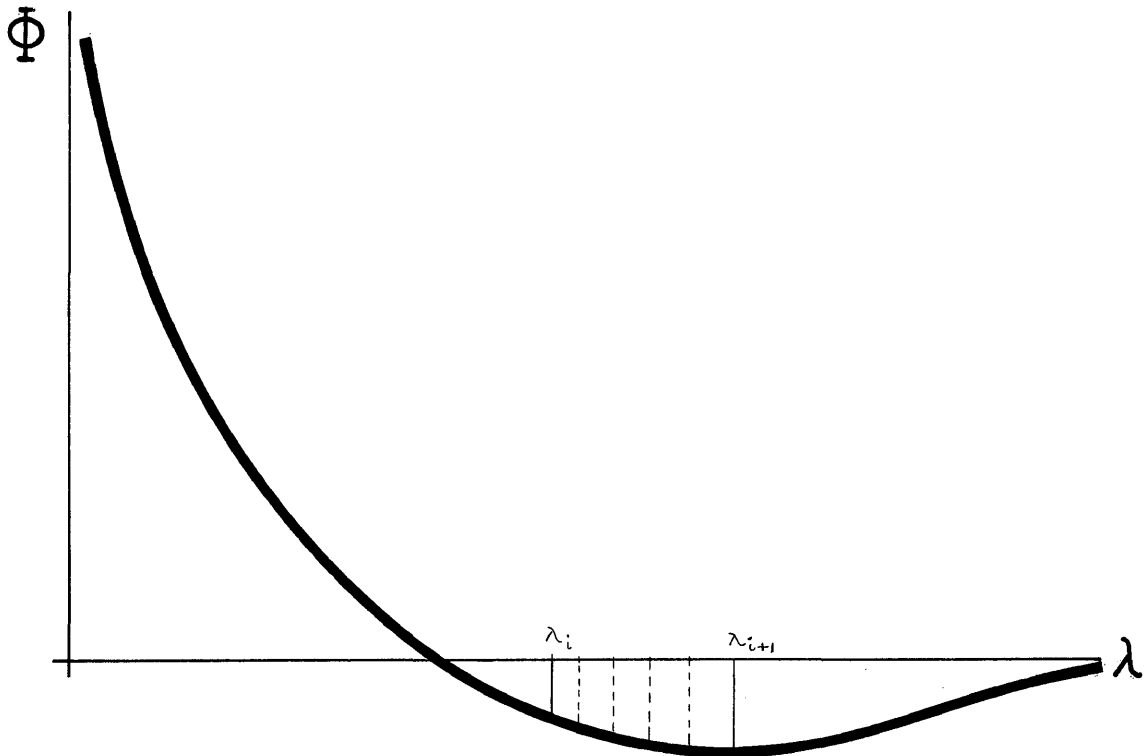


Figure 15.

Approximation of the kernel

The following quadrature formula is obtained by combining (57) and (58), and making the change of variable $\lambda r = x$:

$$H_k(\tau) \approx \frac{1}{\tau^{\mu+1}} \sum_{i=1}^m \sum_{j=0}^n \frac{a_j}{\tau^j} \int_{\lambda_i \tau}^{\lambda_{i+1} \tau} x^{\mu+j} J_\nu(x) dx. \quad (59)$$

The evaluation of the definite integrals in this approximation can be carried out by using either power-series expansions or reductions formulas.

a). Power-series expansions:

Taylor series (Luke, 1962, p. 44),

$$\int_0^z t^\mu J_\nu(t) dt = z^{\mu+1} \sum_{k=0}^{\infty} \frac{(-1)^k \left(\frac{z}{2}\right)^{\nu+2k}}{k! (\mu + \nu + 2k + 1) \Gamma(\nu + k + 1)} . \quad (60)$$

Asymptotic expansion (Luke, 1962, p. 54),

$$\int_0^z t^\mu J_\nu(t) dt = \frac{z^\mu \Gamma\left(\frac{\nu + \mu + 1}{2}\right)}{\Gamma\left(\frac{\nu - \mu + 1}{2}\right)} - \left(\frac{z}{\pi z}\right)^{\frac{1}{2}} (f \cos \theta + g \sin \theta) , \quad (61)$$

where

$$\theta = z - \frac{\nu \pi}{2} + \frac{\pi}{4}$$

and

$$f \sim \sum_{k=0}^{\infty} (-1)^k a_{2k} z^{-2k} , \quad g \sim \sum_{k=0}^{\infty} (-1)^k a_{2k+1} z^{-2k-1} . \quad (62)$$

The a_k are given by the following recurrence formula:

The a_k are given by the following recurrence formula:

$$2(k+1)a_{k+1} = \left[3\left(k + \frac{1}{2}\right)\left(k + \frac{5}{6}\right) - 2\mu(k+1) - \nu^2 \right] a_k - \left(k + \frac{1}{2} + \nu\right)\left(k + \frac{1}{2} - \nu\right)\left(k - \frac{1}{2} - \mu\right) a_{k-1} , \quad (63)$$

with

$$a_0 = 1 , \quad a_1 = \frac{5}{8} - \mu - \frac{\nu^2}{2} .$$

A computer program based on equations (60) to (63) was written to test the feasibility of this procedure. To accomplish an overall accuracy of six digits, a large number of

terms in series (60) had to be added. Because the corresponding increase in computing time makes the method very inefficient for small-scale computers, it was abandoned.

b). Reduction formulas: The following two reductions formulas obtained from expressions given by Abramowitz and Stegun (1965, p. 483) are useful:

$$\begin{aligned} \frac{1}{\tau^{\mu+j+1}} \int_{\lambda_i \tau}^{\lambda_{i+1} \tau} t^{\mu+j} J_0(t) dt &= \frac{1}{\tau} \left\{ \left[\lambda^{\mu+j} J_1(\lambda \tau) \right. \right. \\ &+ \left. \lambda^{\mu+j-1} \frac{\mu+j-1}{\tau} J_0(\lambda \tau) \right] \Big|_{\lambda_i}^{\lambda_{i+1}} \\ &\left. - \frac{(\mu+j-1)^2}{\tau^{\mu+j}} \int_{\lambda_i \tau}^{\lambda_{i+1} \tau} t^{\mu+j-2} J_0(t) dt \right\} \quad (64) \end{aligned}$$

$$\begin{aligned} \frac{1}{\tau^{\mu+j+1}} \int_{\lambda_i \tau}^{\lambda_{i+1} \tau} t^{\mu+j} J_1(t) dt &= \frac{\mu+j}{\tau^{\mu+j+1}} \int_{\lambda_i \tau}^{\lambda_{i+1} \tau} t^{\mu+j-1} J_0(t) dt \\ &- \frac{\lambda^{\mu+j}}{\tau} J_0(\lambda \tau) \Big|_{\lambda_i}^{\lambda_{i+1}} \quad (65) \end{aligned}$$

Computer programs were written to evaluate the functions $J_0(x)$, $J_1(x)$, and $\int_0^x J_0(t)dt$ by polynomial approximation (Abramowitz and Stegun, 1965, Hitchcock, 1957). Expressions (64) and (65) give satisfactory numerical results if the factors multiplying the integrals in (59) are smaller than 1. This is the case when $r^j > a_j$, where the a_j are the coefficients of the polynomial approximation to $\phi(\lambda)$ as given by (58). The constants a_j were computed by the method of divided differences.

The coefficients for the polynomial approximation of the kernel functions representing the Adena field are very large, as illustrated by the equivalent layer case (6-2) for the Hough no.1 well log. The approximating polynomial of order five on the interval $1.29 \times 10^{-6} \leq \lambda \leq 2.89 \times 10^{-6}$ is

$$P(\lambda) = 58.6 - 2.13 \times 10^7 \lambda + 6.55 \times 10^{12} \lambda^2 - 1.49 \times 10^{18} \lambda^3 \\ + 2.10 \times 10^{23} \lambda^4 - 1.34 \times 10^{28} \lambda^5 .$$

The large magnitude of these coefficients, together with their alternating signs, makes any computations by (59) meaningless, unless r is taken large enough to compensate the a_j . A comparison of the Hough no.1, (6-2) case computed by Gaussian quadrature (correct to five digits) and by the above method points this out clearly (table XII). Because of these severe limitations and its slowness (2.5 min of computing time per layer for one transform value on the CDC 8090), this approach was discarded for the numerical evaluation of (39).

Table XII.

Comparison of the Hankel transforms $H_1(r)$
computed in two different ways

r	Gauss quadrature	Poly. approx.
10^3	-0.0210727	-1.2241106
10^4	4.9679009	4.809944
10^5	25.395790	25.395470
10^6	54.009592	54.009884

2. Polynomial approximation of the integrand.-- In numerical quadrature formulas, the integral is approximated by a finite sum of weighted ordinates of the function. The weights are obtained from the polynomial which matches the function exactly at certain sample points. There are two types of quadrature formulas, Newton-Cotes formulas where the samples are equally spaced, and Gaussian formulas where the samples are determined by the zeros of Legendre polynomials $P_n(x)$. The latter has the advantage of requiring only half the number of ordinates for a given order of the approximating polynomial. In other words, with n sample points the degree of the polynomial approximation of the integrand is $n-1$ for Newton-Cotes, and $2n-1$ for Gauss. In addition, the interpolation by Legendre polynomials in Gauss' method converges

more rapidly than the interpolation by Lagrangian polynomials in Newton-Cotes' formula (Lanczos, 1957, p. 403). Furthermore, the saving of ordinates does not only economize computing time, it also reduces the round-off error in the arithmetic operations. Because of the advantages it was decided to use Gaussian quadrature rather than Newton-Cotes formulas for the numerical evaluation of synthetic sounding curves.

Gauss' rule of order n for an arbitrary interval (a,b) is

$$\int_a^b f(y) dy = \frac{b-a}{2} \sum_{i=1}^n w_i f(y_i) + R_n \quad , \quad (66)$$

(Abramowitz and Stegun, 1965, p. 887)

with

$$y_i = \frac{b-a}{2} x_i + \frac{b+a}{2} \quad (67)$$

and the remainder

$$R_n = \frac{(b-a)^{2n+1} (n!)^4}{(2n+1) [(2n)!]^3} \frac{1}{2^{2n+1}} f^{(2n)}(\xi) \quad , \quad a \leq \xi \leq b. \quad (68)$$

The abscissas x_i and weights w_i given by

$$P_n(x_i) = 0 \quad , \quad w_i = \frac{2}{(1-x_i)^2 [P_n'(x_i)]^2} \quad i = 1, 2, \dots, n, \quad (69)$$

have been tabulated for selected values of n up to 96, (Abramowitz and Stegun, 1965, p. 916).

With $x = \lambda r$ the general expressions for the basic Hankel transforms (39) can be rewritten

$$H_k(r) = \frac{1}{r} \int_0^{\infty} \left(\frac{x}{r}\right)^{\mu} \Phi\left(\frac{x}{r}\right) J_{\nu}(x) dx \quad (70)$$

$k = 1, 2, 3; \mu = 0, 1, 2; \nu = 0, 1.$

The effect of the transform variable is to scale the kernel $\left(\frac{x}{r}\right)^{\mu} \Phi\left(\frac{x}{r}\right)$ with respect to the Bessel function $J_{\nu}(x)$. For small r the kernel function appears very compressed, but stretches out as r increases, as shown in figure 16 for the case $k = 1$ in formula (70).

When $x_c = \lambda_c r$ is reasonably small, laying in the first few cycles of the Bessel functions, formula (66) can be applied directly with $a = 0$ and $b = x_c$. For large x_c , exceeding several cycles of $J_{\nu}(x)$ this process becomes too slow, even for a large-scale computer. The following example illustrates this point. The thickness of the first layer d_1 of the Hough no.1 section is 33.5 m; for a relatively small spacing $r = 1000$ m,

$$x_c = \frac{10r}{d_1} = \frac{10000}{33.5} \approx 300,$$

which corresponds to about 50 cycles of $J_{\nu}(x)$, to be taken into account in the integration.

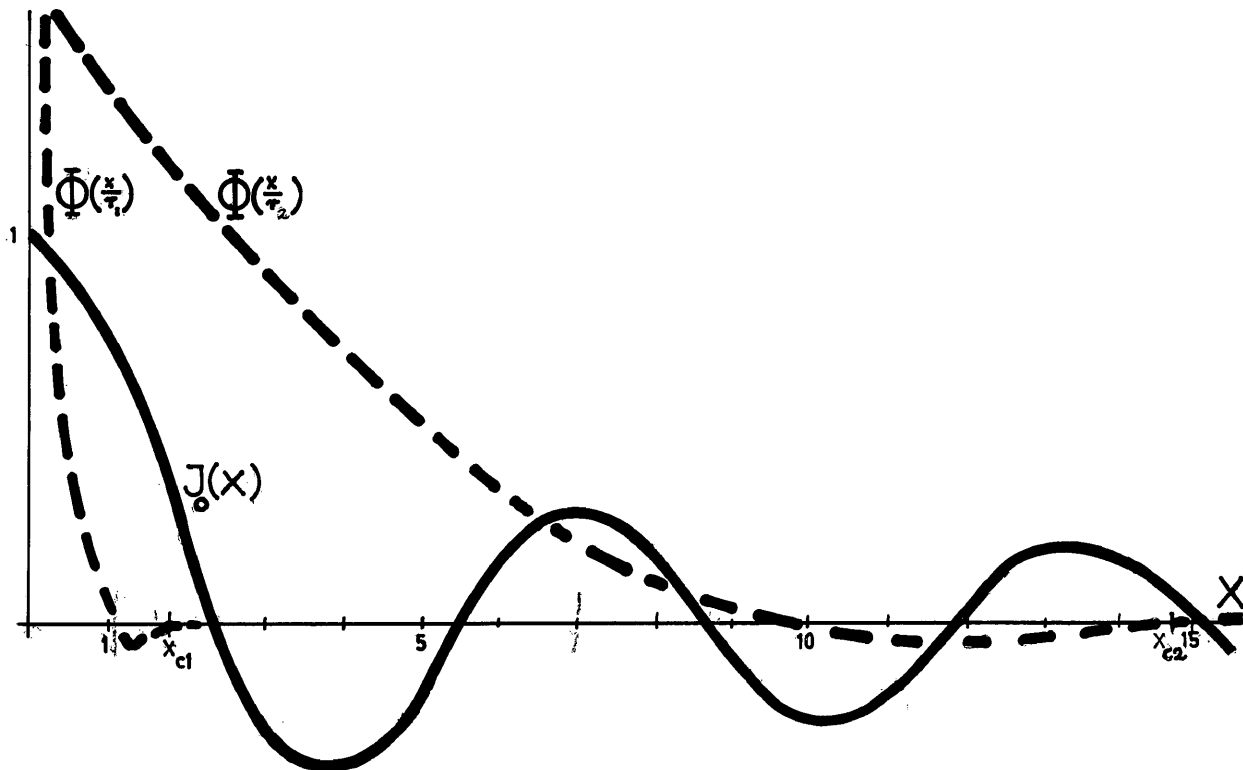


Figure 16.

Effect of the transform variable r on
the product $\phi(\lambda)J_0(x)$

Longmann (1957)₂ has given a method to overcome this difficulty for "well behaved" functions $\phi(\lambda)$, as the ones dealt with here, presenting an exponential tail. His procedure consists in applying formula (66) successively to half a cycle of the Bessel functions; a and b are consecutive zeros of $J_\nu(x)$. By this procedure, it is observed that beyond a certain value of the abscissa x the integration yields an alternating, slowly convergent series. The sum of this series can be speeded up by applying an Euler transformation (Bromwich, 1931, p. 62) to a few terms of it.

This procedure may be adapted to the evaluation of Hankel transforms by writing (70) as

$$H_k(\tau) \approx \frac{1}{\tau^{\mu+1}} \sum_{j=0}^m \int_{z_j}^{z_{j+1}} x^{\mu} \Phi\left(\frac{x}{\tau}\right) J_\nu(x) dx \quad , \quad (71)$$

where m is a finite integer selected according to the required accuracy, and z_j is given by

$$J_\nu(z_j) = 0 \quad , \quad \nu = 0, 1 \quad ; \quad j = 0, 1, 2, \dots, m. \quad (72)$$

When the definite integrals in (71) are approximated by Gauss' rule of order n , the following finite series is obtained:

$$H_k(\tau) \approx \frac{1}{\tau^{\mu+1}} \sum_{j=0}^m \frac{z_{j+1} - z_j}{2} \sum_{i=1}^n w_i y_{ij}^{\mu} \Phi\left(\frac{y_{ij}}{\tau}\right) J_\nu(y_{ij}) \quad (73)$$

$$H_k(\tau) \approx \frac{1}{\tau^{\mu+1}} \sum_{j=0}^m u_j \quad (74)$$

The y_{ij} in (73) are given by (67) with $a = z_j$, $b = z_{j+1}$. If the terms u_j in series (74) are slowly decreasing in magnitude and alternating in sign starting with $j = p$, (74) can be rewritten

$$H_k(\tau) \approx \frac{1}{\tau^{\mu+1}} \left\{ \sum_{j=0}^{p-1} u_j + \sum_{j=p}^m (-1)^j |u_j| \right\} \quad (75)$$

The sum of the second series in (75) can be obtained with improved accuracy by "eulerizing" it

$$\sum_{j=p}^m (-1)^j u_j = \frac{1}{2} u_p + \frac{1}{4} \Delta u_p + \dots + \frac{1}{2^q} \Delta^{q-1} u_p + R_q \quad (76)$$

$q \leq m-p,$

where $\Delta^j u_p$ denotes the j th leading difference of u_p in the set $\{u_j\}$. The remainder is given by

$$R_q \triangleq \frac{1}{2^q} \left[\Delta^q u_p - \Delta^q u_{p+1} + \Delta^q u_{p+2} - \dots \right]. \quad (77)$$

Longman (1957) gives the abscissas y_{ij} for Gauss' rule of order 16 and the corresponding values of $J_0(y_{ij})$ and $J_1(y_{ij})$ for the first ten cycles. For the transformation of the Adena oil field kernels it was necessary to extend these coefficients to at least 50 cycles.

The first step in evaluating the abscissas y_{ij} from

$$y_{ij} = \frac{z_{j+1} - z_j}{2} x_i + \frac{z_{j+1} + z_j}{2}, \quad (78)$$

$$i = 1, 2, \dots, 16; \quad j = 20, 21, \dots, 99$$

consists in finding the zeros z_j of $J_0(x)$ and $J_1(x)$. For this purpose the following approximations given by Jahnke and Emde (1945, p. 143), were used:

$$J_0(z_j) = 0 \text{ for}$$

$$\frac{z_j}{\pi} \approx j - \frac{1}{4} + \frac{0.050661}{4j-1} - \frac{0.053041}{(4j-1)^3} + \frac{0.262051}{(4j-1)^5} - \dots;$$

(79)

$$J_1(z_j) = 0 \text{ for}$$

$$\frac{z_j}{\pi} \approx \left[j + \frac{.11}{4} - \frac{0.151982}{4j+1} + \frac{0.015399}{(4j-1)^3} - \frac{.245270}{(4j+1)^5} + \dots \right] \quad \text{J.P.}$$

These formulas give the values of z_{20} with an accuracy of eight digits. The higher order zeros are even better approximated because of the asymptotic behavior of the expressions.

Next, the y_{ij} are obtained from (78) and the tabulated values of x_i for $n = 16$ (Abramowitz and Stegun, 1965, p.916). $J_0(y_{ij})$ and $J_1(y_{ij})$ are computed from the asymptotic expansion (Luke, 1962, p. 31):

$$J_\nu(z) = \left(\frac{z}{\pi} \right)^{1/2} \left[\cos \left(z - \frac{1}{2} \nu \pi - \frac{1}{4} \pi \right) P(\nu, z) + \sin \left(z - \frac{1}{2} \nu \pi - \frac{1}{4} \pi \right) Q(\nu, z) \right] \quad (80)$$

with $|z| \rightarrow \infty \quad |\arg(z)| < \pi$,

$$P(\nu, z) \sim \sum_{k=0}^{\infty} \frac{(-1)^k \left(\frac{1}{2} + \nu\right)_{2k} \left(\frac{1}{2} - \nu\right)_{2k}}{(2k)! (2z)^{2k}} \quad (81)$$

$$\triangleq \sum_{i=0}^{\infty} U_i$$

$$Q(\nu, z) \sim \sum_{k=0}^{\infty} \frac{(-1)^k \left(\frac{1}{2} + \nu\right)_{2k+1} \left(\frac{1}{2} - \nu\right)_{2k+1}}{(2k+1)! (2z)^{2k+1}} \quad (82)$$

$$\triangleq \sum_{i=0}^{\infty} T_i$$

where $(a)_0 \triangleq 1$, and $(a)_k \triangleq a(a+1)(a+2) \dots (a+k-1)$. The terms U_i , T_i in series (81) and (82) may be computed by the following iteration scheme:

$$U_k = -U_{k-1} \frac{(\frac{1}{2} + \nu + 2k - 2)(\frac{1}{2} + \nu + 2k - 1)(\frac{1}{2} - \nu + 2k - 2)(\frac{1}{2} - \nu + 2k - 1)}{2k(2k-1)(2z)^2} \quad (83)$$

$$U_0 = 1$$

$$T_k = -T_{k-1} \frac{(\frac{1}{2} + \nu + 2k - 1)(\frac{1}{2} + \nu + 2k)(\frac{1}{2} - \nu + 2k - 1)(\frac{1}{2} - \nu + 2k)}{2k(2k+1)(2z)^2} \quad (84)$$

$$T_0 = \frac{(\frac{1}{2} + \nu)(\frac{1}{2} - \nu)}{2z}$$

The computations were carried out in double precision (16 digits) on the IBM 7044 at the University of Colorado Graduate School Computing Center. With only five terms of each series $P(\nu, z)$ and $Q(\nu, z)$, the Bessel functions of arguments greater than 60 are correct to 12 decimal places, as checked with the tables from the Harvard Computation Laboratory (1947).

Formula (73) is further simplified by lumping the different constants together into one weight

$$W_{ij} \triangleq \frac{z_{j+1} - z_j}{2} w_i y_{ij}^\mu, \quad (85)$$

so that the final expression for quadrature becomes

$$r = \int_{\nu} (y_{ij})$$

$$H_k(\tau) \approx \frac{1}{\tau^{\mu+1}} \sum_{j=0}^m \sum_{i=1}^{16} W_{ij} \left(\frac{y_{ij}}{\tau} \right), \quad m \leq 50. \quad (86)$$

Transform programs were written both in Fortran for the CDC 8090, and in Fortran IV for the IBM 7044. Because of large storage requirements (10000 locations for constants), the program for the CDC 8090 had to be broken up into three parts. Magnetic tape operations are required heavily which brings the average computing time per layer for one transform value to 25 sec. The average computing time per layer for one transform value is approximately 0.3 sec on the IBM 7044. The flow chart for these computer programs is given in the appendix.

There are three sources of errors in the procedure used:

a). The error of the Gaussian quadrature. The traditional error estimate is given by (68). This formula is of no practical help because the knowledge of the derivative of order $2n$ of $f(x)$ throughout the interval of integration is required. It shows, however, that the quadrature formula (66) is exact if $f(x)$ is precisely a polynomial of degree $2n-1$ between the limits of integration. From this property the following qualitative statements on the numerical accuracy can be made:

The error for spacings r smaller than the first layer thickness will depend on how well the integrand can be approximated by a polynomial of degree 95 on the maximum interval $(0,10)$.

For larger spacings, up to $r = 30 \times (\text{first layer-thickness})$, the error is determined by the accuracy with which a polynomial of degree 31 approximates the integrand between consecutive zeros of the Bessel functions (approximately $\pi/2$).

b). The error in the Euler transformation. The remainder R_q defined by (77) can be used for estimating the error in the summation formula (76) if the leading differences $\Delta^q u_n$, $n = q, q+1, \dots$, are always positive and decrease as n increases, because then

$$|R_q| < \frac{1}{2^q} |\Delta^q u_p| .$$

However, the conditions stated by Bromwich (1931, p. 62), for this inequality do not hold for the present case. Therefore, the following accuracy test is used: the transformation is applied successively to an increasing number of terms; if the relative error between two consecutive sums s_j and s_{j+1} is smaller than a prescribed positive constant, the result s_{j+1} is accepted as satisfactory.

c). The round-off error. This error arises from the limitation of using only a finite number of decimal places in the computations. A theoretical discussion of its effects is rather unsatisfactory for lengthy programs; perhaps the best way of estimating it is to use the computer itself for an indication of its magnitude. For this objective the transforms of $\phi(\lambda) = 1000\lambda e^{-1000\lambda}$ were evaluated both in closed form

and by the quadrature program in order to compare the numerical values. The following formulas were employed for the exact Hankel transformations:

$$\int_0^{\infty} \lambda^k e^{-a\lambda} J_0(\lambda r) d\lambda = \frac{k!}{[a^2 + r^2]^{1/2 k + 1/2}} P_k \left(\frac{a}{[a^2 + r^2]^{1/2}} \right)$$

(Erdélyi, 1954, v. 2, p. 9)

$$\int_0^{\infty} \lambda^{k+1} e^{-a\lambda} J_k(\lambda r) d\lambda = \frac{1}{\sqrt{\pi}} 2^{k+1} \frac{\Gamma(k + \frac{3}{2})}{[a^2 + r^2]^{k+3/2}} a r^k .$$

(Erdélyi, 1954, v. 2, p. 29).

The errors between closed and approximated transforms (39) in terms of the error criteria given on page 59 are shown in table XIII.

Table XIII.

Errors between exact and approximated transforms

Transform	Max. ampl. of error curve	Maximum absolute error	Maximum relative error	Root mean square deviation
$rH_1(r)$	7×10^{-8}	-7×10^{-8}	-9×10^{-5}	3×10^{-8}
$r^2 H_2(r)$	1×10^{-7}	-1×10^{-7}	-6×10^{-4}	5×10^{-8}
$r^3 H_3(r)$	2×10^{-5}	-3×10^{-5}	-3×10^{-3}	3×10^{-6}

Table XIII shows that for this particular

transformation round-off and quadrature errors are not severe and that five digits accuracy can be obtained in case of good convergence of the integrals.

It is most important to notice that if these integrals converge slowly, for instance if the geoelectric section has a very resistant basement, the alternating series (76) might have to be truncated too soon, thus diminishing the accuracy of the corresponding apparent resistivities for large spacings of r . But under these circumstances the apparent resistivity curves approach a straight line with a slope of plus 1 (Keller and Frischknecht, 1966, p. 116), for large spacings of r .

Synthetic Sounding Curves for the Adena Field

The single-pole, Schlumberger, and polar-dipole apparent resistivities were computed for the Hough no.1 (6-2), (11-3), (25-1), and 40 layer cases of the Adena field. Six functional values were tabulated per decade of the spacing r between 1 m and 1000 km in the first example, and between 1 m and 31 km in the rest. It was impossible to compute synthetic sounding curves for the well log sampled with a ten-foot interval because of the length of computing time involved: for one profile of 30 points, 120 hours, (5 days) on the CDC 8090, and 1.5 hours on the IBM 7044.

The Hough no.1, (6-2) sounding curves were checked with the asymptotic expansion formulas (48) to (50) for the spacing $r = 10^7$ m. Table XIV compares the apparent resistivities computed by the asymptotic expansion with the corresponding values obtained by the Hankel transform program on the IBM 7044.

Table XIV.

Comparison of apparent resistivities computed by asymptotic expansion and by quadrature

Array	Asymptotic expansion ap. res. (Ωm)	Quadrature ap. res. (Ωm)
Single pole	599.147	599.15
Schlumberger	597.463	597.47
Polar dipole	595.865	594.99

The agreement between the respective single-pole and Schlumberger apparent resistivities is essentially correct to five places. The polar-dipole apparent resistivities show a difference which could be expected, because the series (76) did not converge for the specified error bound (10^{-7}), as in the former cases.

Figure 17 shows the three sounding curves for Hough no.1, (6-2) plotted one on top of the other. The minimum in

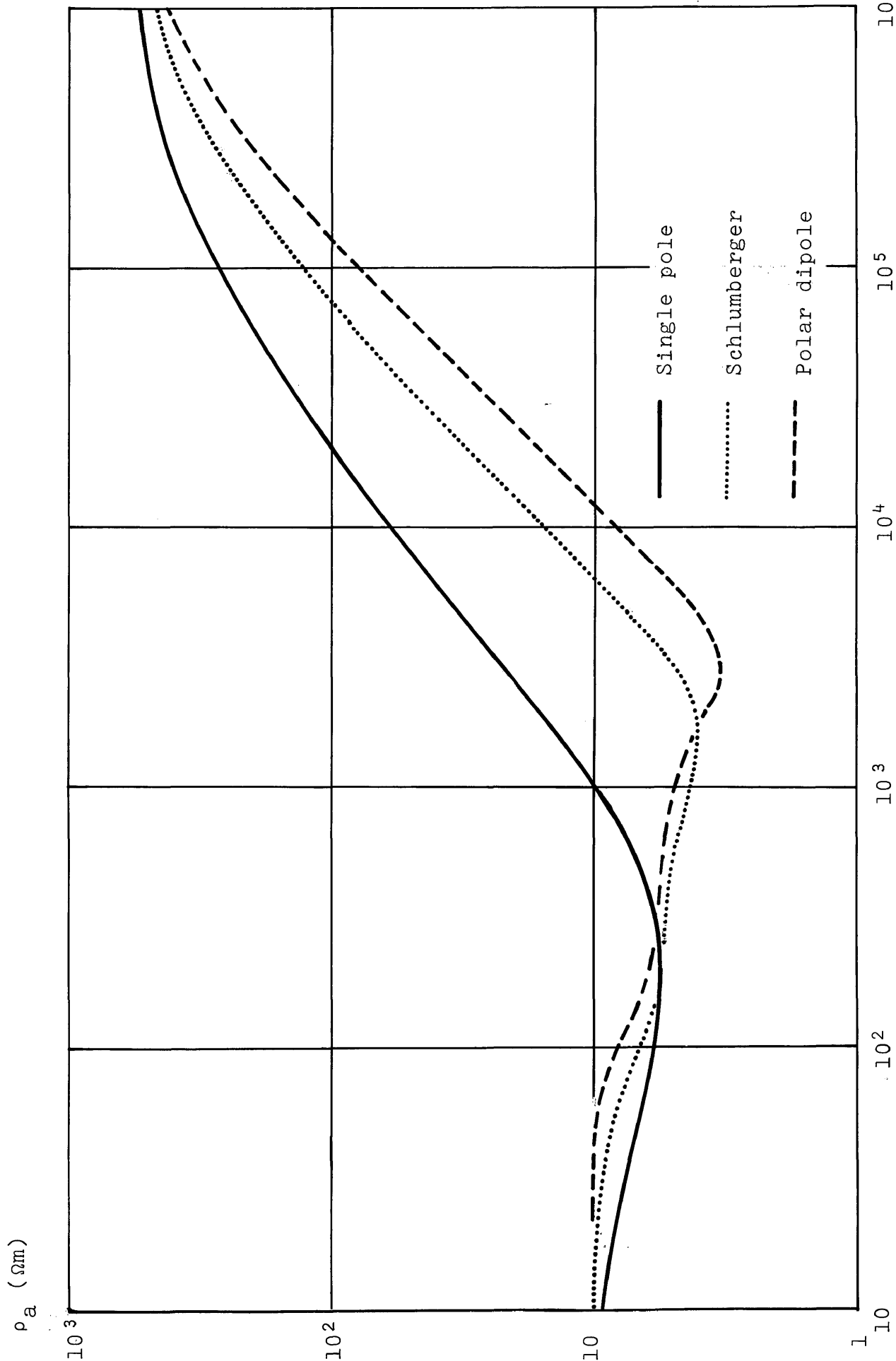


Figure 17.

Synthetic sounding curves for Hough no.1, Adena, model (6-2)

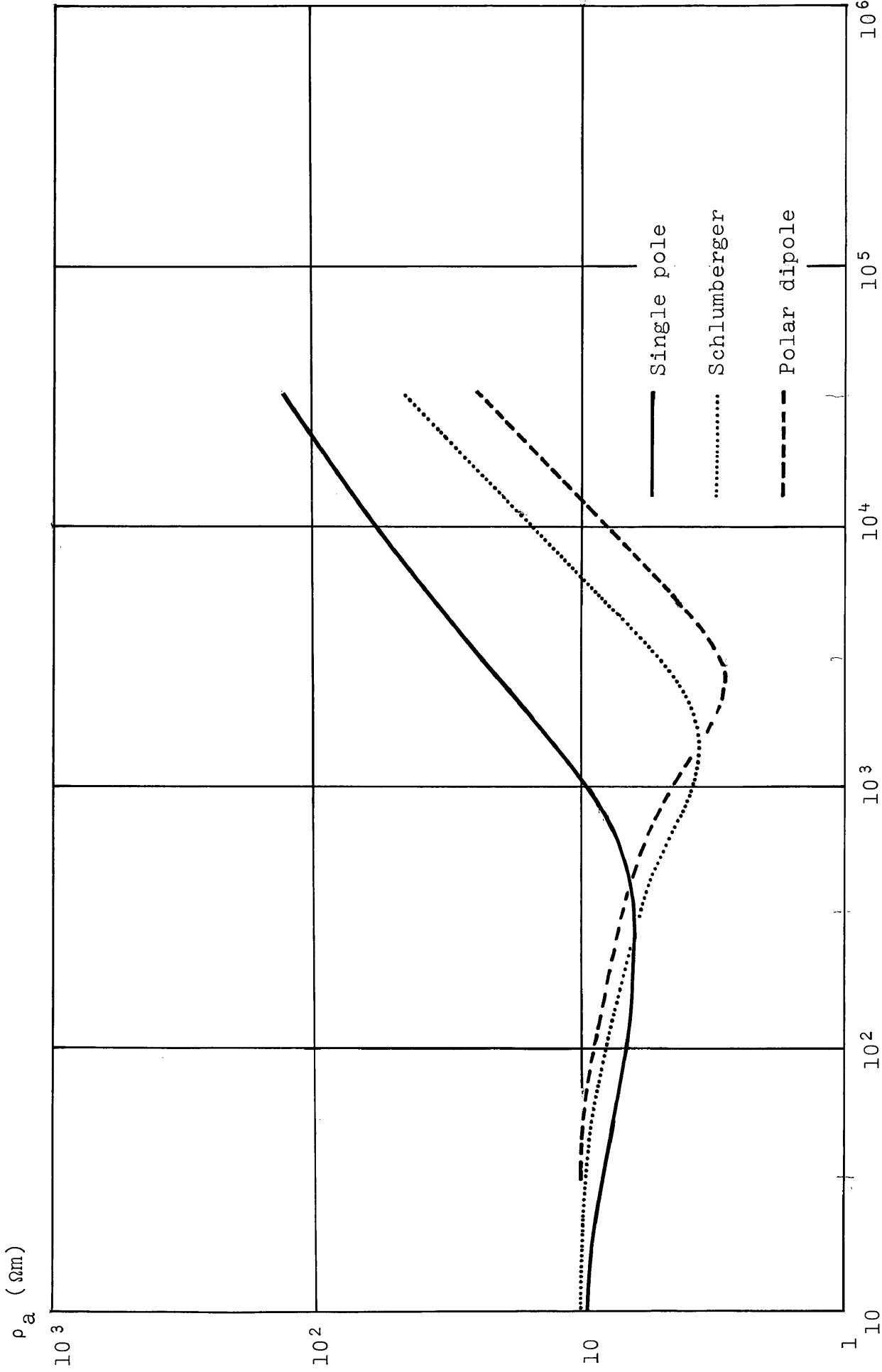


Figure 18.

Synthetic sounding curves for Hough no.1, Adena, model (40)

the apparent resistivities produced by the conductive Pierre shale is more emphasized and has more character in the Schlumberger and polar-dipole arrays than in the single-pole array. The sounding curves are shifted, one with respect to the other, the single-pole curve approaching the final asymptotic value faster. Comparison with the Hough no.1, 40-layer case plotted in figure 18 shows that the biggest differences between corresponding sounding curves occur in their lower parts, for spacings smaller than 300 m. This observation is in agreement with the observation made for the kernel functions, that the upper layers have considerably more weight in fitting the correct model.

A quantitative comparison study of single-pole apparent resistivity curves for several equivalent models of Hough no.1, Adena, showed that relative departures between them are of the same magnitude as the relative departures between the corresponding kernel curves. This behavior suggests that the quantitative effects of the layering parameters could be studied in the λ -domain, which is of course, an advantage, because kernel functions are considerably easier to generate than sounding curves.

The relative departures between Schlumberger and polar-dipole apparent resistivities for different equivalent models of the Adena field increase slightly. For instance,

comparison of equivalent model (6-2) with equivalent model (40) gives the following relative departures: single-pole 13.7 percent, Schlumberger 18.8 percent, polar-dipole 21.4 percent. These anomalies indicate that Schlumberger and polar-dipole measurements have, at least theoretically, higher resolving power than the single-pole measurements, which is, however, lost when transformed into the kernel domain.

As stated before on page 64 in order to detect the resistant target layers representing the "D" and "J" sands of the Adena oil field an accuracy in measurements much better than 1 percent is required. This hypothetical anomaly increases slightly for the Schlumberger and polar-dipole arrays, at the same time requiring greater spacings (approximately 2.5 and 4 miles, respectively).

THE INTERPRETATION OF RESISTIVITY
DATA VIA KERNEL FUNCTION

Two steps are involved in the transformation of a given resistivity variation along the vertical axis of a semi infinite medium to the corresponding distribution of the potential of the electric field on its surface. The first step, discussed in the first two chapters, consists of the non-linear process of evaluating the kernel function for the medium. The second step, presented in the chapter preceding this one, is a linear integral transformation (Hankel, or Fourier-Bessel transform) of the kernel function into an apparent-resistivity function. It is tempting to reverse these two steps in order to obtain the vertical resistivity profile of the medium from observed resistivity sounding curves. This approach was first suggested by Slichter (1933), and later taken on by Pekeris (1940), Vozoff (1958), and Koefoed (1965a, and 1965b).

This interpretational procedure starts then by first applying an inverse Hankel transformation to the field data. The inversion formulas, developed in the next paragraphs, depend on the particular type of array used for measuring apparent resistivities.

Formulas for the Inversion of Apparent Resistivities

1. Single-pole array.-- The apparent resistivity measured with the single-pole array $\rho_{sp}(r)$, in terms of the kernel function $K(\lambda) = \phi(\lambda) + 1$ is according to table XI

$$\rho_{sp}(\tau) = \tau \rho(0) \int_0^{\infty} K(\lambda) J_0(\lambda \tau) d\lambda \quad , \quad (87)$$

applying Hankel's inversion theorem

$$K(\lambda) = \frac{\lambda}{\rho(0)} \int_0^{\infty} \rho_{sp}(\tau) J_0(\lambda \tau) d\tau \quad . \quad (88)$$

In order to improve the rate of convergence of the integral (88), it was suggested by Koefoed (1965b), an auxiliary function which approaches zero for large spacings of r be used. Since $\rho_{sp}(r) \rightarrow \rho(z_n)$ when $r \rightarrow \infty$, where $\rho(z_n)$ is the lowermost constant resistivity of the medium extending to infinite depth, the following auxiliary function might be used:

$$\psi(\tau) \triangleq \frac{\rho_{sp}(\tau) - \rho(z_n)}{\rho(0)} \quad ,$$

with this change equation (88) can be rewritten as

$$K(\lambda) = \lambda \int_0^{\infty} \psi(\tau) J_0(\lambda\tau) d\tau + \frac{\rho(z_n)}{\rho(0)} \quad (89)$$

For numerical computations, it is convenient to make the change of variable $\lambda r = x$, so that the inversion formula for apparent resistivities of the single-pole type becomes finally

$$K(\lambda) = \int_0^{\infty} \Psi\left(\frac{x}{\lambda}\right) J_0(x) dx + \frac{\rho(z_n)}{\rho(0)} \quad (90)$$

2. Wenner array.-- The expression for the apparent resistivity of the Wenner array $\rho_w(r)$, can not be inverted directly, as seen from the formula

$$\rho_w(\tau) = 2 \rho(0) \tau \int_0^{\infty} K(\lambda) \{J_0(\lambda\tau) - J_0(2\lambda\tau)\} d\lambda \quad (91)$$

A change of variable $\lambda = 0.5\lambda$ in the second Bessel function of the integrand was proposed by Van Nostrand and Cook (1966), so that equation (91) becomes

$$\rho_w(\tau) = \rho(0) \tau \int_0^{\infty} \left\{ 2K(\lambda) - K\left(\frac{\lambda}{2}\right) \right\} J_0(\lambda\tau) d\lambda \quad ,$$

which can be inverted to

$$2K(\lambda) - K\left(\frac{\lambda}{2}\right) = \frac{\lambda}{\rho(0)} \int_0^{\infty} \rho_w(\tau) J_0(\lambda\tau) d\tau .$$

The kernel function $K(\lambda)$ might be obtained from $2K(\lambda) - K(0.5\lambda)$ by a procedure analogous to the reduction of Wenner to single-pole apparent resistivities, which is discussed next.

Koefoed (1966) developed a curve-matching procedure for the inverse transformation of equation (91). Another possibility consists in reducing the Wenner curve to a single-pole curve.

Combining equations (87) and (91), the apparent resistivity of the Wenner array can be expressed in terms of single-pole apparent resistivities:

$$\rho_w(r) = 2\rho_{sp}(r) - \rho_{sp}(2r) \quad (92)$$

Applying (92) successively for $r = \frac{1}{2}r, \frac{1}{4}r, \frac{1}{8}r, \dots, \frac{1}{2^n}r$, and multiplying each side by 1, 2, 4, $\dots, 2^{n-1}$, respectively:

$$\begin{aligned} 1. \quad \rho_w\left(\frac{1}{2}r\right) &= 2\rho_{sp}\left(\frac{1}{2}r\right) - \rho_{sp}(r) \\ 2. \quad 2\rho_w\left(\frac{1}{4}r\right) &= 4\rho_{sp}\left(\frac{1}{4}r\right) - 2\rho_{sp}\left(\frac{1}{2}r\right) \\ 3. \quad 4\rho_w\left(\frac{1}{8}r\right) &= 8\rho_{sp}\left(\frac{1}{8}r\right) - 4\rho_{sp}\left(\frac{1}{4}r\right) \\ &\vdots \\ &\bullet \end{aligned}$$

$$n-1. \quad 2^{n-2} \rho_w \left(\frac{1}{2^{n-1}} \tau \right) = 2^{n-1} \rho_{SP} \left(\frac{1}{2^{n-1}} \tau \right) - 2^{n-2} \rho_{SP} \left(\frac{1}{2^{n-2}} \tau \right)$$

$$n. \quad 2^{n-1} \rho_w \left(\frac{1}{2^n} \tau \right) = 2^n \rho_{SP} \left(\frac{1}{2^n} \tau \right) - 2^{n-1} \rho_{SP} \left(\frac{1}{2^{n-1}} \tau \right),$$

adding equations i to n:

$$\sum_{i=1}^n 2^{i-1} \rho_w \left(\frac{1}{2^i} \tau \right) = 2^n \rho_{SP} \left(\frac{1}{2^n} \tau \right) - \rho_{SP}(\tau),$$

but,

$$\rho_{SP}(r) \rightarrow \rho(0) \quad \text{when } r \rightarrow 0;$$

hence,

$$\rho_{SP}(\tau) \approx 2^n \rho(0) - \sum_{i=1}^n 2^{i-1} \rho_w \left(\frac{\tau}{2^i} \right). \quad (93)$$

Likewise, an expression of the single-pole apparent resistivity in terms of the Wenner curve for increasing spacings of r is obtained by using formula (92) for $r = 2r, 4r, 8r, \dots, 2^n r$, multiplying both sides, respectively, by $\frac{1}{2}, \frac{1}{4}, \frac{1}{8}, \dots, \frac{1}{2^n}$, and adding the equations:

$$\sum_{i=0}^n \left(\frac{1}{2} \right)^i \rho_w(2^i \tau) = 2 \rho_{SP}(\tau) - \frac{1}{2^n} \rho_{SP}(2^{n+1} \tau).$$

In this case $\rho_{sp}(r) \rightarrow \rho(\infty)$ when $r \rightarrow \infty$, which yields the following approximation to the single pole apparent resistivity derived from Wenner data:

$$\rho_{sp}(\tau) \approx \frac{1}{2^{n+1}} \rho(z_n) + \sum_{i=0}^n \left(\frac{1}{2}\right)^{i+1} \rho_w(2^i \tau) . \quad (94)$$

Two criteria can be employed to find the proper number n of terms in series (93), and (94). Let ${}_n\rho_{sp}(r)$ denote the apparent single-pole resistivity computed with n terms of these series; then the computations can be stopped, whenever

$$\left| \frac{{}_{n-1}\rho_{sp}(\tau)}{{}_n\rho_{sp}(\tau)} - 1 \right| < \varepsilon \quad n = 1, 2, \dots ,$$

where ε is a specified error bound depending on the accuracy of the data.

Another way to determine when to truncate the series consists in using the inequalities

$$\left| \frac{\rho(0)}{\rho_w\left(\frac{1}{2^n} \tau\right)} - 1 \right| < \varepsilon$$

and

$$\left| \frac{\rho(z_n)}{\rho_w(2^n \tau)} - 1 \right| < \varepsilon$$

for equations (93) and (94), respectively, with ε as defined before.

The Wenner curve must be specified for all spacings r in order to make the transformation to the single-pole curve. This condition imposes the same requirements on the data as the inversion formula (89), and in particular the need for reasonably accurate values of $\rho(0)$ and $\rho(\infty)$. For transformation of field data, a great amount of interpolation might be necessary.

3. Schlumberger array.-- If ρ_{sl} denotes the Schlumberger apparent resistivity, then

$$\rho_{sl}(\tau) = \rho(0) \left\{ 1 + \tau^2 \int_0^{\infty} \lambda \Phi(\lambda) J_1(\lambda\tau) d\lambda \right\}$$

can be solved for $\Phi(\lambda)$ by the inversion

$$\begin{aligned} \Phi(\lambda) &= \int_0^{\infty} \frac{\rho_{sl}(\tau) - \rho(0)}{\rho(0)\tau} J_1(\lambda\tau) d\tau \\ &= \frac{1}{\rho(0)} \int_0^{\infty} \frac{\rho_{sl}(\tau)}{\tau} J_1(\lambda\tau) d\tau - \int_0^{\infty} \frac{J_1(\lambda\tau)}{\tau} d\tau, \end{aligned}$$

but,

$$\int_0^{\infty} \frac{J_1(\lambda\tau)}{\tau} d\tau = 1,$$

hence,

$$K(\lambda) = \frac{1}{\rho(0)} \int_0^{\infty} \frac{\rho_{sl}(\tau)}{\tau} J_1(\lambda\tau) d\tau \quad (95)$$

As before with the inversion of single-pole apparent resistivities, it is convenient to change the integrand of formula (95) to achieve stronger convergence of the integral.

With

$$\psi(\tau) \triangleq \frac{\rho_{sl}(\tau) - \rho(z_n)}{\rho(0)}$$

the inversion for Schlumberger apparent resistivities becomes

$$K(\lambda) = \int_0^{\infty} \frac{\psi(\tau)}{\tau} J_1(\lambda\tau) d\tau + \frac{\rho(z_n)}{\rho(0)} \quad (96)$$

or, if the change of variable $\lambda\tau = x$ is made,

$$K(\lambda) = \int_0^{\infty} \psi\left(\frac{x}{\lambda}\right) \frac{J_1(x)}{x} dx + \frac{\rho(z_n)}{\rho(0)} \quad (97)$$

In many field cases the lowermost stratum has a very high resistivity compared with the overlaying formations, for instance the igneous or metamorphic basement of a sedimentary basin. Because of the limitations of instrumentation and terrain, the survey generally can not be expanded far enough to define the resistivity of the substratum. For instance, to

record the basement resistivity with an accuracy of 2 percent from the synthetic Schlumberger sounding curve for the Adena field, the survey has to be carried out 4600 km! This is, of course, technically impossible, even if the required current intensity were available, and enough land mass were around, the lateral effects would be overwhelming. Furthermore, the curvature of the earth would not allow applying the horizontal layer model. All one is able to detect is the first part of the branch of the sounding curve, raising with a slope of 1. Because the lowermost constant resistivity $\rho(z_n)$ can not be obtained from surface measurements, equation (96) is not applicable, and another approach is necessary. It is shown in Keller and Frischknecht (1966, p. 116) that in the case of a perfectly resistant substratum

$$\rho_{s1}(r) = r/S, \quad r \rightarrow \infty. \quad (98)$$

In practice, a substratum with a sufficiently strong resistivity contrast displays the rising branch beginning at some finite spacing r_c . In the Hough no.1, (6-2) layer case with a basement resistivity of 600 ohm-m, and a longitudinal resistivity of 4.2 ohm-m, (coefficient of anisotropy = 1.23), for the 3000 m of sedimentary fill, the value of r_c is about five km, (see figure 17).

From (98) and (95) one can write

$$K(\lambda) = \sigma(0) \left\{ \int_0^{r_c} \frac{\rho_{s1}(\tau)}{\tau} J_1(\lambda\tau) d\tau + \frac{1}{S} \int_{r_c}^{\infty} J_1(\lambda\tau) d\tau \right\}$$

$$K(\lambda) = \sigma(0) \left\{ \int_0^{\tau_c} \frac{\rho_{SL}(\tau)}{\tau} J_1(\lambda\tau) d\tau + \frac{J_0(\lambda\tau_c)}{S\lambda} \right\}$$

This last formula can be manipulated into a more convenient form as follows:

$$K(\lambda) = \sigma(0) \left\{ \int_0^{\tau_c} \frac{\rho_{SL}(\tau) - \rho_{SL}(\tau_c)}{\tau} J_1(\lambda\tau) d\tau + \int_0^{\tau_c} \frac{\rho_{SL}(\tau_c)}{\tau} J_1(\lambda\tau) d\tau + \frac{J_0(\lambda\tau_c)}{\lambda S} \right\}$$

$$K(\lambda) = \int_0^{\infty} \psi(\tau) \frac{J_1(\lambda\tau)}{\tau} d\tau + \frac{\rho_{SL}(\tau_c)}{\rho(0)} \int_0^{\tau_c} \frac{J_1(\lambda\tau)}{\tau} d\tau + \frac{J_0(\lambda\tau_c)}{\rho(0)\lambda S} ;$$

where,

$$\psi(\tau) \triangleq \frac{\rho_{SL}(\tau) - \rho_{SL}(\tau_c)}{\rho(0)} ,$$

and,

$$\int_0^{\tau_c} \frac{J_1(\lambda\tau)}{\tau} d\tau = \int_0^{\lambda\tau_c} J_0(x) dx - J_1(\lambda\tau_c) .$$

Hence, the inversion of Schlumberger sounding data in the case of a resistant basement is

$$K(\lambda) = \int_0^{\infty} \psi(\tau) \frac{J_1(\lambda\tau)}{\tau} d\tau + \frac{\rho_{SL}(\tau_c)}{\rho(0)} \left\{ \int_0^{\lambda\tau_c} J_0(x) dx - J_1(\lambda\tau_c) \right\} + \frac{J_0(\lambda\tau_c)}{\rho(0)\lambda S} \quad \lambda \geq \frac{1}{\tau_c} \quad (99)$$

This form has the advantage that Hankel's infinite integral, rather than a definite integral, is required, so that for numerical computations, only three correction terms have to be evaluated in addition to the usual Hankel transform.

4. Polar-dipole array.-- There are two approaches to the inversion of the observed polar-dipole resistivity function $\rho_{pd}(r)$, one leading to a double integral, the other making use of equatorial-dipole or Schlumberger apparent resistivities.

a). The kernel function as a double integral of the polar-dipole resistivity.

By definition

$$\rho_{PD}(\tau) \triangleq \pi \frac{\tau^3}{I} \frac{\partial^2}{\partial \tau^2} U(\tau) \quad ,$$

where,

$$U(\tau) = \frac{\rho(0)I}{2\pi} \left\{ \frac{1}{\tau} + \int_0^{\infty} \Phi(\lambda) J_0(\lambda\tau) d\lambda \right\} \quad ;$$

hence,

$$\rho_{PD}(r) = \frac{1}{2} \rho(0) r^3 \frac{\partial^2}{\partial r^2} \left\{ \frac{1}{r} + \int_0^{\infty} \Phi J_0(\lambda r) d\lambda \right\} ,$$

integrating with respect to r,

$$\begin{aligned} \int_0^r \frac{\rho_{PD}(x)}{x^3} dx + C &= \frac{1}{2} \rho(0) \frac{\partial}{\partial r} \left\{ \frac{1}{r} + \int_0^{\infty} \Phi(\lambda) J_0(\lambda r) d\lambda \right\} \\ &= \frac{1}{2} \rho(0) \left\{ -\frac{1}{r^2} - \int_0^{\infty} \Phi(\lambda) \lambda J_1(\lambda r) d\lambda \right\} ; \end{aligned}$$

with the change of variable $\lambda r = x$, the last equation becomes

$$\int_0^r \frac{\rho_{PD}(x)}{x^3} dx + C = \frac{1}{2} \rho(0) \left\{ -\frac{1}{r^2} - \frac{1}{r^2} \int_0^{\infty} \Phi\left(\frac{x}{r}\right) x J_1(x) dx \right\}. \quad (100)$$

Let $r \rightarrow \infty$, then

$$\int_0^{\infty} \frac{\rho_{PD}(x)}{x^3} dx = -C ,$$

which can be rewritten as

$$C = - \int_0^r \frac{\rho_{PD}(x)}{x^3} dx - \int_r^{\infty} \frac{\rho_{PD}(x)}{x^3} dx .$$

Hence, equation (100) becomes

$$\int_r^{\infty} \frac{\rho_{PD}(x)}{x^3} dx = \frac{1}{2} \rho(0) \left\{ \frac{1}{r^2} + \int_0^{\infty} \Phi(\lambda) \lambda J_1(\lambda r) d\lambda \right\}$$

$$\frac{2}{\rho(0)} \int_{\tau}^{\infty} \frac{\rho_{PD}(x)}{x^3} dx - \frac{1}{\tau^2} = \int_0^{\infty} \Phi(\lambda) \lambda J_1(\lambda \tau) d\lambda ,$$

which can be inverted to

$$\Phi(\lambda) = \frac{2}{\rho(0)} \int_0^{\infty} \int_{\tau}^{\infty} \frac{\rho_{PD}(x)}{x^3} \tau J_1(\lambda \tau) dx d\tau - \int_0^{\infty} \frac{J_1(\lambda \tau)}{\tau} d\tau$$

Finally, the kernel function of the apparent polar-dipole resistivity is given by

$$K(\lambda) = \frac{2}{\rho(0)} \int_0^{\infty} \int_{\tau}^{\infty} \frac{\rho_{PD}(x)}{x^3} \tau J_1(\lambda \tau) dx d\tau . \quad (101)$$

b). Inversion of resistivity sounding data by combining polar and equatorial-dipole curves.

From table XI:

$$\rho_{SL}(\tau) = \rho(0) \left\{ 1 + \tau^2 \int_0^{\infty} \lambda \Phi(\lambda) J_1(\lambda \tau) d\lambda \right\} , \quad (102)$$

$$\rho_{PD}(\tau) = \rho(0) \left\{ 1 + \frac{\tau^2}{2} \int_0^{\infty} \lambda \Phi(\lambda) J_1(\lambda \tau) d\lambda - \frac{\tau^3}{2} \int_0^{\infty} \lambda^2 \Phi(\lambda) J_0(\lambda \tau) d\lambda \right\} , \quad (103)$$

let

$$F(r) \triangleq \rho_{sl}(r) - \rho_{pd}(r) + \rho(0) , \quad (104)$$

then from (102) and (103),

$$F(r) = \frac{r^3}{2} \rho(0) \int_0^\infty \lambda^2 \Phi(\lambda) J_0(\lambda r) d\lambda ,$$

which can be inverted to

$$\Phi(\lambda) = \frac{2}{\lambda \rho(0)} \int_0^\infty \frac{F(r)}{r^2} J_0(\lambda r) d\lambda . \quad (105)$$

This inversion formula can be used only if both ρ_{sl} and ρ_{pd} curves are available (crossed-dipole measurements), and if no lateral effects are present.

A Numerical Technique for the Inversion of Resistivity

Sounding Data

The integral transforms derived so far have to be evaluated by approximate quadrature methods. Slichter (1933) utilized a mechanical integrator; Koefoed (1965a, and 1965b) developed a curve-matching procedure for the transformation. A numerical method, based on the Hankel transform technique described earlier, was used by the author to compute kernel functions from apparent resistivities.

Basically, the procedure used for computing synthetic sounding curves is applicable with minor modifications. The main difference is that apparent resistivities are empirical functions in contrast to the kernel function, which is evaluated analytically. Thus, interpolation between the measured resistivity values is required. Another aspect of field data is the problem of noise; perturbing factors, mainly of geological origin, known generally as lateral effects, are practically always present to some degree. Also, resistivity soundings can seldom be carried out far enough to define the apparent-resistivity curve adequately, especially in the common case of a resistant basement. If in this situation the branch of the Schlumberger curve rising with a slope of 1 can be clearly determined, formula (99) should be used to obtain that part of the kernel function corresponding to $\lambda \geq 1/(\text{maximum spacing})$.

Figure 19 shows the truncation effect of the synthetic Schlumberger curve for the electric log of Hough no.1, model (6-2) in the Hankel transformation. The kernel inverted from this apparent-resistivity curve evaluated for spacings up to 10^8 m agrees within 1 percent with the original kernel curve, and departures can not be shown on a plot of this scale. A truncation of the Schlumberger curve at a spacing $r = 10^6$ m produces a discrepancy of about 20 percent between original

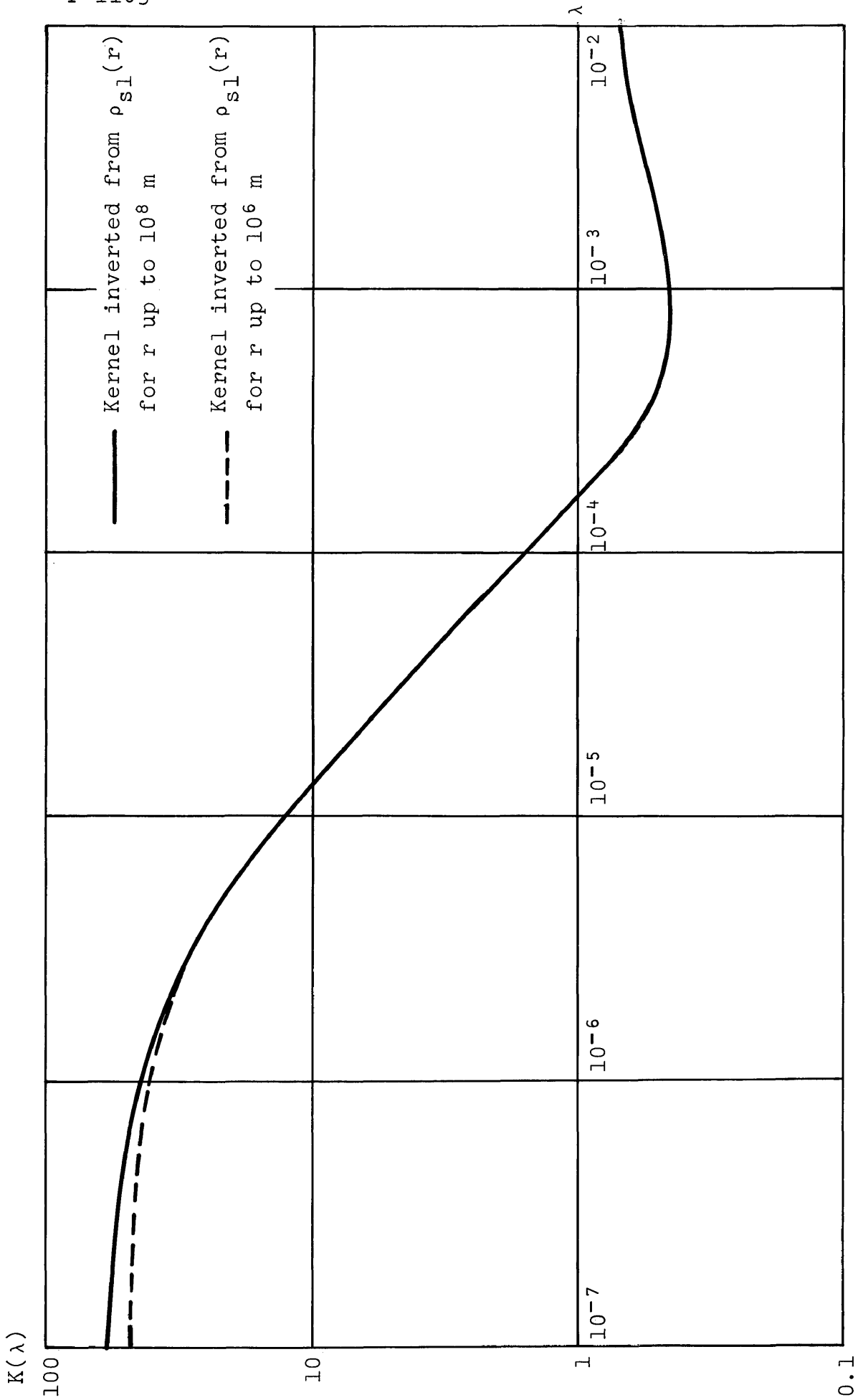


Figure 19.
 Transforms of the synthetic Schlumberger curve for
 Hough no.1, Adena, model (6-2)

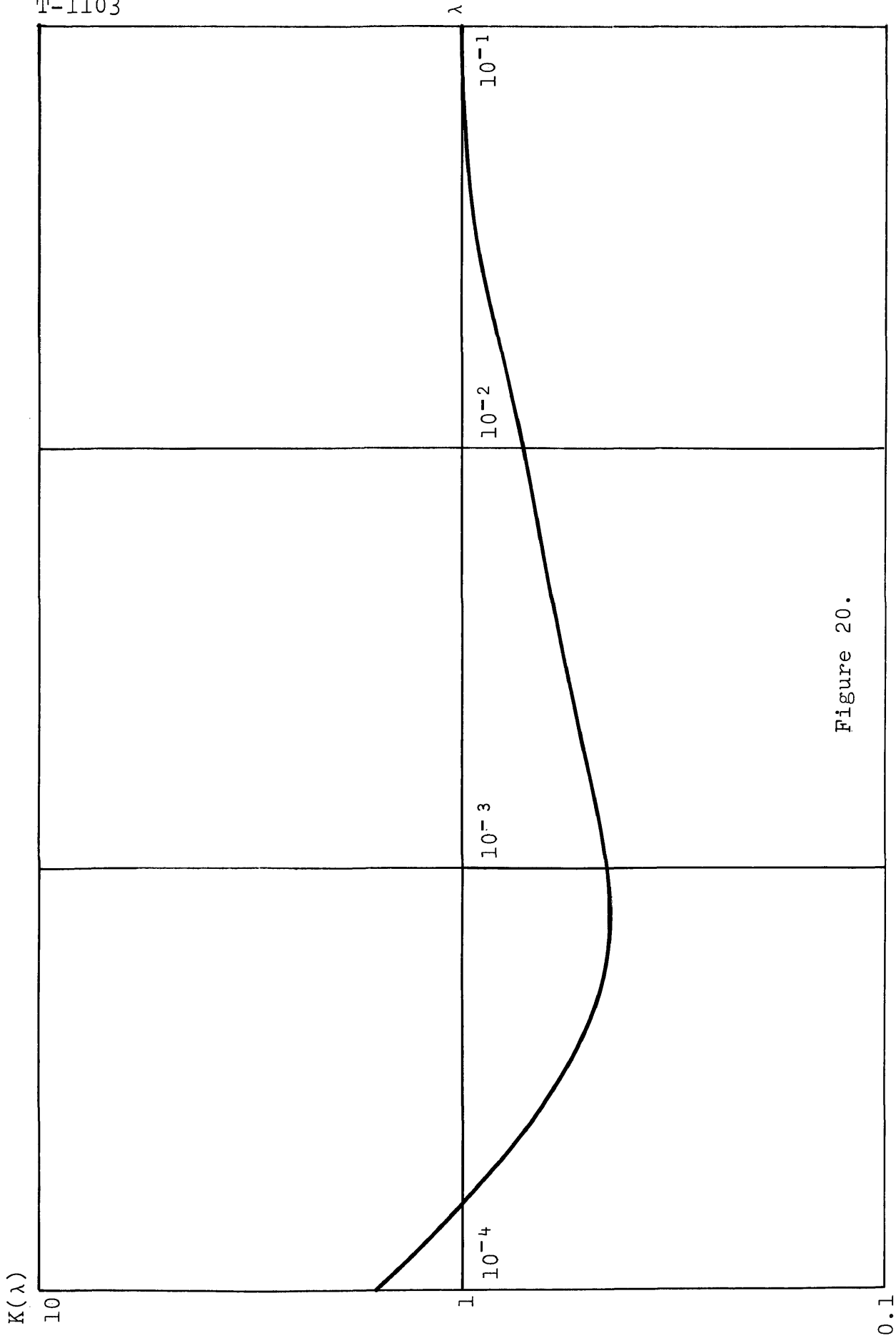


Figure 20.

Transform of the synthetic Schlumberger curve for Hough no.1
using resistant basement formula (99)

and inverted kernels for small values of λ . Figure 20 shows the portion of the kernel function obtained by inverting the Schlumberger sounding data with a maximum spacing of 10 km using formula (99). Once more, the agreement between original and inverted kernel is such that on this graph one curve falls on top of the other.

The transforms of the simulated field data listed in table XV are shown in figure 21. The kernel curve labeled "values picked from smooth curve" was obtained by reading apparent resistivities off the synthetic sounding graph at 20 spacings ranging from 10 m to 5 km. The transform agrees with the original kernel to the degree that discrepancies can not be plotted to the adopted scale. The effect of noise was simulated by the data shown in table XV; its effect is prominent only for larger values of λ (about 0.1) as seen in figure 21. It was further found in these examples that cubic interpolation gave better results than quintic interpolation. For even more "noisy" measurements, smoothing, either by low-pass filters, by drawing smooth curves through the data points, or by fitting polynomials in the least-square sense is probably necessary.

Table XV.
 Simulated Schlumberger field data
 for Adena field

Spacing in m	$\rho_{sl}(r)$ from smooth curve in Ωm	$\rho_{sl}(r)$ with artificial noise in Ωm
10	10.0	9.9
15	10.0	10.1
20	9.9	9.7
25	9.8	9.6
35	9.4	9.5
50	8.8	8.6
70	7.9	7.7
100	6.8	6.9
150	5.9	6.0
200	5.6	5.5
250	5.5	5.4
350	5.3	5.3
500	5.0	4.9
700	4.8	4.7
1000	4.3	4.2
1500	4.0	3.9
2000	4.1	4.1
2500	4.4	4.4
3500	5.6	5.5
5000	7.7	7.7

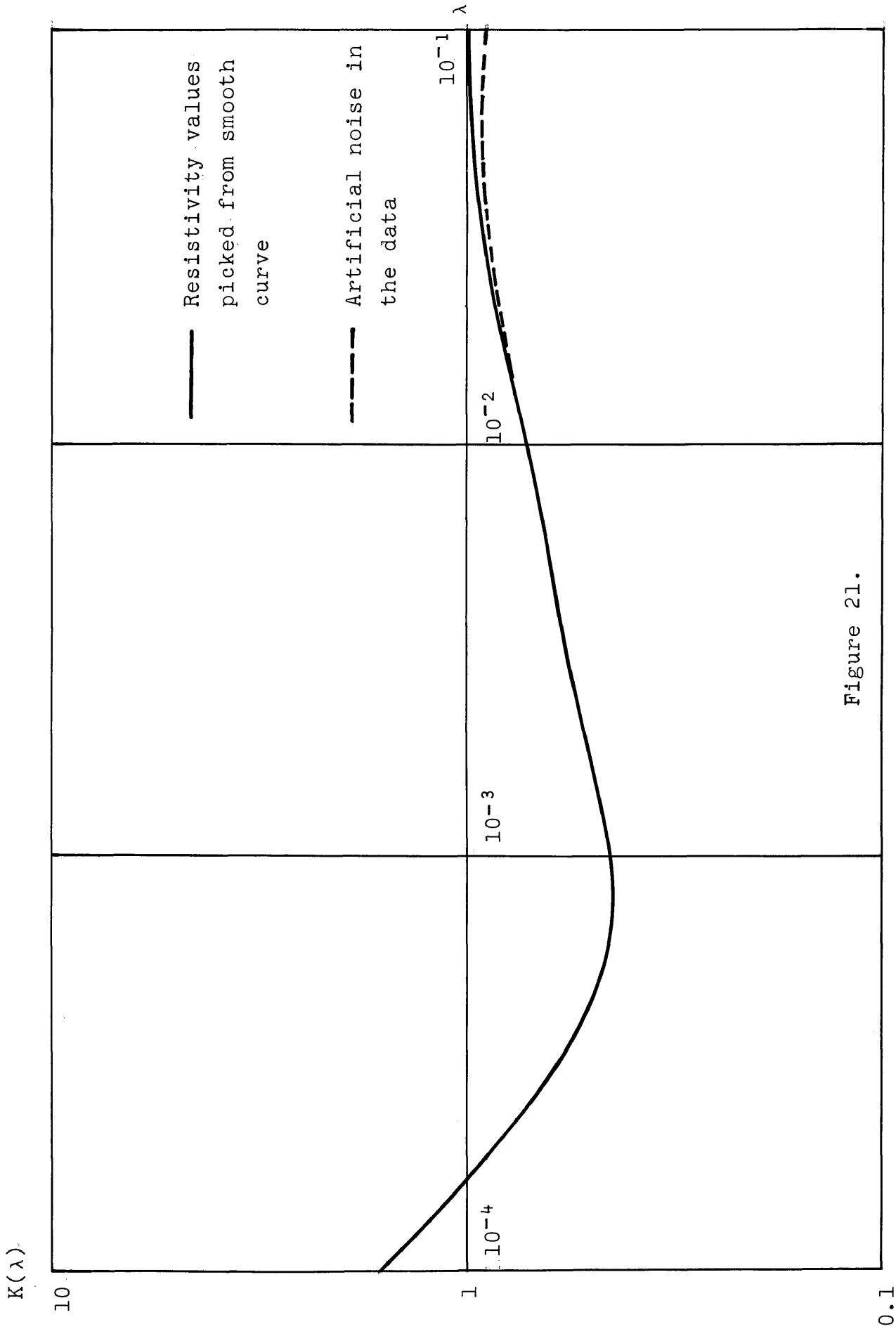


Figure 21.

Transforms of simulated Schlumberger field data for Hough no.1, model (6-2)

The Interpretation of the Kernel Function

The interpretation methods of resistivity sounding data can be roughly divided into direct methods and indirect methods. The direct methods consist of evaluating the resistivity as a function of depth analytically from the kernel function, whereas indirect methods are based on cut-and-try procedures, such as curve matching.

Langer (1933) solved theoretically the problem of determining analytically the continuous resistivity function of depth from the kernel function. However, his method has not been applied because of the algebraic difficulties involved and because the discontinuous resistivity function is much more important in practice. In 1940, Pekeris presented a direct method for interpreting a horizontally layered earth model, if the bed thicknesses increase with depth. His procedure is based on two properties of the layer-kernel function, first the fact that the kernel curve approaches asymptotically a two-layer case for large values of the argument, second, that the effect of the top layer of a section might be removed analytically if its thickness and reflection coefficient with respect to the lower layer are known. A proof of these properties based on Sunde's recurrence relation (25) is very simple and compares favorably with the rather involved original presentation making use of determinants. It is, therefore, worthwhile to give an outline of Pekeris' method.

1. Asymptotic behavior of the kernel function.-- In a section consisting of n layers, let $V_i(\lambda)$ be Sunde's kernel function on top of the i th layer (figure 22).

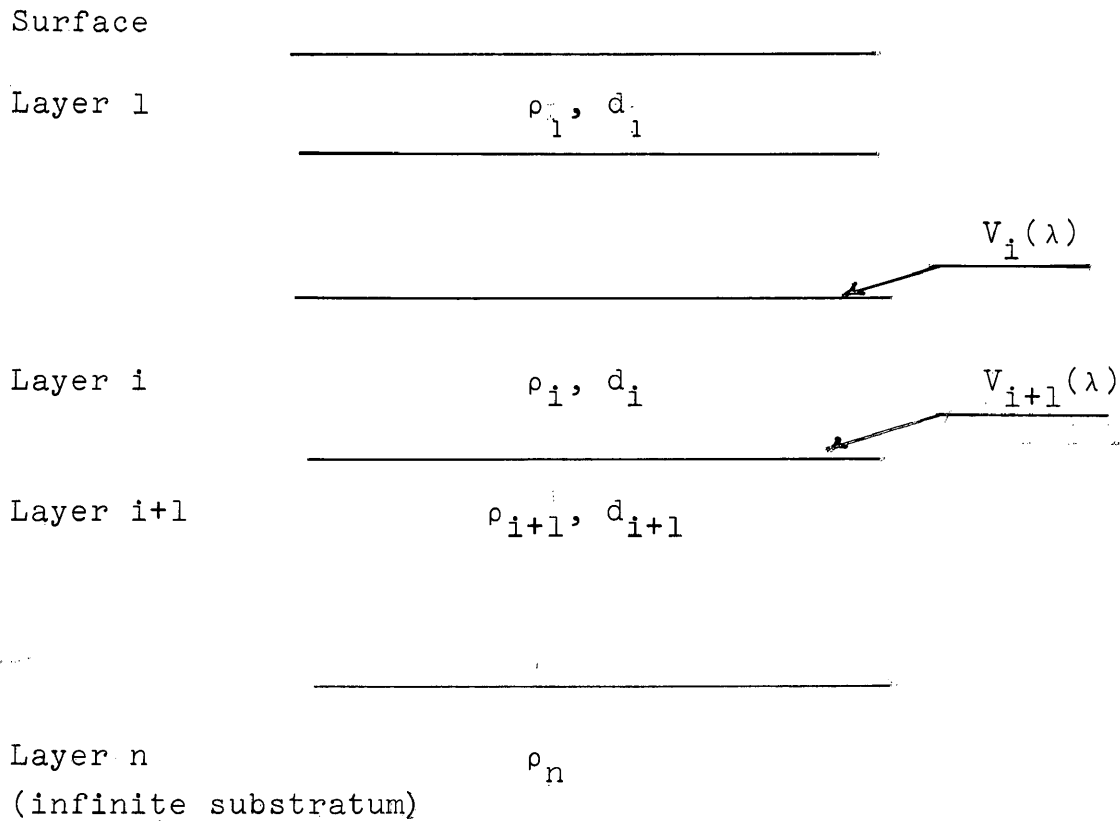


Figure 22.

Horizontally layered earth model

From (25)

$$V_i(\lambda) = \frac{1 - k_i(\lambda)e^{-2\lambda d_i}}{1 + k_i(\lambda)e^{-2\lambda d_i}} = \frac{1 - G_i(\lambda)}{1 + G_i(\lambda)}, \quad (106)$$

where $G_i(\lambda)$ is defined by

$$G_i(\lambda) \triangleq k_i(\lambda)e^{-2\lambda d_i} ; \quad (107)$$

furthermore,

$$k_i(\lambda) = \frac{\rho_i - \rho_{i+1} V_{i+1}(\lambda)}{\rho_i + \rho_{i+1} V_{i+1}(\lambda)} . \quad (108)$$

Taking logarithms of the terms in equation (107)

$$\log\{G_i(\lambda)\} = -2\lambda d_i + \log\{k_i(\lambda)\} , \quad (109)$$

when λ increases $V_{i+1}(\lambda) \rightarrow 1$ by (15), hence, it can be observed from (108) that,

$$\lim_{\lambda \rightarrow \infty} k_i(\lambda) = \frac{\rho_i - \rho_{i+1}}{\rho_i + \rho_{i+1}} \triangleq k_{i,i+1} , \quad (110)$$

$k_{i,i+1}$ denotes the reflection coefficient of the i th bed with respect to the layer beneath it.

Thus, it is seen that equation (109) plotted as semi-logarithmic curve, $\log\{G_i(\lambda)\}$ versus λ , approaches a straight line for large values of λ . The intersection of this line with the $G_i(\lambda)$ axis furnishes the value of the reflection coefficient, its slope the thickness of layer i .

2. Stripping off the top layer.-- Solving (108) for $V_{i+1}(\lambda)$:

$$V_{i+1}(\lambda) = \frac{\rho_i}{\rho_{i+1}} \frac{1 - k_i(\lambda)}{1 + k_i(\lambda)}$$

$$V_{i+1}(\lambda) = \frac{1 + k_{i,i+1}}{1 - k_{i,i+1}} \times \frac{1 - k_i(\lambda)}{1 + k_i(\lambda)}, \quad (111)$$

where $k_i(\lambda)$ is found from (106),

$$k_i(\lambda) = \frac{1 - V_i(\lambda)}{1 + V_i(\lambda)} e^{2\lambda d_i} = G_i(\lambda) e^{2\lambda d_i}. \quad (112)$$

By combining formulas (112) and (111), one can compute the kernel function V_{i+1} in terms of the kernel function V_i on top of the overlaying bed (see figure 22), if the reflection coefficient between the two layers and the bed thickness of the upper layer are known. This process differs from the partial curve-matching procedure in the r -domain, in that the top layer is effectively removed and not replaced by a fictitious layer.

Indirect interpretation is based mainly on graphical methods consisting of comparing the observed kernel function with a set of theoretical master curves to pick out the most likely models. A catalog of kernel master curves is not yet available, at least not to the author's knowledge. However, with a digital computer and a plotter, a considerable number of kernels can be generated efficiently in a short time and compared with the transformed data curve. In this way,

a number of equivalent models fitting the original data with approximately the same error might be obtained, the choice of the most probable layering has then to be based on additional geophysical and geological information.

An indirect numerical technique proposed by Vozoff (1958) consists of fitting the kernel function of an approximate model to the transform of field data in the least-square sense. The layering parameters of the model are adjusted successively by some method, for example steepest descent, until the sum of the squares of the differences between observed and model-kernel function is minimized.

In practice, a semidirect technique, i.e. a combination of direct and indirect methods, will probably give good results. Pekeris' or auxiliary point methods (Zhody, 1965) might be used to get a preliminary, approximate model, which is then adjusted to the transformed sounding curve by modifying the layering parameters.

SUMMARY AND CONCLUSIONS

The kernel function contains all the information on the resistivity variation of a horizontally uniform medium, separated from the effect of source and recording electrodes. This function can, therefore, be used for computation of theoretical sounding curves, or for interpretation of resistivity sounding data.

Apparent resistivities and kernel functions are mutually related by a Hankel transformation. The numerical evaluation of this linear-integral transform by Gaussian quadrature, combined with an Euler transformation, suggested by Longman (1957), yields sufficiently accurate results for exploration. The advantage of this technique over the image method of computing theoretical sounding curves is that more general resistivity variations than horizontal layering might be considered. This point is illustrated by the computation of synthetic sounding curves from representative electrical well

logs for guiding exploration and interpretation of resistivity measurements in the vicinity of the wells. In a specific example it is concluded that "direct" location of oil-saturated zones in the Adena oilfield (Morgan County, Colorado) by surface-based resistivity surveys requires an accuracy of the measurements exceeding 1 percent for spacings of three to five miles.

The quadrature method used in this thesis can be applied to evaluate the kernel function by inverse Hankel transformation of apparent-resistivity curves obtained in electrical surveys. Sufficient numerical accuracy is achieved for the inversion of the synthetic sounding curves for the Adena field, making it possible to use the kernel function for their interpretation.

The kernel-domain approach in interpreting resistivity soundings offers several advantages:

1. Because of the uniqueness of the Hankel transformation, the kernel function can be considered processed data, without addition of information like an apparent-resistivity curve, which is only determined by the accuracy of the measurements.

2. The indetermination in the interpretation arises in the step from the kernel function to the resistivity variation with depth. The interpretation, more an art, than a science, should be limited to this step.

3. Kernel curves can be computed much faster and easier than apparent-resistivity curves. Consequently, any indirect, numerical cut-and-try method works more efficiently in the λ -domain than in the r -domain. Furthermore, necessary additional information on the layering parameters, obtained from adjacent resistivity soundings, from electric logs, from other geophysical surveys, or from geological sources can be built easily into the kernel function.

4. Because the kernel function is independent from the particular measuring array used, only one interpretation scheme is required for all the different types of apparent-resistivity curves.

5. The symmetry property of the kernel domain simplifies interpretation procedures based on curve matching with a catalog of master kernel curves.

6. The kernel-domain approach can be generalized to the interpretation of alternating-current resistivity soundings (Van'yan, 1961).

Before the kernel-domain approach is used in the interpretation of a survey, it has to be decided whether the sounding data are sufficiently accurate, and lateral effects are small enough to guaranty good results in the inverse Hankel transformation.

Future work in the area of kernel-domain interpretation has to consider the problem of the removal of lateral effects and other "noise," either by field techniques or by some processing scheme, in order to prepare the data for inversion.

APPENDIX
LIST AND FLOW CHARTS OF COMPUTER
PROGRAMS USED

The source deck, object code, program constants, and a complete listing of each program is kept on file in the Geophysics Department of the Colorado School of Mines.

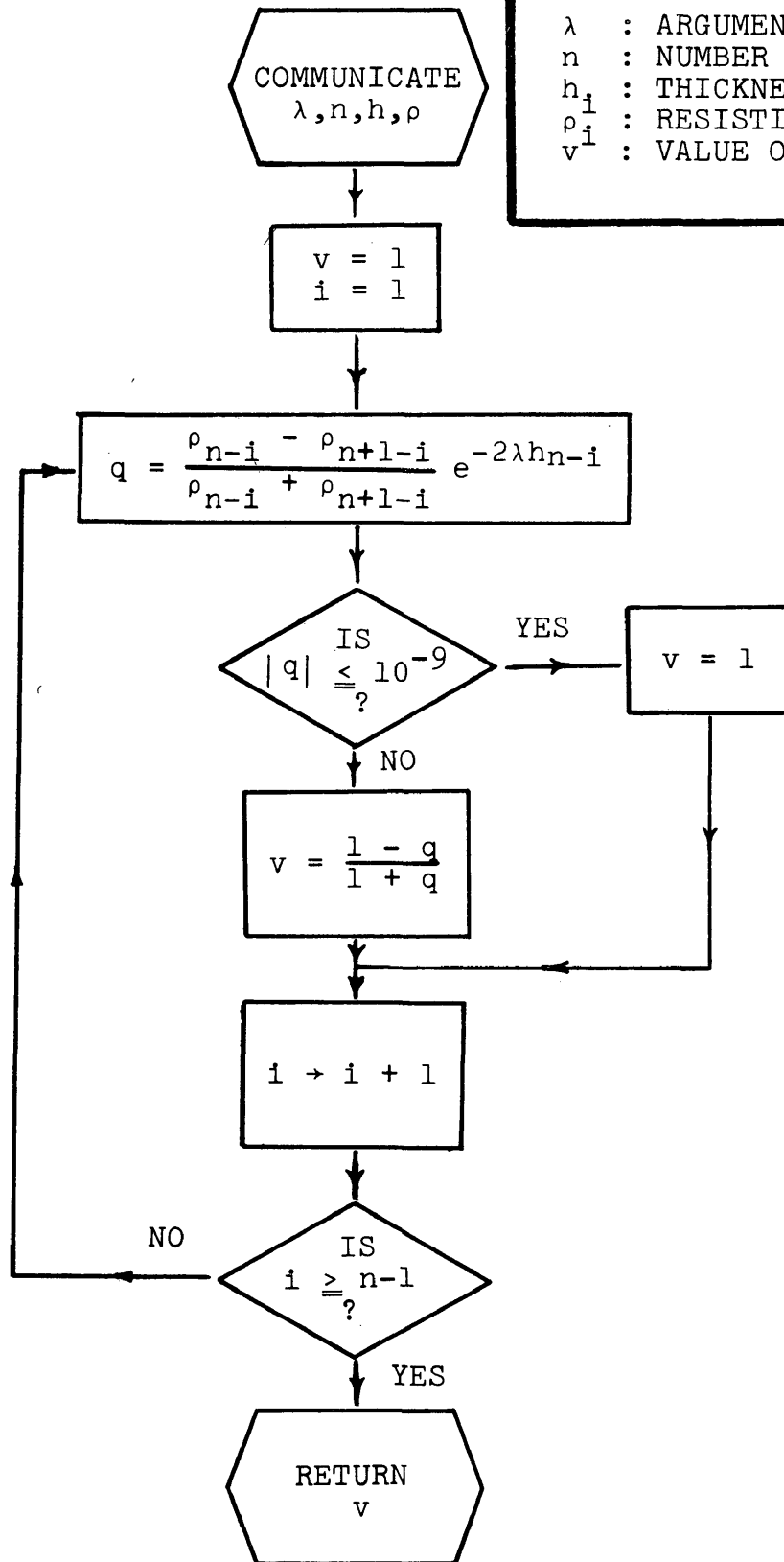
List of Computer Programs

- | No. | Program name and description |
|-----|---|
| 1. | Kernel function for a layered medium, version 1.-- This program computes the kernel function for a layered medium with a specified error at the lower and upper end of the argument. Its main purpose is to get a complete, detailed tabulation of single kernel functions. |
| 2. | Kernel function for a layered medium, version 2.-- This program evaluates the kernel function for a geoelectric section consisting of a surface layer, a sequence of thin layers obtained from a digitized well log, and a lowest layer located between the last resistivity reading on the electric log and the infinite basement. |

3. Kernel function for a layered medium, version 3.-- This program computes the kernel function of a layered medium with specified initial and final values of its argument. Its main purpose is the production of families of kernel functions.
4. Equivalent layers in well-log sections.-- The geoelectric parameters for a specified section of a digitized electric log, and the thickness and resistivity of the equivalent isotropic section are evaluated by this program.
5. Probability density and distribution for resistivities sampled from electric logs.--
6. Synthetic sounding curves package.-- This program computes the integrals in the apparent resistivity formulas for the single-pole, Schlumberger, and/or polar-dipole arrays for a horizontally layered medium. (Fortran IV program).
7. Inversion of the Hankel transform.-- This program evaluates the kernel function from Schlumberger apparent resistivities (Fortran IV program).
8. Subroutine BESFJ0.-- This subprogram computes $J_0(x)$ for real x .
9. Subroutine BESFJ1.-- This subprogram computes $J_1(x)$ for real x .

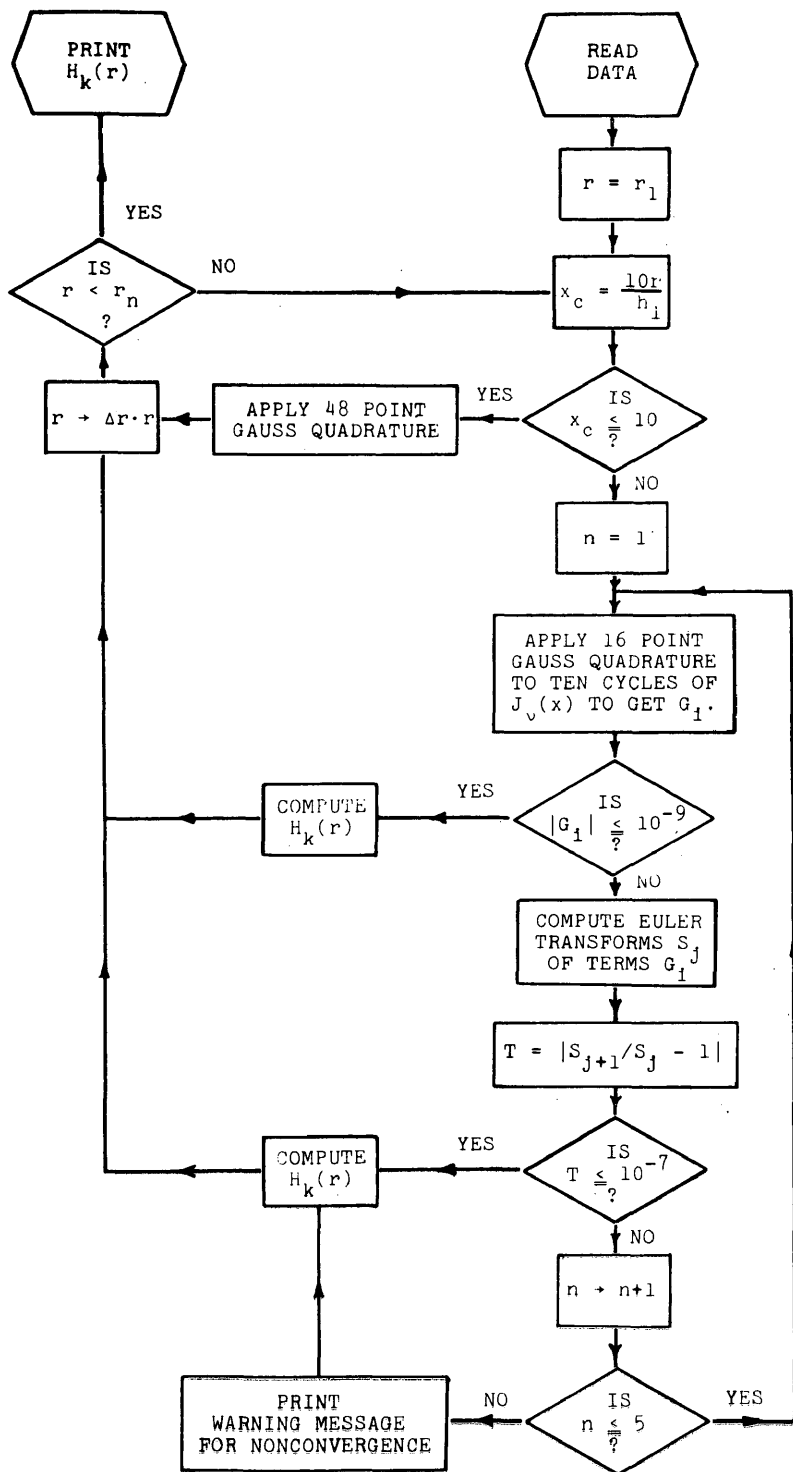
10. Subroutine BESIJ0.-- This program computes $\int_0^x J_0(t)dt$ for real x.
11. Subroutine BIN01.-- This subprogram computes the values of $\int_{t_1}^{t_2} t^n J_0(rt)dt$, and $\int_{t_1}^{t_2} t^n J_1(rt)dt$ by recurrence relations.
12. Evaluation of Bessel functions for large arguments.-- (Fortran IV program in double precision).
13. Subroutine INTPOL.-- This subroutine interpolates between a set of tabulated entries using the method of divided differences.
14. Subroutine APROX1.-- This subroutine evaluates the polynomial passing through a set of unequally spaced points by the method of divided differences.

FLOW CHART FOR SUBROUTINE KERNEL



λ : ARGUMENT OF KERNEL FUNCTION
 n : NUMBER OF LAYERS
 h_i : THICKNESS OF LAYER i
 ρ_i : RESISTIVITY OF LAYER i
 v^i : VALUE OF THE KERNEL FUNCTION.

GENERALIZED FLOW CHART
FOR HANKEL TRANSFORM PROGRAM



SUBPROGRAMS REQUIRED:

Bessel functions J_0 and J_1 ,
Kernel function $A(\lambda)$.

INPUT:

Program constants, abscissas and weights for Gaussian quadrature. Data, thicknesses (h_1), and resistivities (ρ_1) of geoelectric section; initial (r_1), final (r_n), and multiplying increment (Δr) of transform variable r .

INSTRUCTIONAL CONTROL CARDS:

For selection of transform to be computed and for peripheral operations.

AUXILIARY ARRAYS AND VARIABLES:

G_1 : Value of the basic integral evaluated over 1/2 cycle of J_v ($v = 1, 2, \dots, 20$).
 S_j : Euler transforms of G_1 .

OUTPUT:

Hankel transforms $H_k(r)$,

$$H_1(r) = r \int_0^\infty A(\lambda) J_0(\lambda r) d\lambda$$

$$H_2(r) = r^2 \int_0^\infty \lambda A(\lambda) J_1(\lambda r) d\lambda$$

$$H_3(r) = r^3 \int_0^\infty \lambda^2 A(\lambda) J_0(\lambda r) d\lambda$$

REFERENCES

- Abramowitz, M., and Stegun, I. A., (ed.), 1965, Handbook of mathematical functions: New York, Dover. ✓
- Baranov, Vladimir, and Kunetz, Geza, 1958, Distribution du potentiel dans un milieu stratifié: Acad. Sci. Paris, Comptes rendues, v. 247, no. 23, p. 2170-2171.
- Bodvarsson, G., 1966, Direct methods in applied geophysics: Geoexploration, v. 4, no. 3, p. 113-138.
- Bromwich, T. J., 1931, An introduction to the theory of infinite series: London, Macmillan.
- Erdélyi, A., 1954, Tables of integral transforms: New York, McGraw-Hill.
- Flathe, H., 1955, A practical method of calculating geoelectrical model graphs for horizontally stratified media: Geophys. Prosp., v. 3, no. 3, p. 268-294.
- Galbraith, J. N., Simpson, S. M., and Cantwell, T., 1964, Computer applications in geophysical modeling: Colorado School Mines Quart., v. 59, no. 4, part A, p. 67-76.

- Hamming, R. W., 1962, Numerical methods for scientists and engineers: New York, McGraw-Hill.
- Harvard Computation Laboratory, 1947, Tables of the Bessel functions of the first kind of orders zero and one: Cambridge, Mass. University Press.
- Hitchcock, A. J. M., 1957, Polynomial approximation to Bessel functions of order zero and one and related functions: Math. Tables and other Aids to Comp., v. 11, p. 86-88.
- Hummel, J. N., 1929, Der scheinbare spezifische Widerstand: Zeitschr. Geophysik, v. 5, p. 89-103.
- Ince, E. L., 1956, Ordinary differential equations: New York, Dover.
- Jahnke, E., and Emde, F., 1945, Tables of functions: New York, ✓
Dover.
- Keller, G. V., 1964, Compilation of electrical properties from electrical well logs: Colorado School Mines Quart., v. 59, no. 4, part A, p. 91-110.
- 1965, Electrical prospecting, stratigraphic studies, and the search for petroleum: Colorado School Mines Class Notes.
- 1966, Statistical studies of electrical well logs, in Seventh Annual Logging Symposium Trans.: Soc. Prof. Well Log Analysts, part AA.

- Keller, G. V., and Frischknecht, F. C., 1966, Electrical methods in geophysical prospecting: New York, Pergamon Press. ✓
- Koefoed, O., 1965a, A semi-direct method of interpreting resistivity observations: Geophys. Prosp., v. 13, no. 2, p. 256-282.
- 1965b, Direct methods of interpreting resistivity observations: Geophys. Prosp., v. 13, no. 4, p. 568-591.
- 1966, The direct interpretation of resistivity observations made with a Wenner electrode configuration: Geophys. Prosp., v. 14, no. 1, p. 71-79.
- Kunz, K. S., 1957, Numerical analysis: New York, McGraw-Hill.
- Lanczos, C., 1956, Applied analysis: Englewood Cliffs, N.J., Prentice Hall.
- Langer, R. E., 1933, An inverse problem in differential equations: Am. Math. Soc. Bull., v. 39, p. 814-820.
- Longman, I. M., 1957, Tables for the rapid and accurate numerical evaluation of certain infinite integrals involving Bessel functions: Math. Tables and other Aids to Comp., v. 11, p. 166-180. ✓
- Luke, Y. L., 1962, Integrals of Bessel functions: New York, McGraw-Hill.
- Maillet, Raymond, 1947, The fundamental equations of electrical prospecting: Geophysics, v. 12, no. 4, p. 529-556.

Mooney, H. M., and Wetzel, W. W., 1956, The potentials about a point electrode and apparent resistivity curves for a two - three and fourlayer earth: Minneapolis, University of Minnesota Press.

Mooney, H. M., Orellana, E., Picket, H., and Tornheim, L., 1966, A resistivity computation method for layered earth models: Geophysics, v. 31, no. 1, p. 192-203.

Mygdal, K. A., 1963, Adena - largest field in the Denver basin, in Geology of the Northern Denver Basin and Adjacent Uplifts: Rocky Mtn. Assoc. Geologists, p. 222-225.

Onodera, Seibe, 1960, The kernel function in the multiple-layer resistivity problem: Jour. Geophys. Research, v. 65, no. 11, p. 3787-3794.

Parker, J. M. (ed.), 1961, Oil and gas field volume, Colorado Nebraska: Rocky Mtn. Assoc. Geologists.

Pekeris, C. L., 1940, Direct method of interpretation in resistivity prospecting: Geophysics, v. 5, no. 1, p. 31-42.

Pirson, S. J., 1963, Handbook of well log analysis: Englewood Cliffs, N. J., Prentice Hall.

Roman, Irwin, 1963, The kernel function in the surface potential for a horizontally stratified earth: Geophysics, v. 28, no. 2, p. 232-249.

Schlumberger, C., Schlumberger, M., and Leonardon, E. G., 1934, Some observations concerning electrical

- measurements in anisotropic media, and their interpretation: Am. Inst. Mining and Metall. Engineers Trans., v. 110, p. 159-182.
- Slichter, L. B., 1933, The interpretation of the resistivity prospecting method for horizontal structures: Physics, v. 4, p. 307-322.
- Stefanescu, S., Schlumberger, C., and Schlumberger, M., 1930, Sur la distribution électrique potentielle autour d'une prise de terre ponctuelle dans un terrain à couches horizontales homogènes: Le Journal de Physique et le Radium, series 7, v. 1, p. 132-140.
- Sunde, E. D., 1949, Earth conductive effects in transmission systems: New York, Van Nostrand.
- Tranter, C. J., 1951, Integral Transforms in mathematical physics: London, Methuen.
- Van Nostrand, R. G., and Cook, K. L., 1966, Interpretation of resistivity data: U. S. Geol. Survey Prof. Paper 499.
- Van'yan, L. L., Terekhin, Y. I., and Shtimmer, A. I., 1961, Metodika rascheta volnovykh krivkh chastotnogo zondirotvaniya, (Methods of calculation of wave curves of frequency sounding): Prikladnaya Geofizika, no.30, p. 92-102.
- Vozoff, Keeva, 1958, Numerical resistivity analysis: horizontal layers: Geophysics, v. 23, no. 3, p. 536-556.

Watson, G. N., 1952, A treatise on the theory of Bessel functions: Cambridge, University Press.

Zohdy, A. A. R., 1965, The auxiliary point method of electrical sounding interpretation and its relationship to the Dar-Zarouk parameters: Geophysics, v. 30, no. 4, p. 644-660.